Title
Experimental studies of laser guiding and wake excitation in plasma channels

Author
Volfbeyn, Pavel

Publication Date
1998-06-01

LBNL-41892

ERNEST ORLANDO LAWRENCE
BERKELEY NATIONAL LABORATORY

Experimental Studies of Laser Guiding and Wake Excitation in Plasma Channels

Pavel Volfbeyn

Accelerator and Fusion Research Division

June 1998

Ph.D. Thesis

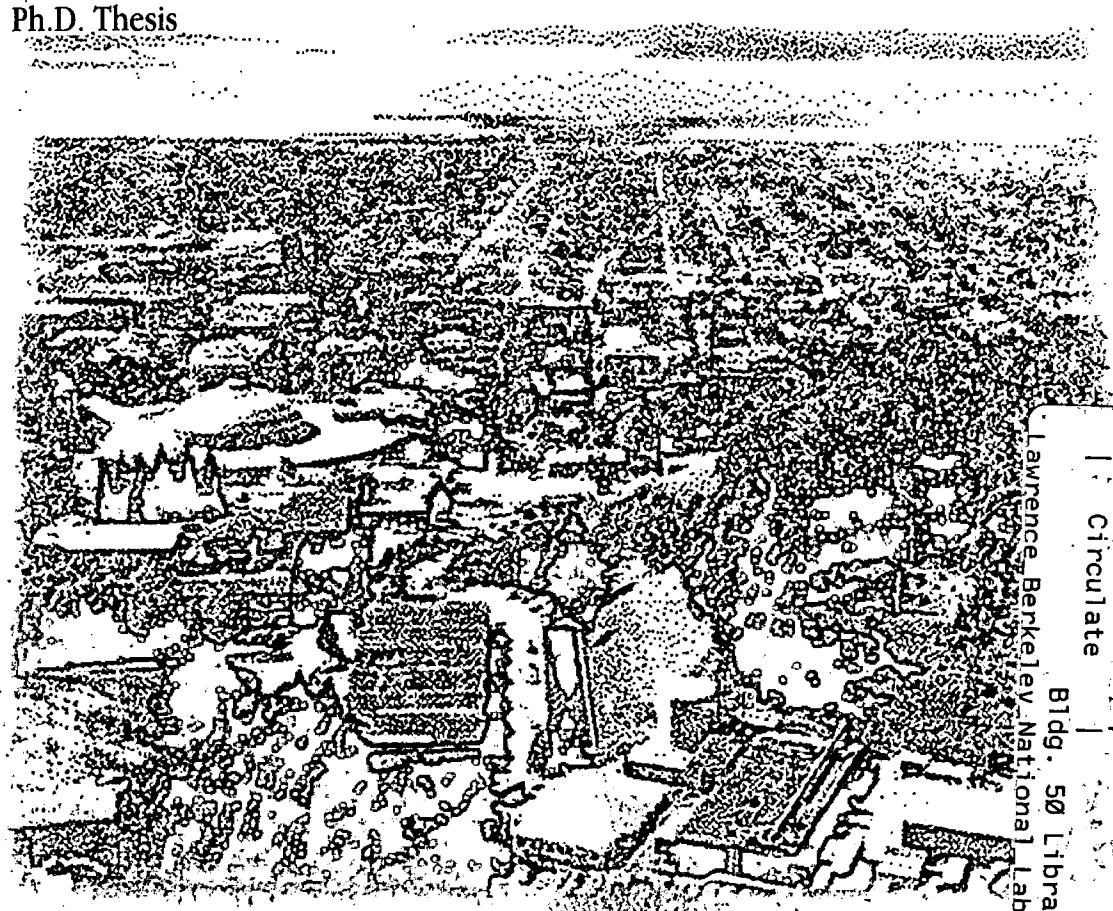

DISCLAIMER

LBNL-41892

Experimental Studies of Laser Guiding and Wake Excitation in Plasma Channels

Pavel Volfbeyn
Ph.D. Thesis

Department of Physics
Massachusetts Institute of Technology

and

Accelerator and Fusion Research Division
Ernest Orlando Lawrence Berkeley National Laboratory
University of California
Berkeley, CA 94720

June 1998

This work was supported by the Director, Office of Energy Research, Office of High Energy and Nuclear Physics, High Energy Physics Division, of the U.S. Department of Energy under Contract No. DE-AC03-76SF00098.

Experimental Studies of Laser Guiding and Wake Excitation in Plasma Channels.

by

Pavel Volfbeyn

M.S., Massachusetts Institute of Technology, 1995

Submitted to the Department of Physics
in partial fulfillment of the requirements for the degree of

Doctor of Philosophy in Physics

at the

MASSACHUSETTS INSTITUTE OF TECHNOLOGY

June 1998

Experimental Studies of Laser Guiding and Wake Excitation in Plasma Channels.

by

Pavel Volfbeyn

Submitted to the Department of Physics
on May 22, 1998 in partial fulfillment of the
requirements for the degree of
Doctor of Philosophy in Physics

Abstract

This thesis presents results of experimental investigations of laser guiding in plasma channels. A new technique for plasma channel creation, the Ignitor – Heater scheme was proposed and experimentally tested in hydrogen and nitrogen. It made use of two laser pulses. The Ignitor, an ultrashort (<100 fs) laser pulse, was brought to a line focus using a cylindrical lens to ionize the gas. The Heater pulse (100-200 ps long) was used subsequently to heat the existing spark via inverse Bremsstrahlung. The hydrodynamic shock expansion created a partially evacuated plasma channel with a density minimum on axis. Such a channel has properties of an optical waveguide. This technique allowed, for the first time, creation of plasma channels in low atomic number gases, such as hydrogen, which is of importance for guiding of highly intense laser pulses. The channel density was diagnosed with time resolved longitudinal interferometry. From these measurements the plasma temperature was inferred.

The guiding properties of the channels were tested by injecting a 5×10^{17} W/cm^2,

75fs laser pulse. The guiding properties and transmission and coupling efficiency were studied as a function of relative position of the channel and the injection pulse focus. Whereas entrance coupling efficiency into the channel was lower than expected, channel coupling to continuum losses were found to be in good agreement with analytical predictions. We speculate that increased coupling efficiency can be achieved through better mode matching into the channel.

Analytic and numerical one dimensional (1-D), nonrelativistic theory of laser pulse propagation in underdense plasma was presented, in the context of laser wakefield acceleration. The relation between the laser pulse energy depletion, longitudinal laser pulse shape distortion, and changes in the group velocity and center wavelength was explored. 1-D theory was extended to treat the case of a laser exciting a wake in a hollow plasma channel, by making use of an energy conservation argument. Based on the results of this theory, a laser wakefield diagnostic was proposed where, by measuring the changes in phase or spectrum of the driving laser pulse, it is possible to infer the amplitude of the plasma wake.

Thesis Supervisors:

W. P. Leemans

Title: Physicist, Group Leader, Lawrence Berkeley National Laboratory

J. S. Wurtele

Title: Associate Professor, University of California Berkeley

Acknowledgements

I am deeply grateful to Wim Leemans. His ideas and labor are behind all that went into this thesis, without him this work would not be possible. The learning experience that I had working with Wim is invaluable, he taught me a great deal of physics and experimental skill. His tact and ability to inspire made my years at LBNL a great experience.

The engineering support of Leon Archambault, Jim Dougherty, and Scott DiMaggio has been essential to this project, I wish to thank them for their hard work.

I would like to thank Jonathan Wurtele for giving me the opportunity to work on this exciting project and for his direction on the theoretical aspects of this thesis.

Gennady Shvets initiated the work on the driving laser pulse evolution. I wish to thank him also for many an enlightening discussion.

I am thankful to Peter Lee, who modified and ran the computer code to calculate the driving laser pulse evolution.

I am grateful to Palma Catravas for her help with the data taking at the final stages of the project, and for the apple fritter that made it possible for Wim and I to go on to observeguiding.

I gratefully acknowledge Kang-Zhu Guo for writing the phase retrieval routine, Roger Falcone for donating equipment to the project, and Earl Marmar for his insightful comments on the thesis.

Discussions with Max Zolotorev, Brad Shadwick, and Carl Schroeder were of great help.

I must acknowledge the generous support and assistance from all the staff at the Center for Beam Physics, LBNL. I am grateful to Swapan Chattopadhyay for giving me the opportunity to work at the Center. Many thanks to Joy Kono, Sam Vanecek, Olivia Wong, and Linda Noel for their help and support.

I would like to express my gratitude to Peggy Berkovitz and Pat Solakoff at the MIT Physics Department, they were extremely helpful and understanding in my special situation as a non-resident student.

My parents have started me on the way to a career in physics. I am grateful for that and for their support throughout my graduate school years.

I am greatly indebted to Beth Chen for her love and support.

Contents

1 Introduction

Testing of new and existing theories in high energy physics requires development of particle accelerators capable of producing particle beams with multi TeV energies [1]. The energy gain in an accelerator is proportional to the product of accelerating field, E_z, and acceleration length, L, $\Delta W = E_z L$. The conventional RF accelerators commonly operate in E_z=10-20 MV/m range and are not expected to reach gradients higher than 200 MV/m, limited by electrical breakdown in the accelerating cavities. The electrical breakdown originates with electron field emission from the walls of the cavity. These electrons generate secondary electrons when they reach other metal parts of the RF accelerating structure and this leads to avalanche breakdown. With the highest conventionally achievable gradients, the length of a multi TeV accelerator, and with it the cost, are likely to be prohibitively high. A solution to this problem is building an accelerator with electric field gradient several orders of magnitude higher than currently achieved with the RF technology, thereby reducing the length of the machine, and thus the cost. Laser Plasma Accelerators have been proposed [2] to eliminate the breakdown problem by operating in plasma with no solid walls in the region of high fields.

The focus of this thesis is on a particular type of plasma accelerator, the Laser Wakefield Accelerator (LWFA). A laser wakefield accelerator uses a single laser pulse travelling through a plasma with the plasma density n less than critical density

$n_c = m/4\pi e^2\omega^2$, where e and m are the charge and mass of the electron respectively and ω is the laser frequency, and leaves behind a longitudinal plasma density modulation at the plasma frequency (a plasma wave) $\omega_p^2 = 4\pi e^2 n / m$. The critical density is a plasma density above which the electromagnetic fields of the laser become evanescent in the plasma. To excite a large amplitude plasma wave, the laser pulse must have extremely intense fields, such that the quiver velocities of the plasma electrons are relativistic and should have a duration on the order of the plasma period. This plasma wave has phase velocity equal to the laser group velocity. In an underdense plasma this velocity is close to the speed of light. Thus, this plasma wave is well suited to accelerating relativistic electrons, because a highly relativistic electron, moving with velocities close to the speed of light, will sample the accelerating phase of the plasma wave for extended periods of time. Because the accelerating process happens on the timescale of several plasma periods, the plasma stays organized and confined and most of the well known plasma instabilities are avoided.

Since the original proposal of laser driven plasma accelerators [2] in 1979, where it was proposed that plasma waves with extremely high longitudinal electric fields and with phase velocity close to the speed of light can be excited by ponderomotive pressure of a laser pulse [3], the field has progressed past the proof-of-principle stage (for a recent review see E. Esarey et al. [12]).

The ability of laser pulses to excite plasma waves with high gradients (>1 GV/m) was first shown in plasma beat wave experiments [4], where the plasma waves were

excited by a train of pulses produced by beating of two long laser pulses instead of a single laser pulse. The reason for using the beat wave scheme for the plasma wave excitation was because laser technology capable of producing high intensity ultrashort pulses was not available in the early 1980's. A pulse train with pulse spacing equal to the plasma period was produced by beating two appropriately chosen lines of a CO_2 laser. By accelerating externally injected electrons [5], these beat wave experiments proved that the excited plasma waves had large gradients (30 GV/m) with a phase velocity close to the speed of light.

Chirped pulse amplification [6] in lasers made it possible to produce the higher laser intensity and shorter pulse duration of a single pulse, needed for experimental studies of LWFA, where a single laser pulse with duration matched to the plasma period is used to excite the plasma wave [2].

The next step in the development of the LWFA, after the demonstration of the ability to excite plasma waves with high electric field gradients, is making an accelerating structure with a macroscopic acceleration length. There are several effects limiting the acceleration length and hence, the maximum energy achievable in a LWFA structure. The first and most severe limit on the energy gain in a homogeneous plasma LWFA is laser diffraction. To reach the high intensities needed for plasma wave excitations, on the order of 10^{18} W/cm^2, the laser pulse (or pulses) must be focused to spotsizes on the order of several laser wavelengths. In all experiments to date, the high plasma electric fields were confined to distances on the order of the diffraction distance of the laser, the Rayleigh range. In order for laser acceleration to achieve higher energies, desirable for future

colliders, the acceleration distance must be increased. Consequently, the laser beam must remain tightly focused over distances of many Rayleigh ranges. The second limitation stems from the fact that the plasma wave phase velocity (equal to the group velocity of the exciting laser pulse) is less than the speed of light. In this so called dephasing limit, an electron will initially gain energy from the wave and subsequently slip into a decelerating region of the plasma oscillation by overtaking the wave. The third limitation arises from the depletion of the laser pulse, as it gives up energy to the plasma wave. This again yields an upper limit on how long a LWFA structure can be. Whereas the laser depletion is unavoidable and is, in fact, an inherent consequence of plasma wave excitation, the diffraction must and can be overcome. These three limits on the acceleration length are addressed in this thesis.

Laser guiding in plasma channels has been proposed [7] as a means to extend the acceleration length. The index of refraction in a plasma of density n can be approximated by $\eta_R \approx 1 - \frac{\omega_p^2}{2\omega^2}$. As in an optical fiber, a plasma channel can provide optical guiding if the index of refraction peaks on axis. This requires a plasma density profile that has a local minimum on axis. To be relevant for high gradient LWFA, a plasma channel has to be able to guide a high intensity, ~10^{18} W/cm^2, laser pulses over distances approaching the dephasing length (several centimeters for plasma densities around 10^{18} cm^{-3} and a laser wavelength of about 1 micron).

Experimentally, low power laser pulses have been guided in plasma channels [8]. In these experiments one laser pulse (~100 ps, ~100 mJ) was brought to a line focus in a

mixture of high atomic number (Z) gases with an axicon lens to produce a few cm long plasma, and subsequently heat it via inverse Bremsstrahlung. The resulting hydrodynamic expansion led to a time-dependent density profile with a minimum on-axis. Pulse propagation over distances of up to 70 Rayleigh lengths (about 2.2 cm) of moderately intense laser pulses ($< 5x10^{14}$ W/cm^2), with pulse lengths much larger than the plasma period, was demonstrated in these experiments. The intensity of the channel creation laser pulse, achieved in these experiments was not sufficient for ionization of low Z gases, but required instead the use of high Z gases. Unfortunately, in channels produced with high Z gases, an ultra-intense pulse would further ionize the gas on the channel axis, thereby negating the guiding. While the 100 ps long laser pulse was energetic enough to cause significant plasma heating, ionization of low Z atoms requires an order of magnitude higher laser intensity.

To allow the use of low Z atoms and to demonstrate the feasibility of guiding of the highly intense laser pulses over many Rayleigh ranges we have developed a novel method for channel production: the Ignitor - Heater technique. With this technique gases can be fully stripped of electrons, or ionized to sufficient depths, so that the intense laser pulse, which is injected into the channel to drive the plasma wave, does not alter the channel plasma density profile through additional ionization. Rather than utilizing a single laser pulse for ionization and heating, this scheme makes use of two laser pulses. A femtosecond "Ignitor" pulse is used to create the initial spark. A longer, ~200 ps, perfectly time synchronized "Heater" pulse is then introduced to heat the plasma. Results of Ignitor – Heater channel production experiments and measurements of the

channel transverse plasma density profile with femtosecond Mach-Zehnder interferometry will be presented. The guiding of intense laser pulses will be experimentally verified and issues related to energy coupling in these channels will be studied.

We then investigate the other two limits on the LWFA interaction length, laser pulse depletion and dephasing. At laser intensities on the order of 10^{18} W/cm^2 the index of refraction of the plasma is modified by its interaction with the laser pulse through relativistic effects as well as through a plasma density modulation arising from the excited plasma wave. The interaction with plasma affects both longitudinal and transverse properties of the laser pulse, which, in turn, leads to changes in the coupling between the laser pulse and the plasma as well as in properties of the accelerating plasma wave. These issues affect the depletion and dephasing. They are important for evaluation and optimization of the efficiency of LWFA designs. We present a one dimensional (1-D), nonrelativistic analytic model of the driving pulse evolution and supporting simulation results. A novel theoretical approach, based on energy conservation, is used to extend the 1-D theory to treat laser pulse evolution as it excites a plasma wake in a channel. The relation between the laser pulse energy depletion, longitudinal laser pulse shape distortion, and changes in the group velocity and center wavelength is explored. Based on the results of this theory we propose a new plasma wave diagnostic method based on the theory of the evolution of the driving laser pulse [9].

The first measurements of the excited plasma wave amplitude were done by Thomson scattering [10]. Energy spectra of externally injected electrons, accelerated in

the plasma, were later used as a measure of the plasma wave fields [5], which agreed with the Thomson scattering measurements. Longitudinal femtosecond interferometry [11], using an externally injected laser pulse and measuring the phase shift imparted to it by the plasma wave as a function of delay time after the driving pulse, was shown recently to be yet another valuable technique for measuring the excited wave amplitude.

The diagnostic proposed in this thesis derives information about the first period (from the front of the laser pulse) of the excited plasma wave, through measurement of the phase or frequency evolution of the driving laser pulse. It is passive, in that it does not require any additional laser pulses or an externally injected electron beam.

In Chapter 2 of this thesis we begin with the theory of the LWFA in a homogeneous plasma and in a plasma channel. Discussion of the physics governing the ionization and inverse Bremsstrahlung heating, in the laser acceleration relevant regime, is given in Chapter 3. The description of the Ti:Sapphire laser system we have built specifically for the experiments of this thesis is given in Chapter 4. The major experimental results are presented in Chapter 5. These are a proof-of-principle experiment on the Ignitor - Heater scheme, the first measurements of plasma channel profiles in hydrogen, obtained with longitudinal two dimensional imaging interferometry with femtosecond temporal resolution, demonstration of intense laser pulse guiding, and coupling efficiency characterization. A theoretical treatment of the driving laser pulse evolution as it excites a plasma wave in a homogeneous plasma and in a plasma channel is given in Chapter 6, followed by conclusions in Chapter 7.

2 Theory of Laser Wakefield Generation and Plasma Channel Guiding

This Chapter covers the basic theory required for understanding the Laser Wakefield Accelerator (LWFA) [2], [3], and [12] and laser guiding in a plasma channel. In a LWFA, an ultra-short laser pulse is used to excite a plasma wave via the ponderomotive force from the gradient in the laser pulse intensity. The laser pulse length τ is chosen such that $\omega_p \tau \approx \pi$.

Analytical calculation of the coupling of a laser pulse to a longitudinal plasma wave in a homogeneous plasma is presented in Section 2.1. Section 2.2 addresses guiding of laser pulses in plasma channels. The plasma wakefield modes in channels are discussed in Section 2.3.

2.1 Basic Theory

In this section, the well known cold fluid model for laser plasma interactions is derived. The driving laser pulse couples to the plasma through Maxwell's Equations:

$$\nabla \times \vec{E} = -\frac{1}{c}\frac{\partial \vec{B}}{\partial t};$$
$$\nabla \times \vec{B} = \frac{1}{c}\frac{\partial \vec{E}}{\partial t} + \frac{4\pi}{c}\vec{J}, \tag{2.1}$$

where $\vec{E}$ and $\vec{B}$ are the laser electric and magnetic fields respectively, and $\vec{J}$ is the current density in the ambient plasma due to the laser pulse. Eq. (2.1) is rewritten in terms of the Lorentz invariant normalized vector potential $\vec{a}_0 = \frac{e\vec{E}}{\omega mc}$, where c is the speed of light in vacuum, by taking the curl of the first equation, a time derivative of the second, and combining them, to obtain the wave equation

$$\nabla \times \nabla \times \vec{a}_0 + \frac{1}{c^2}\frac{\partial^2 \vec{a}_0}{\partial t^2} = \frac{4\pi e}{mc^3}\vec{J}. \tag{2.2}$$

From now on a linearly polarized laser pulse with purely transverse fields is assumed and any fast oscillations at twice the laser frequency are averaged. The assumption is valid, provided the laser spotsize is much larger than the wavelength. Eq. (2.2) becomes a scalar equation with the amplitude a_0 of the normalized vector potential replacing the vector, where $\hat{e}_x a_0 = \vec{a}_0$. Since the transverse size of the laser pulse is much larger than the amplitude of the displacement of an electron ($\sim a_0 c/\omega$), the transverse canonical momentum of an electron moving in the laser fields is conserved and $\gamma V_\perp / c = -a_0$, where $V\perp$is the amplitude of the electron quiver velocity, the electron quiver velocity is collinear with $\vec{a}_0$, and $\gamma = \left(1 + a_0^2/2\right)^{1/2}$. The transverse current density then is also collinear with $\vec{a}_0$, its amplitude is J=-nea$_0$c and

$$\frac{4\pi e}{mc^3} J = -\frac{\omega_p^2}{c^2} a_0.$$

(2.3)

Under the assumption that the vector potential is purely transverse, Eq. (2.3) becomes:

$$\nabla \times \nabla \times a_0 + \frac{1}{c^2}\frac{\partial^2 a_0}{\partial t^2} = -k_p^2 a_0,$$

(2.4)

where $k_p = \frac{\omega_p}{c}$.

In a slab geometry we obtain

$$-\frac{\partial^2 a_0}{\partial z^2} - \frac{\partial^2 a_0}{\partial x^2} + \frac{1}{c^2}\frac{\partial^2 a_0}{\partial t^2} = -k_p^2 a_0.$$

(2.5)

In a 1-D model a transversely homogeneous plasma and a plane laser wave are assumed. In that case the x-derivative is zero and the vector potential a_0 is a function of z and t only. Changing variables to $z = z$, $\xi = z - ct$ transforms Eq. (2.5) into

$$\frac{\partial^2 a_0}{\partial z^2} + 2\frac{\partial^2 a_0}{\partial z \partial \xi} = k_p^2 a_0.$$

(2.6)

The next section is concerned with determining the right hand side of Eq. (2.6)

2.1.1 Laser Wakefield in Uniform Plasmas

The right hand side of Eq. (2.6) describes the influence of the plasma on the pulse propagation. The laser pulse, through the ponderomotive force, excites a wake. The physics of ponderomotive excitation of plasma wakes is the focus of this section.

The widely used cold electron fluid model is based on some simplifying approximations. The laser duration is on the order of $1/\omega_p$, so the ion motion is neglected. The plasma is assumed to be underdense, or $\omega_p << \omega$. The plasma electrons experience action of the laser fields, denoted by E and B or, in dimensionless form, by the Lorentz invariant normalized vector potential a_0. The assumption of purely transverse laser fields is justified if the laser spotsize is much larger than the wavelength, or if the laser is assumed to be near to a waist. The excited wave amplitude is found from the fluid equation for the electrons

$$\frac{\partial \vec{v}}{\partial t} + (\vec{v} \cdot \nabla)\vec{v} = \frac{e}{m}\left(\vec{E}_\perp + \frac{\vec{v}}{c} \times \vec{B}_\perp + \vec{E}_p \right), \tag{2.7}$$

where $\vec{v}$ is the velocity of a fluid element and $\vec{E}_p$ is the electric field generated by the plasma wave. The thermal pressure, ∇nkT, is neglected since the thermal velocity is, by assumption, much smaller than the velocity of the oscillatory motion in the laser field, $v_{th} << v_{osc}$. The electron velocity is written as

$$\vec{v} = \vec{a}c + \vec{v}_s. \tag{2.8}$$

Eq. (2.8) is motivated by the fact that, provided that the maximum electron excursion is

much less than the laser spotsize, r_s, (the $a_0 c/\omega r_s << 1$ limit), in the absense of the plasma wave, $\vec{v} = \vec{a}c$ would satisfy Eq. (2.7) because the transverse derivative part of the second term of the left hand side of the Eq. (2.7) would be much smaller than the longitudinal derivative part. The s subscipt denotes a slow velocity term, varying as $\omega_p << \omega$. $\vec{v} = \vec{a}c$ can be obtained from the conservation of transverse momentum as well. By substituting Eq. (2.8) into Eq. (2.7) and averaging over the fast laser period, an equation describing the evolution of the slow component of electron velocity, $\vec{v}_s$, is obtained

$$\frac{\partial \vec{v}_s}{\partial t} = \frac{e}{m}\left(\vec{E}_p + \nabla f\right), \tag{2.9}$$

where f is the laser ponderomotive potential given by

$$f = \frac{mc^2}{4e} a_0{}^2. \tag{2.10}$$

Solving the continuity equation for the perturbation to initial plasma density $n = n_0 + \delta n$:

$$\frac{\partial}{\partial t}\frac{\delta n}{n_0} = -\nabla \cdot \vec{v}_s. \tag{2.11}$$

From the Poisson equation

$$\nabla \cdot \vec{E}_p = 4\pi e \delta n \tag{2.12}$$

and Eqs. (2.9) and (2.11), an equation for plasma wave excitation is obtained

$$\left(\frac{\partial^2}{\partial t^2}+\omega_{p0}^2\right)\frac{\delta n}{n_0}=\frac{e}{m}\nabla^2 f, \tag{2.13}$$

where $\omega_{p0}^2 = 4\pi e^2 n_0 / m$ is the unperturbed plasma frequency.

After making a variable change $\xi = z - ct$, $t = t$, as is common, we have

$$\left(\frac{\partial^2}{\partial \xi^2}+k_p^2\right)\frac{\delta n}{n_0}=\left(\nabla_\perp^2+\frac{\partial^2}{\partial \xi^2}\right)\frac{{a_0}^2}{4}, \tag{2.14}$$

where $k_p=\omega_p/c$, and, again under assumptions of $|\vec{a}| << 1$ and $\frac{\omega_p}{\omega} << 1$.

The solution to the driven harmonic oscillator equation (Eqn.(2.14)) can be written as

$$\frac{\delta n}{n}=\frac{a_L^2(\zeta,r)}{2}+k_p\int_\zeta^\infty \sin(k_p(\zeta-\zeta'))\frac{a_L^2(\zeta',r)}{2}d\zeta' - \frac{1}{k_p}\int_\zeta^\infty \sin(k_p(\zeta-\zeta'))\left[\frac{1}{r}\frac{\partial}{\partial r}r\frac{\partial}{\partial r}\frac{a_L^2(\zeta',r)}{2}\right]d\zeta' \tag{2.15}$$

2.2 Plasma Channel as Optical Guide

As discussed in Chapter 1, for the LWFA to achieve the high energies needed by the high energy physics community, the wake excitation must be done by a guided laser pulse in a plasma channel. Similar to conventional fiber optics, the transverse

characteristics of the laser beam are determined by the transverse profile of the guide, i.e. the plasma density profile. There are two main types of channels that have been considered in the literature: the parabolic channel and the hollow channel. The parabolic channel has a cylindrically symmetric, parabolic density profile with minimum density on axis. It is usually assumed that the plasma wake in a parabolic channel is purely electrostatic or, equivalently, that the channel size is large compared to the plasma wavelength [13], [14]. The hollow channel refers to a cylindrically symmetric step plasma density profile, where the density inside the channel is zero, and the wall thickness is much less than a plasma wavelength.

A hollow channel is particularly favorable for the propagation of a high quality electron beam. It supports a single electromagnetic plasma wave mode and can be designed to support only one guided laser mode [13], [15]. This suppresses the laser hose instability [13], [14]. Full control over the channel profile remains a major experimental challenge and density profiles are typically neither parabolic nor hollow. The transverse fields of the plasma wave excited in an arbitrary profile channel have not been found analytically [13], [15], although much progress has been made in numerically determining the electromagnetic plasma wake modes [16].

The optical guiding of laser pulses in plasmas over extended distances (many Rayleigh lengths) can occur through a combination of effects: relativistic self-focusing, [17], [18], [19], [20], [21], [22], [23], and [24], preformed density channels [7], [25], and [26], and plasma wave guiding [23]. These optical guiding mechanisms are based on the principle of refractive guiding. Refractive guiding can occur when the radial profile of

the index of refraction, $\eta_R(r)$, exhibits a maximum on axis, i.e., $\partial\eta_R / \partial r < 0$. The index of refraction for a small amplitude electromagnetic wave propagating in a uniform plasma with density $n = n_o$ in the 1D limit is given by $\eta_R = ck/\omega = (1-\omega_p^2/\omega^2)^{1/2}$. For large amplitude waves, however, variations in the electron density and mass will occur, i.e., [26]

$$\eta_R(r) \cong 1 - \frac{\omega_p^2}{2\omega^2}\frac{n(r)}{n_o\gamma(r)} \tag{2.16}$$

assuming $\omega_p^2/\omega^2 << 1$. The leading order motion of the electrons in the laser field is the quiver motion $p_\perp = mca$ and, hence, $\gamma \cong \gamma_\perp = \sqrt{1+a_0^2/2}$ and the radial variation of $a_0(r)$ can lead to relativistic selffocusing. The density profile contributes if there is a preformed density channel, e.g. $n(r) = n_0 + \Delta n$, where $\Delta n_p = \Delta n r^2/r_0^2$ and r_o determines the curvature of the channel plasma density profile. In the limits $a_0 << 1$ and $|\Delta n_p / n_o| << 1$ the refractive index is given by

$$\eta(r) \cong 1 - \frac{\omega_p^2}{2\omega^2}\left(1 - \frac{a^2}{2} + \frac{\Delta n_p}{\Delta n_0} + \frac{\delta n_w}{n_0}\right), \tag{2.17}$$

where a wake response is included in $\delta n_w / n_0$.

For the short pulses (of order a plasma wavelength), however, relativistic guiding is substantially reduced [23]. This is due to the tendency of the ponderomotive force from the front of the pulse to push plasma electrons forward and generate a density

increase, δn_w, which balances the relativistic mass increase. The plasma frequency then has no transverse variation and cannot optically guide the laser pulse.

An equation describing the evolution of the laser spot size, r_S, can be derived by analyzing the paraxial wave equation with an index of refraction given by Eqn.(2.17)Assuming the radial profile of the laser pulse is approximately Gaussian, $a_0^2 \propto e^{-2r^2/r_s^2}$ and ignoring the wake, the normalized laser spot size $R = r_s/r_0$ (r_O is the initial laser spot size) evolves according to [13], [22], [26]

$$\frac{d^2R}{dz^2} = \frac{1}{Z_R^2 R^3}\left[1 - \frac{P}{P_c} - \frac{\Delta n}{\Delta n_c} R^4\right] \tag{2.18}$$

where $P \propto a^2 r_s^2$ is the laser power and is constant (independent of z) in the paraxial approximation, $Z_R = k r_0^2/2$ is the Rayleigh length, $P_c[GW] \cong 17(\omega/\omega_p)^2$ is the critical power for self-focusing, [13], [17]-[22], and $\Delta n_c = (\pi r_e r_0^2)^{-1}$ is the critical depth and $r_e = e^2/m_e c^2$ is the classical electron radius.

The terms on the right side of Eqn.(2.18) represent vacuum diffraction, relativistic self-focusing, and channel guiding, respectively. Note if $P = \Delta n = 0$, $r_s = r_0\left(1 + z^2/Z_R^2\right)^{1/2}$, which is the vacuum diffraction result. In the absence of a plasma wake the general condition (see, for example, [17]), to guide (i.e., r_S = constant) a long, axially uniform pulse in a plasma is $P/P_c \geq 1 - \Delta n/\Delta n_c$. In the limit $\Delta n_p = 0$, it can be shown that the relativistic guiding of a long pulse occurs when the laser power satisfies $P \geq P_c$. On the other hand, in the limits $P/P_c << 1$ and $a_0 << 1$, it can be shown that a

parabolic density channel $\Delta n_p = \Delta n r^2 / r_0^2$ can guide a Gaussian laser pulse $a_0^2 \propto e^{-2r^2/r_s^2}$ provided that the channel depth satisfies $\Delta n \geq \Delta n_c$.

This thesis will be concerned with LWFA in which the laser pulse is guided primarily by a preformed plasma density channel, i.e., $\Delta n \approx \Delta n_c$ and $P/P_c << 1$.

2.2.1 Laser Guiding in a Hollow Channel

In this section, the equilibrium transverse profile of a laser pulse guided by a hollow channel is obtained [15]. The hollow channel refers to a cylindrically symmetric step plasma density profile of width d, where the density inside the channel is zero, and the wall thickness is much less than a plasma wavelength: n=0 if r<d, and n=n_0 if r>d. The feedback effect of changes in the plasma density, caused by the laser pulse, on the guided mode is neglected. This effect is expected to remain small as long as $a_0 << 1$.

The mode structure of a hollow plasma channel is similar to the mode structure of an optical fiber with refractive index of unity inside and $\eta_R = ck/\omega = (1-\omega_p^2/\omega^2)^{1/2}$ outside [27]. The lowest order mode supported by a hollow channel in slab geometry (n=0 if |y|<d, and n=n_0 if |y|>d, for all x) is the fundamental TE mode:

$$E_x=E_0 \cos(k_y y)e^{-ikz},\ |y|<d,\quad E_x=E_0 \cos(k_y d)e^{-p(|y|-a)}e^{-ikz},\ |y|>d, \tag{2.19}$$

where $k_y^2=k_0^2-k^2$, $p^2=k^2-k_0^2\eta_R$. From continuity of H_y the dispersion relation is obtained:

$$p= k_y \tan(k_y d).$$

(2.20)

In cylindrical geometry the lowest order mode is the so-called HE_{11} mode [28]. It can be approximated by the linearly polarized LP_{01} mode:

$$c_l = \frac{\varepsilon_0}{2} a^2 \left[\int_0^1 2\pi x dx (J_0(hax))^2 + \int_1^\infty 2\pi x dx \left(\frac{J_0(ha)}{K_0(qa)} K_0(qax) \right)^2 \right],$$

(2.21)

where h and q are laser mode transverse wave numbers inside and outside the channel respectively, $h^2=k_0^2-k^2$, $q^2=k^2-k_0^2\eta_R$, J_0 is the Bessel function of the first kind, and K_0 is the modified bessel function of the second kind. The dispersion relation in cylindrical geometry becomes

$$ha \frac{J_1(ha)}{J_0(ha)} = qa \frac{K_1(qa)}{K_0(qa)},$$

(2.22)

These dispersion relations and field profiles are to be used when designing an accelerator. Channel parameters could be chosen so that there exists a single bound laser mode, in order to avoid laser instabilities [14], [29]. As will be discussed in Section 2.3, the laser amplitude at the channel walls determines the coupling efficiency to the accelerating plasma wave, while the degree of laser penetration into the plasma bulk affects the excitations of unwanted plasma oscillations, the body mode [30]. Thus, even though from the dispersion relations (2.20) and (2.22) it is seen that in a hollow channel a bound mode exists for any channel parameter, however small (with the assumption of

infinite plasma), a channel which is too shallow (small k_p) or too narrow (small d) will have lower efficiency caused by the laser excitation of spurious body modes. On the other hand, the requirement of high laser amplitude at the wall of the channel, for better coupling to the accelerating mode, and the benefit of having a single bound laser mode, limits the value of $k_p d$ from above. For these reasons a value of $k_p d \sim 1$ is thought to be a realistic design value for hollow channel designs.

2.3 Laser Wakefield in Hollow Channels

When an intense short laser pulse propagates in a plasma channel, its ponderomotive potential displaces electrons in the plasma and thus excites a wake-like plasma oscillation. In a hollow channel a single electromagnetic plasma mode is excited by ponderomotive driving of surface currents. Its phase velocity is equal to the laser group velocity, which in the limit $\omega_p^2/\omega^2 \ll 1$ approaches the speed of light.

In slab geometry (n=0 if |y|<d, and n=n_0 if |y|>d, for all x), assuming that $\omega_p^2/\omega^2 \ll 1$, the frequency of this mode is

$$\omega_{ch} = \frac{\omega_p}{\sqrt{1+k_p d}}. \tag{2.23}$$

The fields of this mode inside the channel are

$$E_z(y,z,t) = Ae^{-i(\omega_{ch}t - k_{ch}z)}, E_y(y,z,t) = -\frac{ik_{ch}A}{2} ye^{-i(\omega_{ch}t - k_{ch}z)} = -\frac{v_\phi}{c} B_x,$$

(2.24)

where A is the amplitude of the wakefield mode and $k_{ch} = \omega / v_\phi$ is its wavenumber. The fields of the electromagnetic mode outside the channel, in the plasma, are

$$E_z(y,z,t) = Ae^{-k_p(|y|-d)-i(\omega_{ch}t-k_{ch}z)}, E_y(y,z,t) = -\frac{ik_{ch}A}{2} ye^{-k_p(|y|-d)-i(\omega_{ch}t-k_{ch}z)}$$

(2.25)

The longitudinal electric field inside the channel is not truly constant. The longitudinal and transverse fields in the exact solution of Maxwell's equations change as hyperbolic cosine and sine respectively, with the spatial frequency $k_{\perp c}d \sim k_p d\ \omega_{ch}/\omega$. We neglect this variation because, the plasma frequency to laser frequency ratio, desireable for a LWFA accelerating section is around 50, and the assumption $\omega_p^2/\omega^2 << 1$ holds true. The amplitude of the electromagnetic wake excited by a laser pulse with ponderomotive potential $f = \frac{mc^2 a_0^2}{4e}$, assuming that $f = f(\xi, x)$, where $\xi = z - ct$, is

$$A = k_{ch}^2 \int_{\xi}^{\infty} d\xi' \cos[k_{ch}(\xi - \xi')] f(\xi', y = d).$$

(2.26)

In addition to the electromagnetic mode, an electrostatic oscillation is excited with frequency equal to the plasma frequency in the bulk of the plasma walls. The amplitude of the electric field of this electrostatic mode is zero at both the channel boundary and inside the channel, reaches a peak at a distance of order $1/k_p$ into the plasma, and decays away at large distances.

In cylindrical geometry, the frequency of the electromagnetic mode is

$$\omega_w = \frac{\omega_p}{\sqrt{1 + k_p d \frac{K_0(k_p d)}{2K_1(k_p d)}}}, \tag{2.27}$$

where K's are the modified Bessel functions of the second kind.

The fields of this mode inside the channel are

$$E_z(r,z,t) = Ce^{-i(\omega_w t - k_w z)}, E_r(r,z,t) = -\frac{ik_w C}{2} re^{-i(\omega_w t - k_w z)}, \tag{2.28}$$

Outside the channel the electromagnetic mode fields are

$$E_z(r,z,t) = C\frac{K_0(k_p r)}{K_0(k_p d)} e^{-i(\omega_w t - k_w z)}, \tag{2.29}$$

$$E_r(r,z,t) = -\frac{ik_w C}{k_p}\frac{K_1(k_p r)}{K_0(k_p d)} e^{-i(\omega_w t - k_w z)}. \tag{2.30}$$

The amplitude of the electromagnetic wake excited by a laser pulse with ponderomotive potential $f = \frac{mc^2 a_0^2}{4e}$, assuming that $f = f(\xi, x)$, where $\xi = z - ct$, is

$$C = k_w^2 \int_{\xi}^{\infty} d\xi' \cos[k_w(\xi - \xi')] f(\xi', r = d). \tag{2.31}$$

In conclusion, a guided laser pulse with duration matched to the wake mode period will excite the high accelerating fields over many Rayleigh lengths. A guiding channel needs to satisfy two main criteria. First, the wake mode of such a channel should be resonant with the driving laser pulse. For a parabolic channel this requires that the driving

laser pulse length be matched to the channel density on axis. In a hollow channel, the wake dispersion relation should be taken into account, when calculating the plasma density needed. Second, the channel depth in a parabolic channel must exceed the critical depth for guiding. And, although a hollow channel supports a guided laser mode independently of its height or depth, experimental designs should not depart from channels with $k_p a \sim 1$, as discussed in Section 2.3.1. Creation of channels suitable for guiding and wake excitation is the focus of Chapter 3.

3 Ignitor – Heater Plasma Channel Creation Scheme

3.1 Channel Formation

3.1.1 Introduction

The guiding and wakefield excitation requires development of plasma channels in a controllable and reproducible way. The first technique for channel production relied on hydrodynamic expansion of a laser produced and laser heated plasma [8]. Long plasmas with a small transverse size were created by focusing a relatively long (100 ps) energetic (200 mJ) laser pulse to a line focus with an axicon lens, in a vacuum chamber filled with a gas mixture of Ar and N_2O. After the ionization phase, the laser pulse heated the plasma via inverse bremsstrahlung. The resulting hydrodynamic expansion led to a time-dependent density profile with a minimum on-axis. To demonstrate that such channels were capable of guiding laser pulses, a second laser pulse was injected into this channel at various time delay. For short delay times, the channel was fairly shallow and supported only the fundamental laser mode. For longer delay times, the channel became deeper and wider, thereby allowing higher order modes to propagate. Pulse propagation over distances of up to 70 Rayleigh lengths (about 2.2 cm) of moderately intense laser pulses ($< 5\text{x}10^{14}$ W/cm^2), with pulse lengths much larger than the plasma period, was demonstrated in these experiments [8].

In general, to produce the channel, the laser pulse must satisfy the following requirements. It has to be sufficiently intense to ionize the gas and it has to heat the

plasma to a high enough temperature on a time scale comparable with characteristic hydrodynamic blowout time l/c_s, where l is characteristic size of the plasma and $c_s=[Zk_B(T_e+T_i)/m_i]^{1/2}$ is the ion acoustic speed [34].

Although the initial channeling experiments [8] clearly demonstrated the possibility of guiding laser pulses in plasma channels, the experimental parameters did not meet the requirements of LWFA. In order to excite a large wakefield oscillation, the intensity of the guided pulse has to be on the order of 10^{18} W/cm^2, i.e. two to three orders of magnitude higher. When such an intense laser pulse is brought to focus in air or high pressure gas, such as used in experiments of reference [8], ionization induced refraction [31] will occur, which negatively affects the focusing of the laser pulse. The front of a laser pulse ionizes the gas. Later portions of the pulse propagate through partially ionized gas that has a radial plasma density distribution with a maximum on axis. A plasma with such density distribution acts as a defocusing lens, thereby limiting the maximum achieved intensity. In order to overcome this limitation, a gas jet is required. A gas jet supplies neutral gas in a localized stream or jet into an evacuated chamber. In this way, if the guiding channel is created across the full width of the jet, the driving laser pulse never interacts with neutral gas and does not experience ionization refraction, provided the channel plasma is ionized deeply enough.

In addition, a laser pulse of such high intensity would further ionize any atom not deeply enough ionized by the channel forming pulses. The change in the plasma density transverse profile from additional ionization, as well as the ionization process itself, will affect the propagation of the laser pulse and the properties of the wake in a complicated, adverse manner. This precludes the use of easily ionizable additives such as N_2O. To overcome the effects of additional ionization by the exciting pulse, hydrogen or deeply ionized nitrogen are chosen as the neutral gas for the guiding experiments. Laser and collisional ionization during the channel formation process is expected to result in a

deeply ionized gas near the axis of the channel.

To determine the requirements on the channel forming laser pulses, we next discuss the physics of laser ionization and inverse bremsstrahlung heating in gases. This leads to a new channel formation technique, the Ignitor-Heater method, described in Section 3.1.4.

3.1.2 Ionization

Laser ionization of H_2 can be modeled quite accurately through tunneling, or Coulomb Barrier Suppression Ionization (BSI) [32].

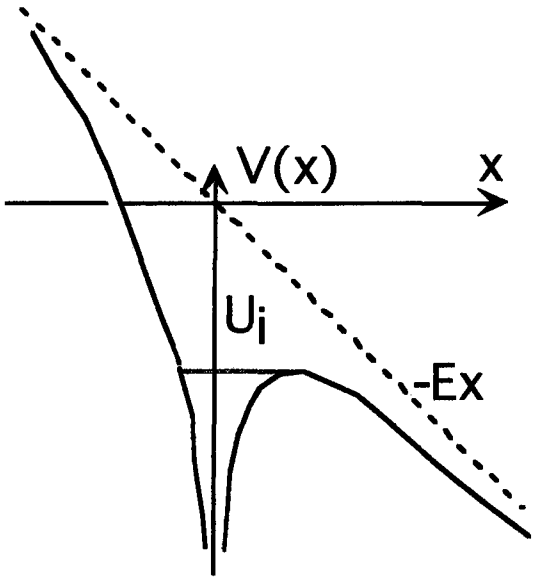

Figure 3-1

The Coulomb potential associated with a field of an atom with a quasi-static laser field E

BSI is a one-dimensional model in which the total electrostatic potential V(x) for the electron is modeled as the superposition of the Coulomb potential associated with a field of an atom and a quasi-static laser field E, Figure 3-1,

$$V(x) = -\frac{Ze}{|x|} - Ex. \tag{3.1}$$

BSI assumes that the time it takes an electron to tunnel through the barrier is short, compared to the period of laser field. The potential V(x) has a local maximum. As the external field strength is increased, the height of the Coulomb barrier is suppressed. According to BSI, the ionization occurs when the local maximum of V(x) reaches the ionization potential, U_i,/e. The electric field at which that happens is

$$E = \frac{U_i^2}{4e^3 Z}. \tag{3.2}$$

Setting this static electric field equal to the peak electric field of the laser, the expression for appearance intensity is obtained,

$$I_{app} = \frac{cU_i^4}{128\pi e^6 Z^2} = 4.00 \times 10^9 \frac{U_i^4(eV)}{Z^2} (W/cm^2). \tag{3.3}$$

Therefore, the intensity of the laser pulse, needed for channel creation in hydrogen, has to be ~1.37×10^{14} W/cm^2. It is important to note that once partial ionization has occurred, and plasma heating through inverse Bremsstrahlung takes place, collisional ionization is expected to play a significant role as an additional mechanism for plasma creation.

3.1.3 Inverse Bremsstrahlung Heating

After a substantial amount of atoms is ionized, the laser pulse heats the plasma by transferring a part of its energy to electrons when the electrons collide with an ion or a

neutral atom. In Coulomb barrier suppression regime nearly full ionization is achieved rapidly for intensities ~10^{14} W/cm^2 [33]. In this section electron-ion collisions are assumed to be the main mechanism for plasma heating.

It should be noted that electron-electron collisions, although present and effective in thermalizing the velocity distribution of plasma electrons, do not contribute to the energy exchangebetween the laser and the plasma [36]. In the parameter regime of this experiment $T_e \le 100eV$, n=7×10^{17} cm^{-3}, the Debye length $\lambda_D = \sqrt{\frac{kT}{4\pi ne^2}} = \frac{V_{th}}{\omega_p} \le 0.07\mu m$ is much smaller than the wavelength of the laser pulse $\lambda = 0.8\mu m$. The net exchange of energy between the laser wave and the electrons during electron-electron collisions is the net change in the product $e\vec{V}\vec{E}$.

The rate of energy transfer is well approximated by one ponderomotive energy per collision,

$$\frac{d\varepsilon}{dt} = \nu_{brem} \frac{mc^2 a_0^2}{4}, \tag{3.4}$$

where ν_{brem} is the collision rate for momentum transfer. When the electron quiver velocity ca_0 is smaller than the electron thermal velocity V_{th}, the small angle scattering Bremsstrahlung rate approaches the classical expression [34]

$$\nu_{ei} = \frac{\omega_p^2 Ze^2 m^{1/2}}{3\sqrt{\pi/2}(k_B T)^{3/2}} \ln\Lambda, \tag{3.5}$$

where $\Lambda = \sqrt{2}\lambda_D \omega_p / \omega r_0$ [35], [36], [37], and [38] is the Coulomb logarithm modified for the presence of the oscillating field, $r_0 = \frac{e^2}{kT}$ is the distance of closest approach, and a plasma with a Maxwellian distribution of temperature T for electrons was assumed. The reason for modifying the Coulomb logarithm in this manner is that only a collision, that happens fast on the time scale of laser period, will be effective in transferring energy to

the electrons.

For $ca_0/V_{th}>1$, an approximate expression can be obtained [35] by using a best fit of the numerical integration of the results of Silin's model [38]:

$$\nu_{ei} = \frac{\omega_p Z}{\pi^2}\left(\frac{1}{n\lambda_D^3}\right)\left(\frac{V_{th}}{ca_0}\right)^3\left(\ln\left(\frac{ca_0}{2V_{th}}\right)+1\right)\ln\Lambda. \qquad (3.6)$$

The contribution of large angle collisions, or collisions with impact parameter $\rho < r_0$, has not been found rigorously up to this date. However, because of the change in the largest impact parameter in the expression for the Coulomb logarithm, this regime becomes important when V_{th}/ω approaches r_0, which will happen before the plasma becomes strongly coupled, because $\omega >> \omega_p$: for the experimental parameters of $k_B T = 1eV$, $n=7\times10^{17}$ cm^{-3}, the modified coulomb logarithm is -1.73, while classical coulomb logarithm is 2.1. This is due to the fact that the time it takes an electron with $\rho = r_0$ to pass by the ion is larger than laser period, and the net energy exchange is zero, and that only the collisions with the impact parameter $\rho < V_{th}/\omega$ will contribute to heating. At low temperatures, $V_{th}/\omega \le r_0$, other processes may contribute to the heating besides the large angle scattering: inverse Bremsstrahlung from electron-neutral collisions, velocity imparted to electrons if ionization occurred off-peak of the electric field for linearly polarized laser pulse, etc. For instance, ionization temperature is on the order of the ponderomotive potential (oscillation energy could be transferred into temperature by electron-electron collisions), which for laser intensity $I=5\times10^{13}$ W/cm^2 is ~3 eV. From this point on, in the calculations of this section it is assumed that the initial plasma temperature is 4 eV.

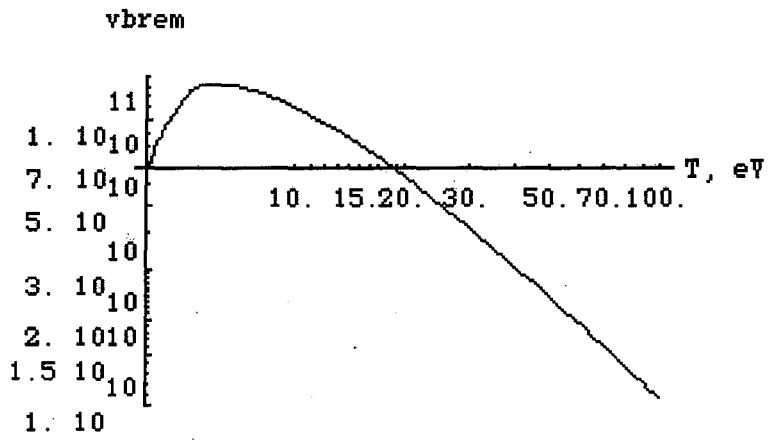

Figure 3-2

Inverse Bremsstrahlung collision frequency vs. temperature, $I=5\times10^{13}$ W/cm^2, $n=7\times10^{17}$ cm^{-3}.

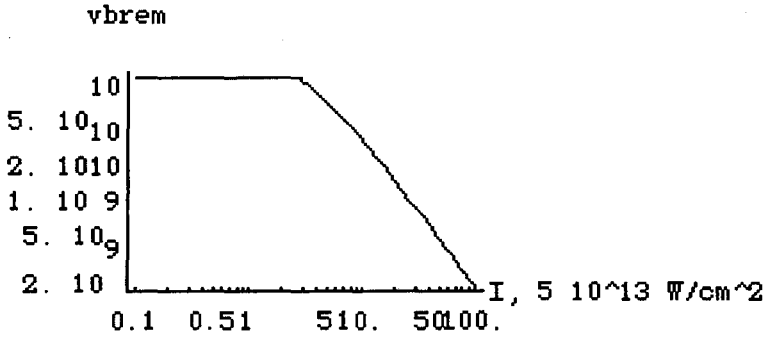

Figure 3-3

Inverse Bremsstrahlung collision frequency vs. laser intensity, T=15eV, $n=7\times10^{17}$ cm^{-3}.

The plasma temperature evolution is governed by equation

$$\frac{3}{2}k_B\frac{d}{dt}T = \nu_{brem}\frac{mv_{osc}^2}{4} \tag{3.7}$$

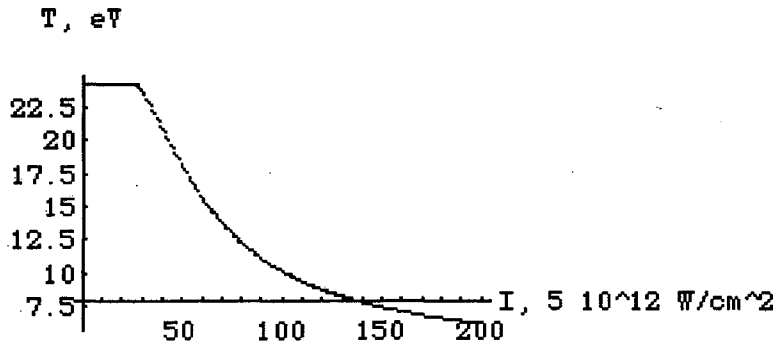

Figure 3-4

Plasma temperature vs. pulse compression ratio: the product $I_0\tau = 500\,Ws/cm^2 = const$, where the laser intensity $I(t) = I_0 e^{-2t^2/\tau^2}$ and the initial plasma temperature $T_{init} = 4\,eV$.

By integrating Eq. (3.7) with the inverse Bremsstrahlung rate given by Eqs. (3.5) and (3.6) (Figures 3-2 and 3-3), the final temperature vs. pulse intensity for a gaussian laser pulse, $I_0\tau = 500\,Ws/cm^2 = const$, is obtained, (Figure 3-4). Here the product of intensity and pulse duration (pulse energy) is kept constant.

For low laser intensities the inverse Bremsstrahlung rate is independent of the laser intensity. The final temperature then depends only on the integral $\int_{-\infty}^{+\infty} \frac{a_0^2}{4} dt \sim \int_{-\infty}^{+\infty} I(t)dt$, and not on the pulselength or peak intensity, as can be seen in Figure 3-4. The dependence of the final temperature on the pulse intensity, with pulse duration held constant, is shown in Figure 3-5.

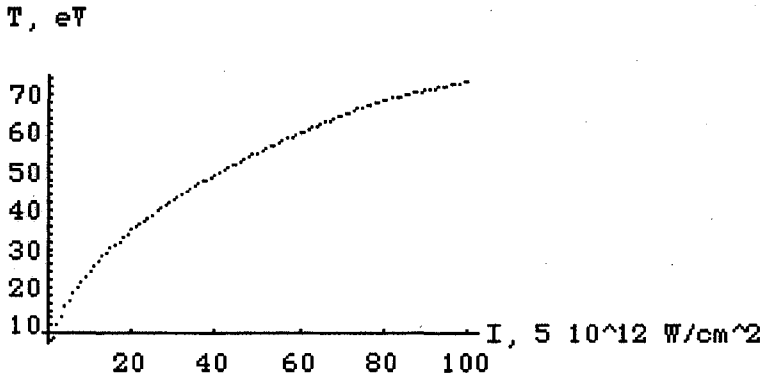

Figure 3-5

Plasma temperature vs. laser peak intensity, where the laser intensity $I(t) = I_0 e^{-2t^2/\tau^2}$, the pulse duration is kept constant at 100 ps, and the initial plasma temperature $T_{init} = 4eV$.

3.1.4 Spark Ignition and Heating

At temperatures around several hundreds of eV, the characteristic time for hydrogen expansion, determined by the ion-acoustic speed, is around 100 ps. In previous experiments [8] a laser pulse with ~160mJ in ~100 ps, focused to a 0.8 cm long line with intensity of ~2×10^{13} W/cm^2, was sufficient to create a plasma channel deep enough for guiding in argon, nitrogen, or xenon. However, as was shown in Section 3.1.1, for hydrogen, the required laser intensity for ionization is ~1.3×10^{14} W/cm^2. On the other hand, from Figure 3-4 it is clear that the optimum intensity for plasma heating is on the order of 1-2×10^{13} W/cm^2. Thus, ionizing the gas and subsequently heating it with one pulse is inefficient. Less laser energy is required to create a channel using two pulses: an ultrashort pulse, ~ 100 fs in duration, to ignite the spark and a stretched ~200 ps long pulse to heat it. In addition, creating laser pulses with sub 100 ps duration requires the

use of a grating compressor, which introduces at least 50% loss of energy.

To summarize, channel creation with the Ignitor-Heater technique requires two perfectly synchronized laser pulses. One, the Ignitor pulse, needs to be sufficiently intense ($>2\times10^{14}$ W/cm^2), which is easily achieved at a minimum expenditure of laser energy by means of an ultrashort pulse. The other, the Heater pulse, has to deliver about 200-300 mJ of energy in 100-200 ps pulse length, to heat the spark sufficiently for creating a shock wave. In the next Chapter we discuss the laser system we have built for LWFA and Ignitor – Heater experiments.

4 Laser System and Experimental Setup

The design of the laser system was guided by the results of the previous chapters and a study of resonant laser wakefield acceleration and laser guiding from a laser builder point of view [39]. We begin with a summary of this design study, followed by a detailed description of the laser system, the implementation of the channel creation Ignitor - Heater concept, as well as the diagnostics for the LWFA experiments.

4.1 Parameter Scalings and Accelerating Stage Design

Closely following the analysis of reference [39], we will next discuss scaling laws that define a parameter regime for a realistic laser driver, a Ti:Al_2O_3 laser system operating at a wavelength of 0.8 μm, which delivers a 50 fs long Gaussian laser pulse with a peak power of 5 TW.

As was shown in Chapter 2, efficient wake excitation requires the driving laser pulse duration to be matched to the laser period. Expressing the plasma density in terms of laser pulse width τ, we obtain

$$n_0[\mathrm{cm}^{-3}] = \frac{\kappa^2 \cdot 3.1 \times 10^{21}}{\tau^2[\mathrm{fs}]}, \tag{4.1}$$

where the plasma density and pulse width are in units of cm^{-3} and femtoseconds respectively, and κ is a numerical factor of order 1 that depends on the laser temporal shape and the channel density profile. For a Gaussian pulse in a homogeneous plasma, $\kappa \cong 0.75$. The resonant density for a 50 fs long Gaussian pulse is about 7×10^{17} cm^{-3}. The plasma wavelength λ_p corresponding to the resonant plasma density can be written as

$$\lambda_p[\mu\mathrm{m}] = 0.6\frac{\tau[\mathrm{fs}]}{\kappa} \tag{4.2}$$

which gives 40 μm for the example. The relativistic group velocity factor $\gamma_g = (1-\beta_g^2)^{-1/2}$ for underdense plasmas is given by $\gamma_g \approx \frac{\omega}{\omega_p} = \frac{\lambda_p}{\lambda_0}$ or , in terms of laser parameters,

$$\gamma_g = 0.6\frac{\tau[\mathrm{fs}]}{\kappa \cdot \lambda_0[\mu\mathrm{m}]}. \tag{4.3}$$

For the numerical example we then have $\gamma_g = 50$. The normalized quiver momentum of an electron in the field of the driving laser can be written as

$$a_0 \cong 6.8\lambda_0[\mu m]\sqrt{\frac{P[TW]}{(r_s[\mu m])^2}}, \tag{4.4}$$

where it is assumed that the laser beam is focused transversely to a lowest-order Gaussian mode with mode size r_S. The maximum on-axis longitudinal electric field strength in the one-dimensional limit is given by [40]

$$E_{max}[GeV/m] \cong 3.8\times 10^{-8}(n_0[cm^{-3}])^{1/2}\frac{a_0^2}{\sqrt{1+\frac{a_0^2}{2}}}. \quad (4.5)$$

Rewriting E_{max} in terms of laser parameters we find

$$E_{max}[GeV/m] \cong 9.74\times 10^4\left(\frac{\lambda_0}{r_s}\right)^2\frac{\kappa P[TW]}{\tau[fs]}. \quad (4.6)$$

Here it is assumed that a_0^2 and the $\delta n/n_0$ are both much less than one.

Assuming that the diffraction of the laser pulse can be overcome by a plasma channel, the maximum distance of acceleration becomes the dephasing length. In Section 6.1 it will be shown that $L_{deph} = \gamma_g^2\lambda_p = \frac{\lambda_p^3}{\lambda_0^2}$. Rewriting L_{deph} in terms of laser parameters we obtain

$$L_{deph} \cong 2.16\times 10^{-7}\frac{\tau^3[fs]}{\kappa^3(\lambda_0[\mu m])^2} \quad (4.7)$$

The maximum energy gain after a dephasing distance is then given by

$$\Delta W_{ch}[MeV] \cong 2.1\times 10^{-2}\frac{\tau^2[fs]}{\kappa^2 r_s^2[\mu m]}P[TW], \quad (4.8)$$

where it is assumed that a laser pulse with $a^2 \propto \exp(-2r^2/r_s^2)$ was guided in a parabolic plasma channel $\Delta n_p = \Delta n_c\frac{r^2}{r_s^2}$. The scaling laws derived here are relevant to a parabolic channel design, where the density gradients do not strongly effect the wakefield. The numerical design results from [39] are summarized in Table 1 for a parabolic channel design. A hollow channel case (calculated from equations of Section 2.4.1), with channel

width $d=r_s$, plasma density zero inside the channel and 1.5×10^{18} cm^{-3} outside (to be resonant with ~50 fs pulse), is also presented for comparison.

Although the accelerating gradient is somewhat stronger in a parabolic channel

Channel geometry	Parabolic	Hollow, $d=r_s$
Laser Power (TW)	5	5
Laser pulse length (fs)	50	50
Plasma density on axis (cm^{-3})	$7\ 10^{17}$	0.
$k_p r_s$	2.7	2.7
Plasma density at $r=r_s$	$1.09\ 10^{18}$	$1.5\ 10^{18}$
Laser strength a_0	0.72	1.
Rayleigh range, (mm)	1.13	1.13
Dephasing length, L_{deph} (mm)	50	23
Accelerating gradient (GeV/m)	16.2	9.1
Energy gain over L_{deph} (GeV)	0.85	0.21
Focusing gradient, (GeV/m^2)	$2.55\ 10^6$	921.

Table 1. Summary of design parameters for a LWFA stage. The design was carried out using 1D equations and was based on available laser technology. Corresponding hollow channel numbers are shown for comparison.

than in a hollow channel, the focusing gradient is much weaker in a hollow channel

(Eq.(2.24)) than in a parabolic channel (Eq. (2.15)). This is due to the fact that in a hollow channel the magnetic field of the electromagnetic mode counteracts the focusing force of the radial electric field, effectively reducing the electric field amplitude by $1/\gamma_{ph}^2$, while in a parabolic channel the wake is mainly electrostatic and the focusing force is proportional to the product of transverse gradient of the laser intensity and longitudinal wake amplitude. A weaker focusing gradient is deemed an advantage of the hollow channel because of the issues of coupling of the electron beam into the LWFA.

4.2 Laser

Guided by the parameter study presented in the previous section we have designed and built a multi-terawatt laser system at the L'OASIS laboratory of the Center for Beam Physics, LBNL. This system produces multiple perfectly time-synchronized pulses with different time structure and energy from a single master oscillator laser. The system allows detailed time resolved studies of laser produced plasma channels and of the laser wake excitation in plasma channels.

4.2.1 Oscillator

The oscillator [41] was constructed based on Kerr-lens modelocking [42] and [43]

in Ti:Sapphire, Figure 4-1.

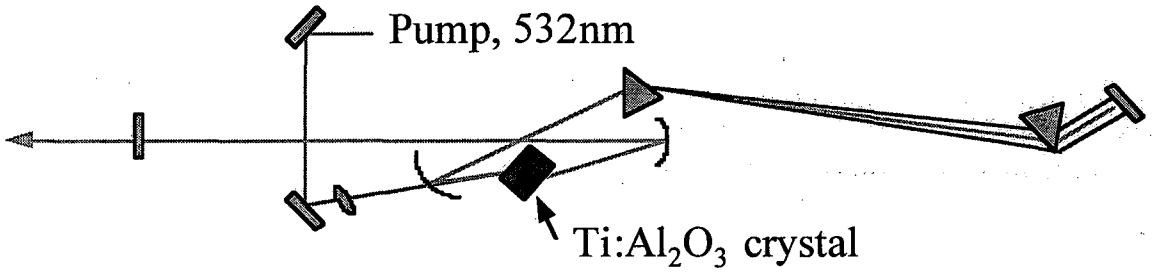

Figure 4-1.

Schematic diagram of Ti:Sapphire oscillator. The oscillator is pumped by an intracavity doubled diode pumped Nd:YAG laser.

Kerr lens mode locking operates in the following manner: the laser-resonator cavity is detuned from the optimum for continuous wave (cw) operation by shortening the effective cavity length. Through addition of a focusing element of proper strength to this shortened cavity, better matching of the cavity mode with the pump beam size at the crystal or, alternatively, smaller diffraction losses will be achieved. The Kerr effect in the Sapphire crystal can provide additional focusing through the dependence of the refractive index on laser intensity: the radial profile of the laser intensity at the crystal, a Gaussian with a maximum on-axis, leads to a radial dependence of the refractive index in the crystal with a maximum on axis, effectively making the crystal a focusing lens. Since the strength of Kerr effect is intensity dependent, a train of short pulses yields a much higher magnitude Kerr lens than a constant amplitude cw radiation, for the same average laser power. For ultra-short pulses, dispersion leads to appreciable pulse-lengthening. Different colors in a laser pulse travel with different velocities. Therefore, a laser pulse after

propagating in a dispersive medium, such as glass or Sapphire, lengthens and its frequency changes from front to back, i.e. it acquires a frequency chirp. This is called group velocity dispersion (GVD). To produce an ultrashort pulse, dispersion compensation is necessary. A prism pair [44] provides the required effect. After going through one prism different colors in the laser beam are propagating at different angles. The second prism collimates the beam, although different colors are still spatially separated. If the beam is made to retrace its path, the beam is reconstructed spatially while the colors in the pulse are rearranged temporally in a manner similar to GVD, only with the opposite direction than in most materials. Thus, by inserting a prism pair into an oscillator cavity, the GVD of other dispersive elements in the oscillator may be exactly compensated (to the second order) provided the distance between prisms is chosen appropriately.

By changing the amount of glass the laser pulse propagates through in one of the prisms, the output pulse length (spectral bandwidth) of the oscillator can be changed. Note, that pulse length control could also be accomplished by a spectrum-limiting slit inserted near the second prism.

The oscillator is pumped with 4 W of 532 nm cw radiation from a diode pumped intracavity doubled Nd:YAG laser. The oscillator lases at about 0.8 μm, which produces a 90 MHz train of pulses with an average power of about 0.25 W. The spectral bandwidth (and hence pulse length) is controllable from about 10 nm to 60 nm with an intracavity slit or a prism pair, Figure 4-2.

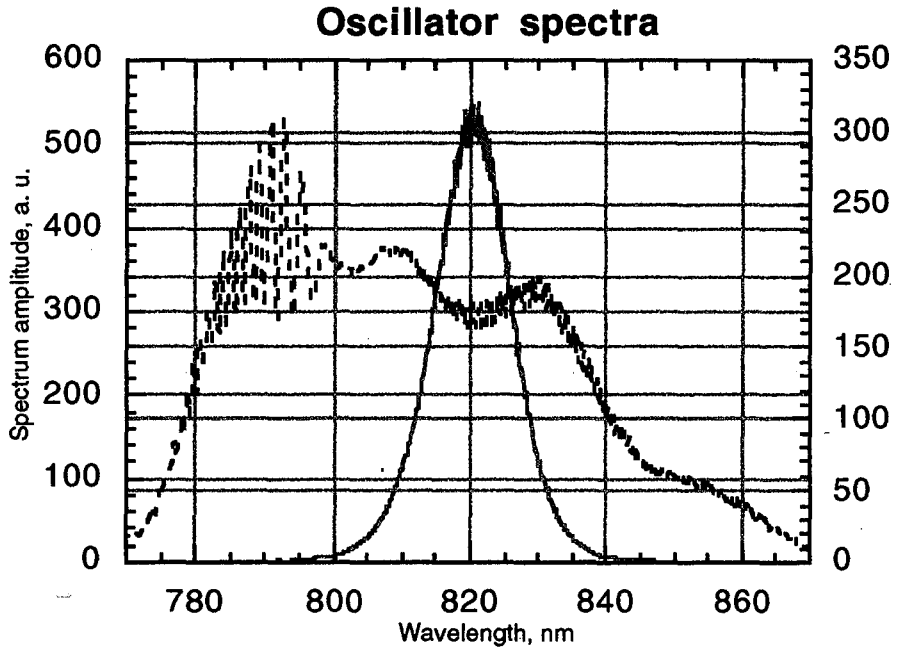

Figure 4-2.

The spectral bandwidth (and hence pulse length) of the oscillator output is controllable from about 10 nm to 60 nm with an intracavity slit or a prism pair. Shown are two typical spectra with close to largest and smallest bandwidths.

The oscillator beam is put through a Faraday isolator, to avoid feed back, and then is input to the stretcher.

4.2.2 **Stretcher**

The all-reflective diffraction grating pulse stretcher [45] is composed of one 1200 gr/mm diffraction grating, a curved mirror, and three plane mirrors, Figure 4-3.

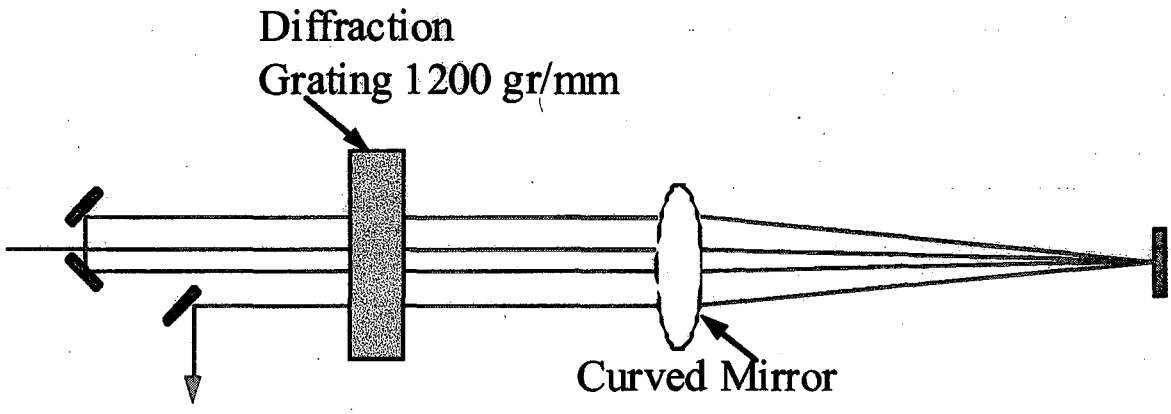

Figure 4-3.

Schematic of the stretcher, view from the top, simplified. The grating is shown as a transparent block and the curved mirror is shown as a lens in order to simplify the schematic, to demonstrate the principle of operation of the stretcher.

After going through the Faraday isolator, the oscillator beam is first reflected by the diffraction grating towards the curved mirror. The curved mirror serves a dual purpose: it reverses the GVD (with respect to the compressor) and it changes the height of the beam so that it can be extracted with a "pick-off" mirror. The beam makes four passes on the grating. After the second pass, the beam is temporally stretched, but spatially very broad. Two additional passes on the grating are necessary to reconstruct the beam spatially, after which the beam is picked off and sent into the cavity of the regenerative amplifier.

4.2.3 Regenerative Amplifier

The beam from the stretcher passes through a height and polarization (vertical to horizontal) changing periscope. It is then injected into the regenerative amplifier by

reflection off a face of the laser rod.

The regenerative amplifier [45] is comprised of a Ti:Al_2O_3 crystal with Brewster cut ends, two Pockel's cells, a quarter wave plate, an output coupler (with strong dependence of the reflectivity on polarization) , and plane cavity mirrors. Optical excitation is achieved by pumping with an intracavity doubled Q-switched Nd:YLF laser. The pump laser generates around 11 W average power at 1 kHz repetition rate. Because the repetition rate of the oscillator is ~ 90 MHz one pulse out of 90,000 needs to be selected. This is done with the quarter wave plate and one Pockel's cell.

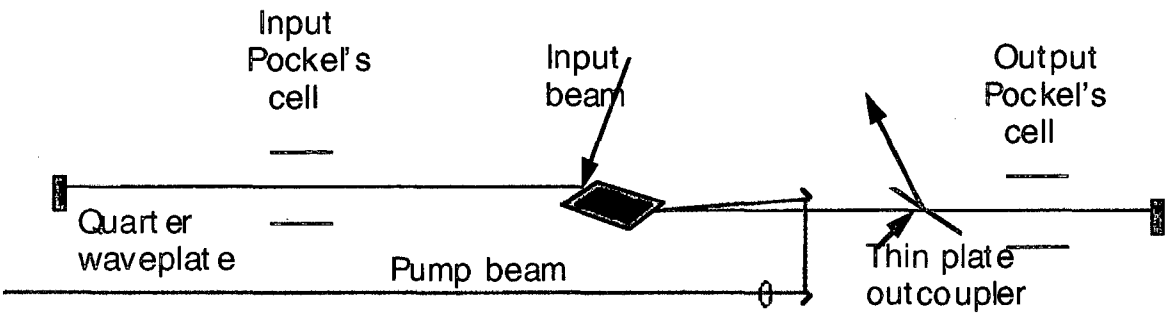

Figure 4-4.

Regenerative amplifier schematic.

With the input Pockel's cell deactivated the pulses pass twice through the quarter wave plate, make a single trip through the regenerative amplifier, pass two more times through the quarterwavelength plate, change polarization from vertical to horizontal, and are ejected from the cavity by a thin plane polarizing beamsplitter-outcoupler.

When the Nd:YLF laser provides a pump pulse to the Ti:Sapphire rod, the input Pockel's cell is activated (a quarterwave voltage (~3.5 kV) is applied) to begin the amplification process. The pulse that has passed through the input Pockel's cell exactly

twice, while it was off, is trapped in the cavity. All the subsequent pulses from the oscillator are rejected on their first pass through the cavity.

After a number of round trips inside the cavity, usually 15-20, the trapped pulse experiences a gain of over 10^6, bringing its energy up to about a saturation level of ~1-1.3 mJ. At this point the quarterwave voltage is applied to the output Pockel's cell, causing a half wave rotation to the trapped pulse after it doublepasses the output Pockel's cell. The pulse is then ejected from the regenerative amplifier by the output coupler plate. Bandwidth control of the oscillator pulses allows bandwidth control of the regeneratively amplified pulses from 10 nm to ~30 nm, Figure 4-5. The upper limit is due to the stretcher bandwidth acceptance limitations and bandwidth narrowing effects in the cavity elements of the regenerative amplifier, such as Fabry-Perot resonator effect in the Pockel's cells and the quarter wave plate and gain narrowing in the crystal. Different bandwidth translates to different pulse duration of the stretched pulse.

A streak camera [46] with picosecond resolution was used to measure the stretched pulse length vs. the output spectrum bandwidth (Figure 4-6). As is evident from this measurement, the stretched pulse duration can be controlled through the oscillator bandwidth from ~100 ps to ~250 ps. This can be used to study the dependence of inverse Bremsstrahlung heating on laser pulse duration (at constant energy).

After exiting the regenerative amplifier, the laser pulse is injected into a three-pass preamplifier.

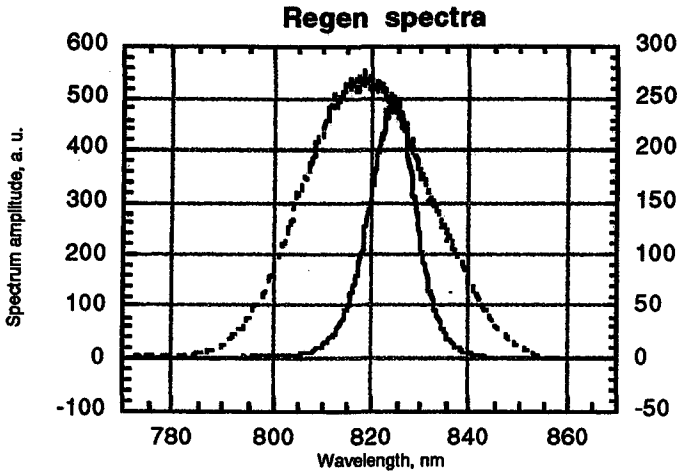

Figure 4-5.

Bandwidth control of the oscillator pulses allows bandwidth control of the regeneratively amplified pulses from 10 nm to ~30 nm. Shown are two typical spectra with about the largest and the smallest bandwidths achieved in the system.

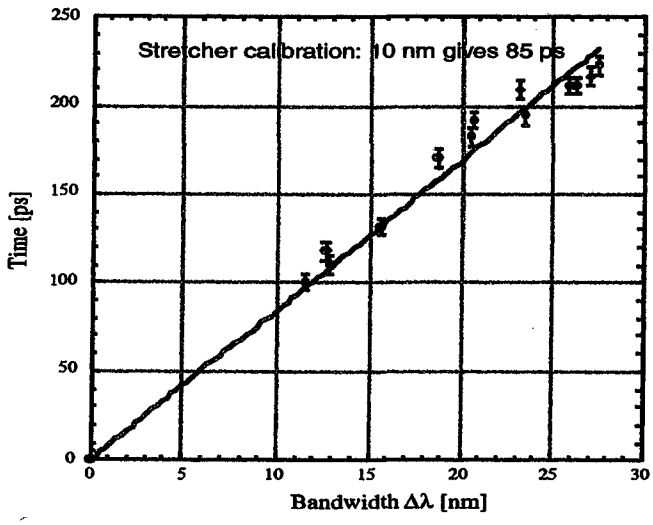

Figure 4-6.

Stretched pulselength vs. the output spectrum bandwidth. Measured using a Soliton K-001 streak camera with XR-200 Photometrics CCD.

4.2.4 Three Pass Preamplifier

The three-pass preamplifier Ti:Al_2O_3 crystal (1 cm diameter, 1.5 cm long), is pumped by typically 380 mJ of 532 nm radiation from a commercial Q-switched, frequency doubled Nd:YAG laser operating at 10 Hz. For a pump fluence on the preamplifier crystal of about 3 J/cm^2 we typically obtain about 50 - 55 mJ per pulse.

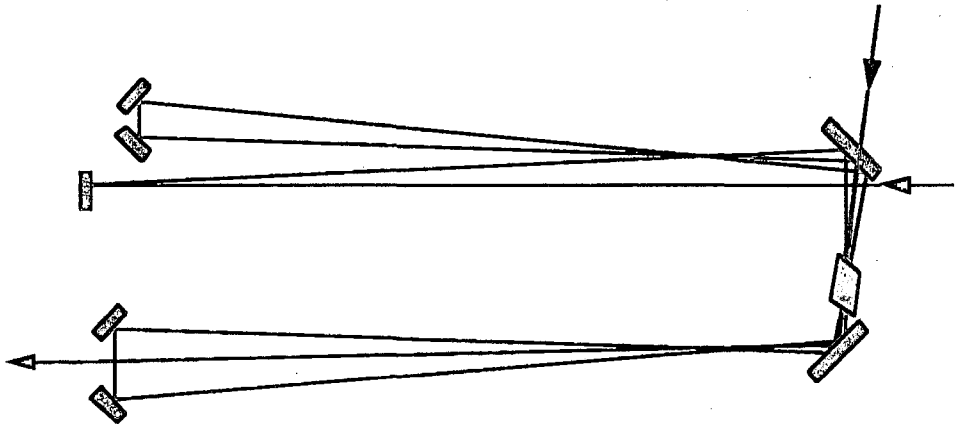

Figure 4-5.

3-Pass pre-amplifier schematic.

This pulse is then injected into the main amplifier.

4.2.5 2+2 Pass Power Amplifier

The main amplifier crystal (1.5 cm diameter, 1.5 cm long) is pumped from both sides with two 9 mm diameter beams containing up to 950 mJ energy (per side) in a 7-8 ns long pulse at 532 nm, Figure 4-6. The 532 nm radiation is produced as follows. A Nd:YAG laser system, lasing at 1064 nm, consisting of an oscillator-amplifier Q-switched

laser generates a 1.2 J energy, 9 ns pulse at 10 Hz with a spatial flat top mode. This mode is relay imaged on the inputs of two amplifier arms, each having two amplifier heads. The ~2 J output power per arm is frequency doubled and relay imaged onto the Ti:Al_2O_3 to maintain a flat top pump profile. After two passes through the main amplifier crystal, the 800 nm pulse is amplified to about 400 mJ.

About 50 % of the pulse energy is then directed through an expanding telescope towards a single grating folded vacuum compressor to produce a pulse with ~ 100 mJ in 70 - 75 fs. The pulse length was measured using a frequency resolved optical gating system (FROG) [47]. This short pulse will be used for wake excitation. The gain saturation in the Ti:Al_2O_3 crystal after two passes is minimal and therefore causes no significant spectral distortion. The remaining pulse double passes the main amplifier again, resulting in an expected energy of 400 - 500 mJ and is not compressed. This long pulse is used for creating the plasma channel. Optical delay lines have been implemented to ensure proper timing between the terawatt pulse, the long pulse, and the blue probe pulse.

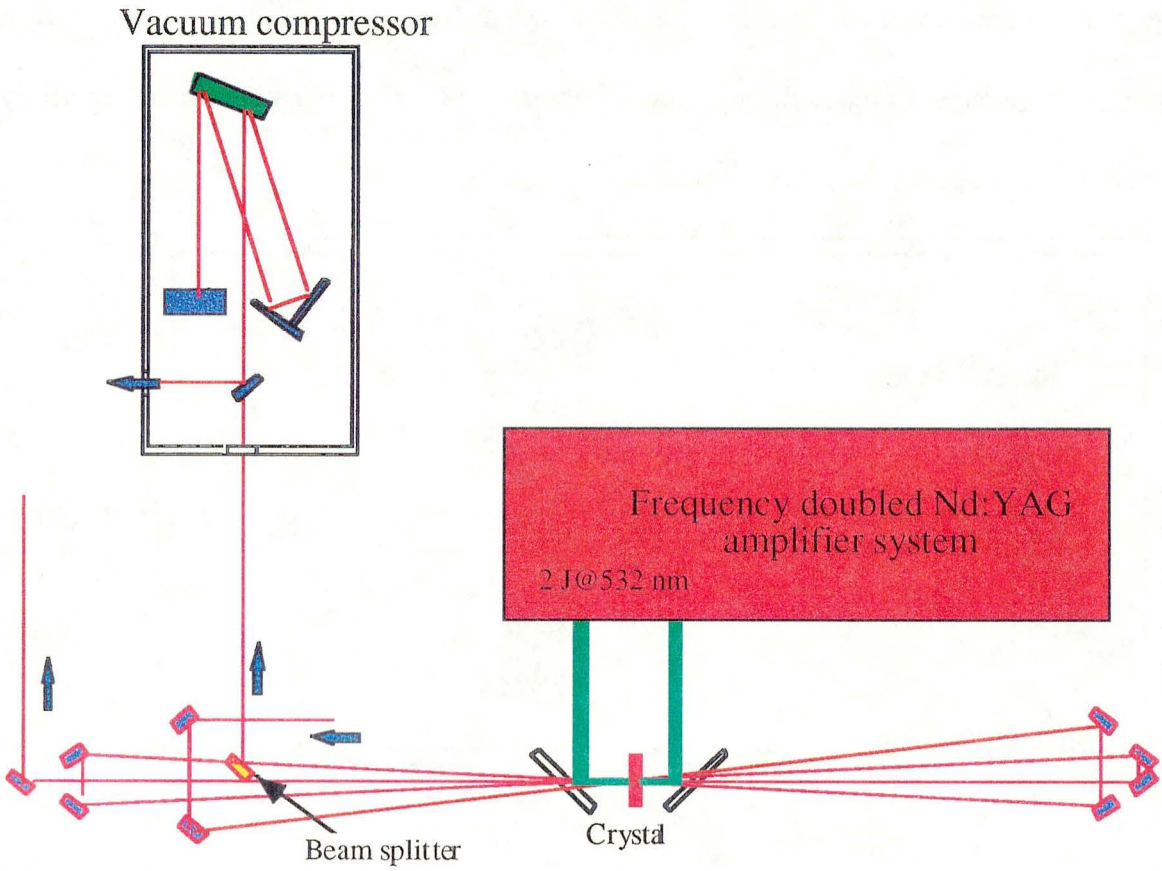

Figure 4-6.

2+2 Pass amplifier and vacuum compressor schematic.

4.2.6 Vacuum Compressor

To achieve the required peak pulse power, a single grating folded vacuum compressor [45] was built to reverse the effect of the stretcher, Figure 4-7. The input beam is reflected by a holographic diffraction grating (120 x 140 mm, 1200 gr/mm) with ~ 90% absolute reflection efficiency at 800 nm towards a horizontal retroreflector. The beam is reflected back at the grating with a horizontal offset of around 2.5 inches. Then, the collimated but spatially broad beam is reflected parallel to the input beam off the

grating towards a vertical retroreflector. After being displaced vertically by two inches, the beam retraces its path through the compressor and exits the compressor spatially reconstructed and temporally compressed.

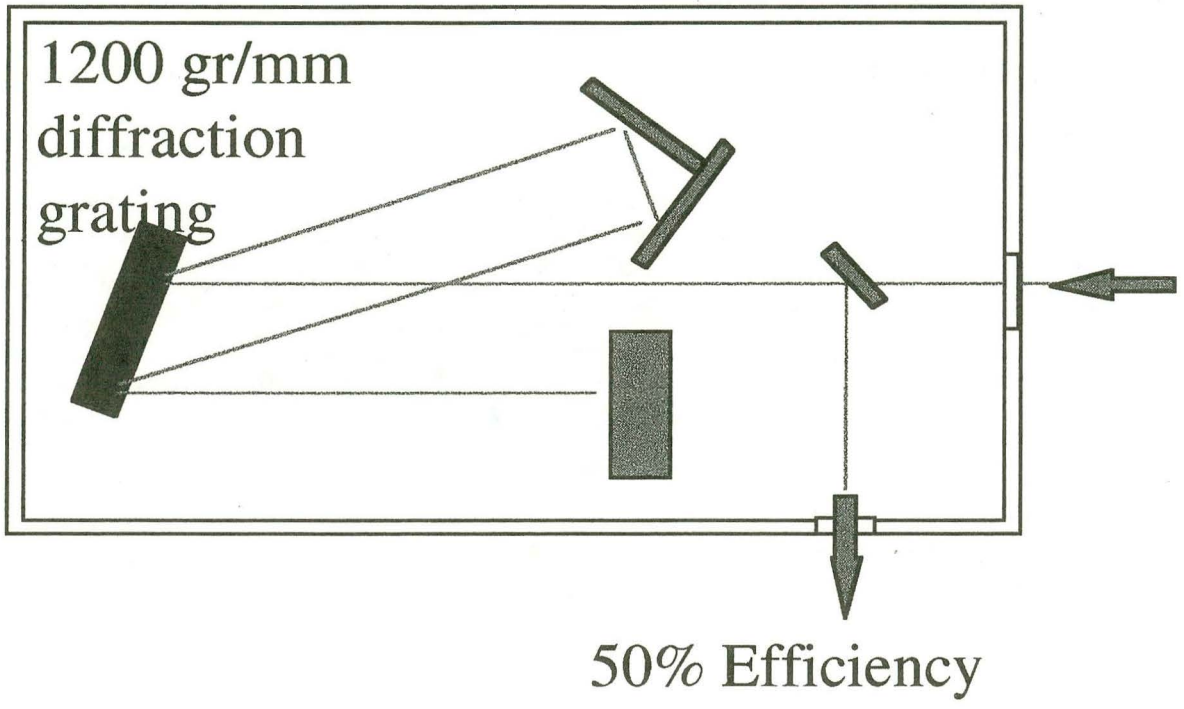

Figure 4-7.

Single grating folded vacuum compressor schematic.

The pulse duration can be adjusted by changing the grating rotation angle and the distance between the horizontal retroreflector and the grating.

The spectrum of the laser pulse narrows after being compressed, mainly due to the spectral dependence of the diffraction grating efficiency and, to a lesser degree, the finite size of the optics. The narrowing was measured to be ~5 nm for a ~28 nm broad input pulse, Figure 4-8.

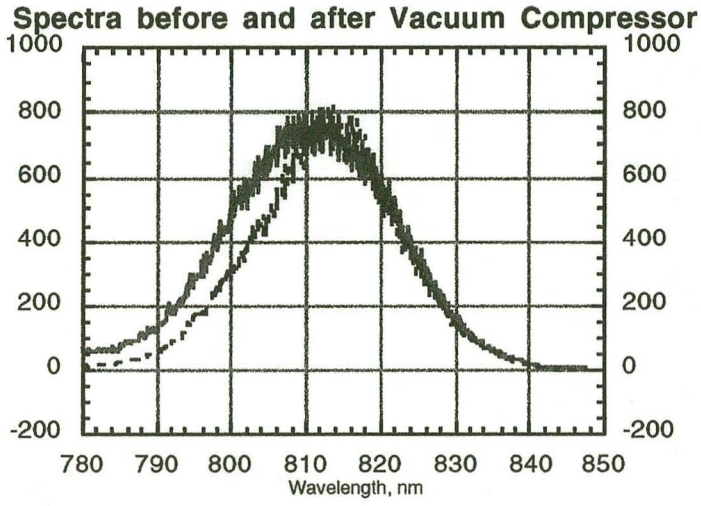

Figure 4-8.

Spectra before and after the vacuum compressor. The narrowing is ~5 nm.

4.3 Longitudinal Mach Zehnder Interferometry With Femtosecond Resolution

A Mach-Zehnder type interferometer with a measured spatial resolution of 4 μm was built to measure line integrated plasma density. This interferometer measures the relative spatial phase shift between two blue (400 nm) 50 fs pulses, one propagating through plasma and one through air. Figure 4-9 shows a schematic of the interferometer setup.

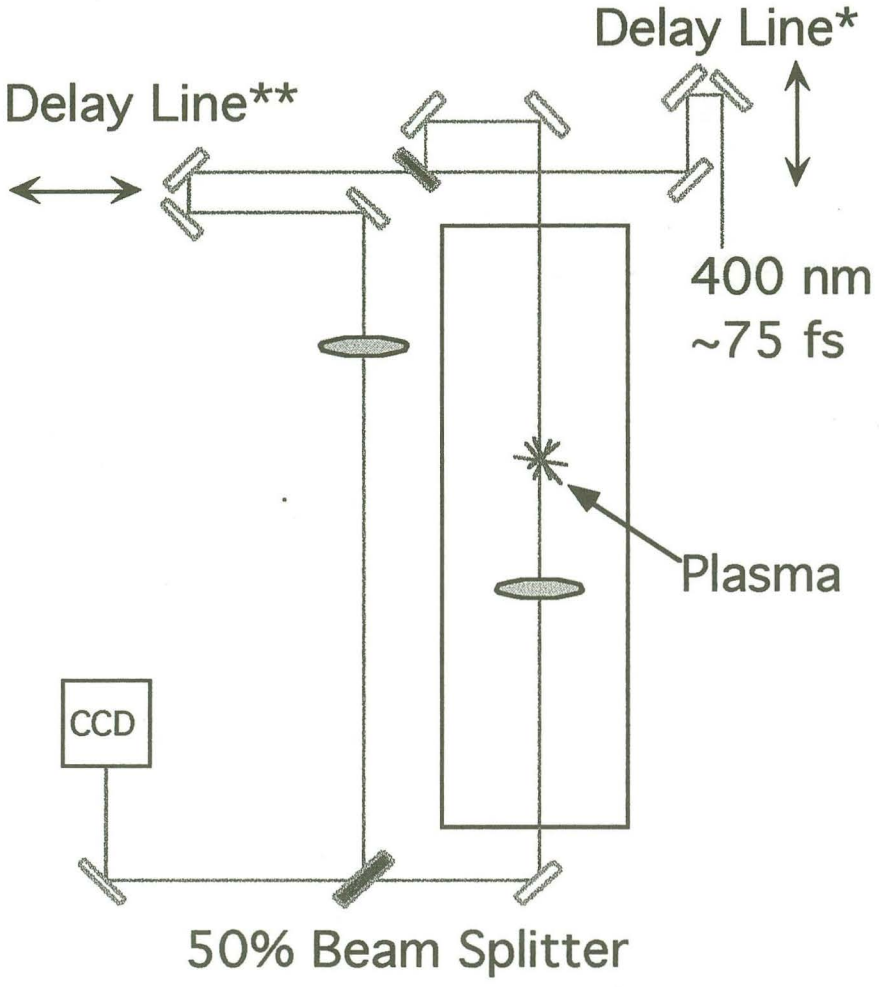

Figure 4-9.

Longitudinal Mach Zehnder interferometry with femtosecond resolution. Interferometer setup schematic.

The blue beam is generated by first compressing ~10% of the regenerative amplifier output with a built-in, scaled down version of the compressor as described in Section 4.1.6, and subsequently frequency doubling in a BBO crystal. A ~60 ns delay line is used to ensure proper timing between the probe pulse and the amplified pulses in the experimental chamber. Upon arrival at the experimental chamber, the beam is divided in a probe and a reference beam, using a 50% beam splitter. The probe, after propagating through the plasma, is recombined with the reference beam, which has propagated through air, to produce a fringe pattern on a CCD camera. The proper arrival time of the two beams,

necessary for temporal overlap, is obtained with a trombone delay line. To image the plasma region onto the CCD camera and to match the radii of curvature of the two beams, a 2 inch diameter 10 cm focal length singlet lens is used into each of the two arms.

Since the blue interferometer beam is perfectly synchronized with the high power beams used in plasma production, the evolution of the 2-D transverse plasma density profile can be measured with a temporal resolution determined by the duration of the blue pulse (~50 fs).

4.4 Ignitor-Heater Channel Production Scheme Implementation

To implement the Ignitor-Heater channel creation scheme (Section 3.1.4), the two laser pulses were combined in a line-focus by means of cylindrical optics onto a gas jet, Figure 4-10. The gas jet was used to avoid ionization induced refraction [48] in a statically filled experimental chamber. The femtosecond intense (~5 10^{14} W/cm^2) Ignitor pulse was focused to a line by reflecting off a cylindrical reflector. The cylindrical reflector is a plano-concave (R=38 mm) cylindrical lens, coated with a dielectric high reflection coating for 45° angle of incidence P-polarized 800 nm radiation. By using a reflective optic we have avoided beam filamentation, self-focusing [49], and other undesirable nonlinear effects in media that would prevent from obtaining a well focused, near diffraction limited beam spot. The Heater pulse was focused with an F/5 refractive cylindrical lens (focal length fl=50mm) at the exact location of the ignitor focus. In addition to the fact that the channel forming beams propagate perpendicularly to the guided pulse, the use of two independent cylindrical optics provides precise independent adjustment of both the positions, angles of incidence, and sizes of the line foci.

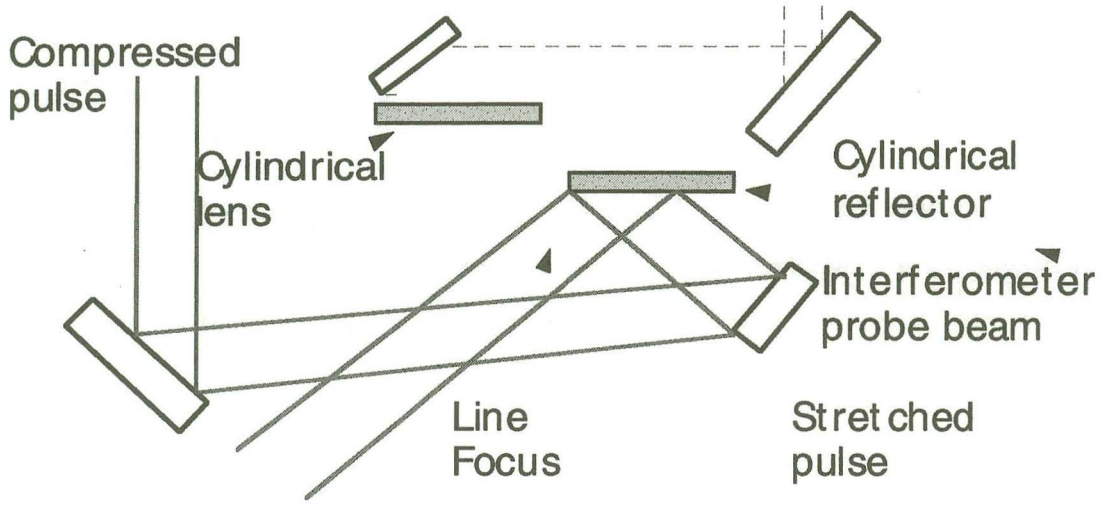

Figure 4-10.

The two pulse combining setup: the femtosecond ignitor pulse (solid lines) is brought to a line focus after reflecting off a cylindrical reflector The cylindrical reflector is a plano-concave (R=38 mm) cylindrical lens, coated with a dielectric high reflection coating for 45° angle of incidence P-polarized 800 nm radiation. The Heater pulse was focused with an F/5 refractive cylindrical lens (focal length fl=50mm) at the exact location of the ignitor focus.

5 Experimental Results

In this Chapter we report on the main results of the experimental implementation of the Ignitor-Heater scheme for channel production, and of the laser guiding in these channels.

In Section 5.1 a chracterization study of a pulsed gas jet, using the Ignitor pulse with two dimensional imaging interferometry is presented. This study served a dual purpose: a) determination of the plasma density achievable in the gas jet and the scalelength of the plasma; b) establishing the minimum required intensity for the Ignitor pulse.

Results of an interferometric study of plasma channel formation, when Ignitor and Heater pulses are combined, are discussed in Section 5.2. An analysis of the experimentally observed hydrodynamics shock waves, ensuing from the laser heat deposition, will be carried out to determine the plasma temperature. The results will be compared with the inverse Bremsstrahlung theoretical model, presented in Chapter 3.

The laser guiding experiments and the coupling efficiency characterization are presented in Section 5.3.

5.1 Gas Jet Characterization

A cylindrical Gas Jet [50] with an orifice opening of 0.762 mm was employed in the experiments. The gas jet body was mounted on a X-Y-Z translation stage. Here

X and Y are horizontal and vertical directions, in the plane orthogonal to the propagation direction of the guided laser beam (Z-direction). The axis of the gas jet coincides with the Y direction.

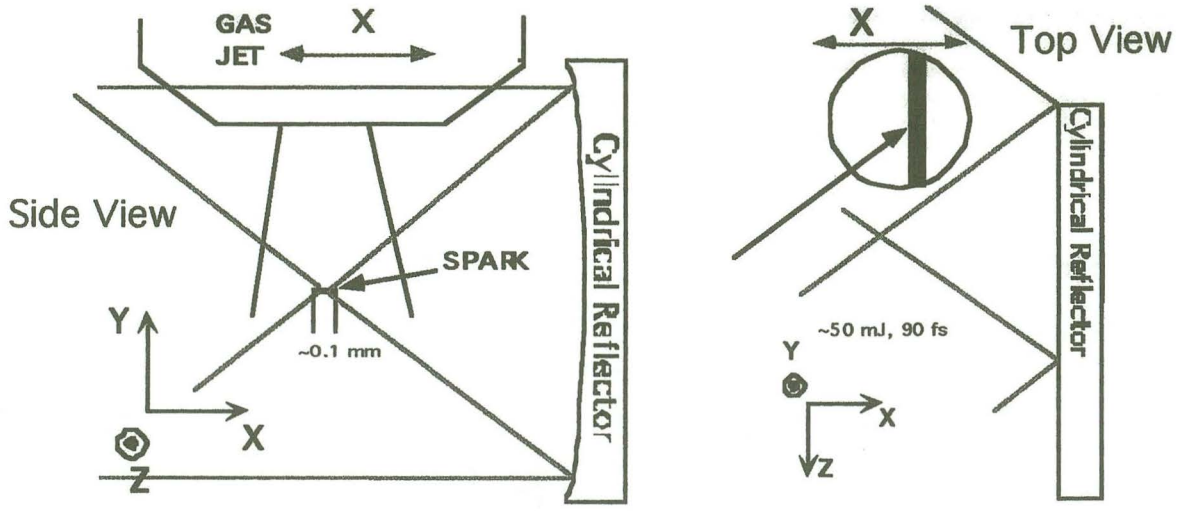

Figure 5-1

The Gas Jet density distribution measurement, side and top views. A small portion of the jet's plume was ionized by the compressed Ti:Sapphire Ignitor pulse focused to a line by a reflective cylindrical lens. The transverse size of the spark was of the order of the Rayleigh length, Z_R~100 micron in X and 5-10 micron in Y (~2w of the focused laser spot), and it extended in Z over the full length of the jet.

The gas density distribution in the jet was measured as follows, a small portion of the jet's plume was ionized by the compressed Ti:Sapphire Ignitor pulse focused to a line by a reflective cylindrical lens. The Mach-Zehnder interferometer was used to record the 2-D phase shift profile (interferogram). The transverse size of the spark was on the order of the Rayleigh length, Z_R~100 micron in X and 5-10 micron in Y (~2w of the focused laser spot), and it extended in Z over the full length of the jet, Figure 5-1. From the interferogram, the maximum phase shift $\Delta\Phi(x)$ [51] was obtained as a function of the

transverse position, X, of the gas jet. An example of an interferogram and of the inferred phase shift is shown in Figure 5-2.

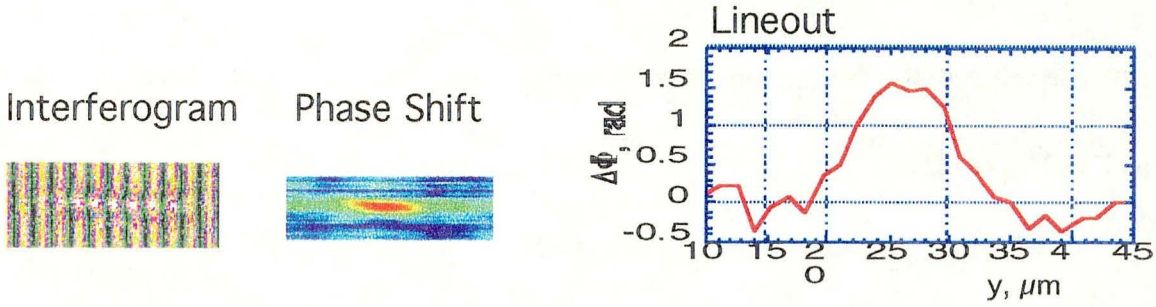

Figure 5-2

Typical interferogram of the plasma produced by the compressed pulse alone, 50 mJ, 90fs. Inferred phase shift: 2-D image and vertical lineout.

Since $\Delta\Phi(x)$ is not a direct measure of the radial density profile, n(r), of the jet, an Abel transform is required to infer the radial density distribution. Indeed, the measured phase shift is proportional to line integral of the gas jet density at a given x:

$$\Delta\Phi(x) = 2\int_{y=0}^{\sqrt{r^2-x^2}} \frac{\omega_p^2(r)}{2\omega_{\text{int}}c}dy = 2\int_{r=x}^{r_0} \frac{4\pi n(r)e^2}{2\omega_{\text{int}}m_0 c}\frac{rdr}{\sqrt{r^2-x^2}}, \tag{5.1}$$

where r_0 is the radius of the gas cylinder, ω_{int} is the frequency of the blue interferometric laser pulse, $\lambda_{\text{int}} = 0.4\,\mu m$.

If the integral of the form of Eq. (5.1) is known, the function itself is given by [52]

$$n(r) = -\frac{2\omega_{\text{int}}m_0 c}{4\pi^2 e^2}\int_{x=r}^{r_0} \frac{\partial\Delta\Phi(x)}{\partial x}\frac{dx}{\sqrt{r^2-x^2}}. \tag{5.2}$$

Because of the derivative in the right hand side of the Eq. (5.2), noise in experimental data is amplified greatly when Abel inversion is performed. To avoid this noise amplification, prior to inverting the data is fit with a smoothing function. The gas jet scan data was fitted with parabolic functions, using a least squares fitting routine. A parabola,

$\Delta\Phi(x) = -\alpha x^2 + \alpha r_0^2$, can be Abel inverted analytically. The resultant function is a quarter of an ellipse: $\frac{4\pi n(r)e^2}{2\omega_{int} m_0 c} = \frac{2}{\pi}\alpha\sqrt{r_0^2 - r^2}$. Thus, the full width at half maximum (FWHM) of the inverted function is related to the base, $2r_0$, of the parabolic fit to $\Delta\Phi(x)$ as $FWHM_{inv} = \sqrt{3}r_0$.

The obtained density distributions, with hydrogen at 1000 psi as the backing gas, at different distances from exit of the jet nozzle are shown in Figure 5-3. The density distribution of the Gas Jet plume with nitrogen at 1000 psi as the backing gas is presented in Figure 5-4. From the data in Figure 5-3 we find that the plume of the gas jet, backed by 1000 psi of hydrogen, expands from 1.2 mm, 0.380 mm below the orifice, to 1.6 mm and 2 mm 1.380 mm and 2.380 mm below the orifice respectively. When backed by 1000 psi of nitrogen, the jet's plume is 0.8 mm in diameter, 0.45 mm below the orifice. The lesser size of the nitrogen plume, compared to that of hydrogen, explains the smaller measured phaseshift in nitrogen than in hydrogen.

These gas jet characterization measurements allow us to calculate absolute plasma density from the measured phaseshift by providing us with information on the gas jet diameter.

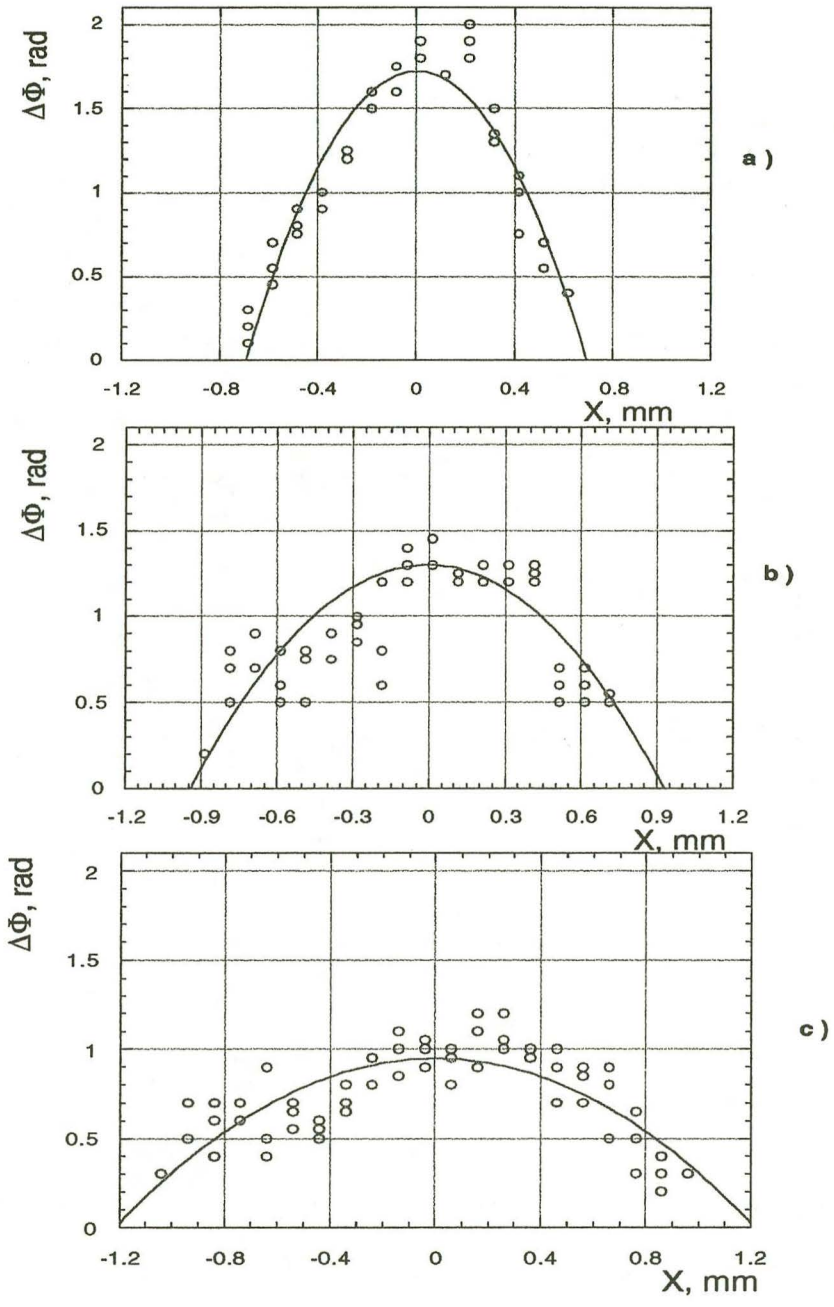

Figure 5-3

Gas Jet transverse scan, 40 mJ, ~75 fs, backing pressure p=1000psi of hydrogen, from the fit: a) z=0.380 mm from the nozzle, FWHM=$1.73r_0$=1.2 mm; b) z=1.380 mm from the nozzle, from the fit: FWHM=$1.73r_0$=1.6 mm; c) , z=2.380 mm from nozzle, from the fit: FWHM=$1.73r_0$=2 mm

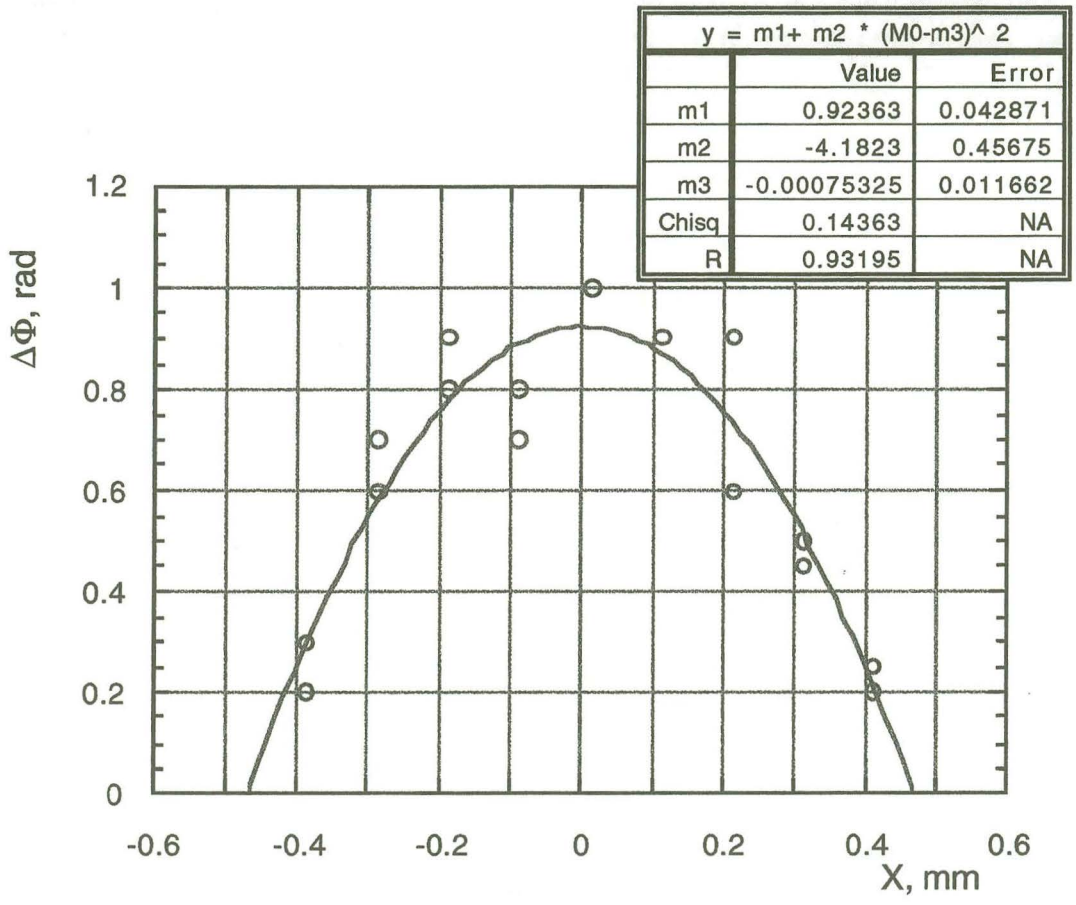

Figure 5-4

Gas Jet transverse scan, 64.5 mJ, ~75 fs, z=0.45 mm from the nozzle,

backing pressure p=1000psi of nitrogen, from the fit: FWHM=1.73 r_0=0.8 mm

To determine the minimum requirements for the Ignitor pulse, ionization curves, spark density vs. ionizing laser intensity were measured. These measurements are important not only as a check of the BSI model, but also because there is a large uncertainty in the spotsize of the Ignitor.

Ionization curves were obtained by using only the Ignitor pulse and measuring electron plasma density for different Ignitor pulse energies. Figure 5-5 and Figure 5-6 show the ionization curves for hydrogen and nitrogen respectively.

To calculate the intensity of the laser pulse at the line focus, the laser spotsize was measured. The long dimension of the line focus was measured by placing a sandblasted, "milky-white", glass plate at the focus of the cylindrical reflector and imaging the plate onto a CCD camera: $w_{long} \approx 6.86\,mm$. Taking the short dimension of the focus to be $5\mu m$ gives the measured threshold intensity for ionization of hydrogen of ~4.3×10^{14} W/cm^2. The threshold for ionization of nitrogen was measured to be around 2×10^{14} W/cm^2.

From the discussion of Section 3.1.1, the appearance ionization intensity for hydrogen is predicted to be, [66], 1.4×10^{14} W/cm^2. The discrepancy with the prediction of Section 3.1.1 could be attributed to at least two factors: the vertical laser focus spotsize uncertainty and the sensitivity of the measurement. The system used in the appearance ionization measurements [37] was able to detect as few as 10 ions, whereas the saturation (i.e. large ionization fraction) occurred for intensities 5 to 10 times higher than the appearance intensity. The interferometric measurement reported here is sensitive to plasma densities larger than about 10^{17}cm^{-3}.

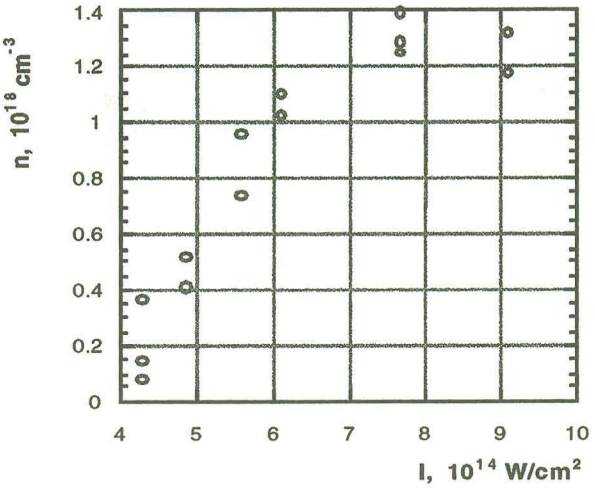

Figure 5-5

Measured peak interferometric phaseshift due to a spark in a hydrogen backed Gas Jet at 1000 psi backing pressure vs. Ignitor pulse energy.

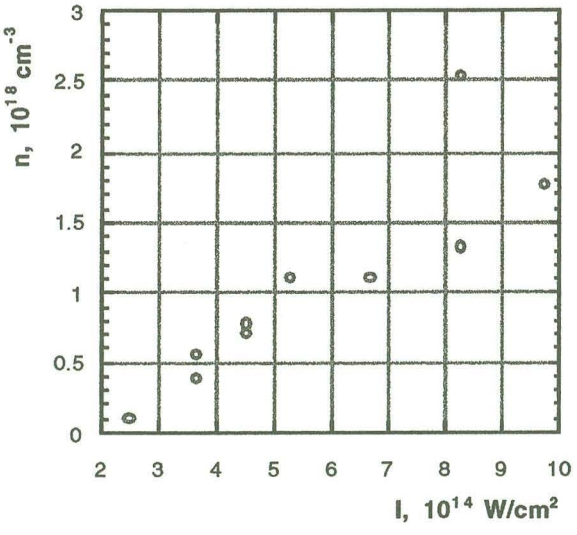

Figure 5-6

Measured peak interferometric phaseshift due to a spark in a nitrogen backed Gas Jet at 1000 psi backing pressure vs. Ignitor pulse energy.

The plateau in the nitrogen ionization curve, Figure 5-6, signifies secondary ionization threshold. The ionization potentials of the first and second electrons of nitrogen

atom are 14.53 eV and 29.60 eV. BSI predicts the ratio of the intensity thresholds for the two states to be around 4, which is in good agreement with the data.

5.2 Ignitor Heater Channel Creation Experiments

In this section the results of channel formation experiments are presented. As discussed previously, channels can be produced by relying on hydrodynamic explosion of a heated plasma. The Ignitor-Heater scheme (Section 4.4) was implemented with 20-40mJ, 75 fs Ignitor pulse and ~270 mJ, 160 ps Heater pulse in nitrogen and hydrogen backed gas jet. We have used 2-D time resolved interferometry to study the formation of the channel.

The interferometric channel formation measurements are analyzed next.

Figure 5-7 and Figure 5-8 show interferograms taken at different delay times of the interferometric pulse in hydrogen and nitrogen respectively. Figure 5-10 presents, calculated from the interferograms of Figure 5-8, channel density profile lineouts in Y-direction for different delay times. The X-size of the channels roughly corresponds to the Rayleigh range of the Ignitor pulse.

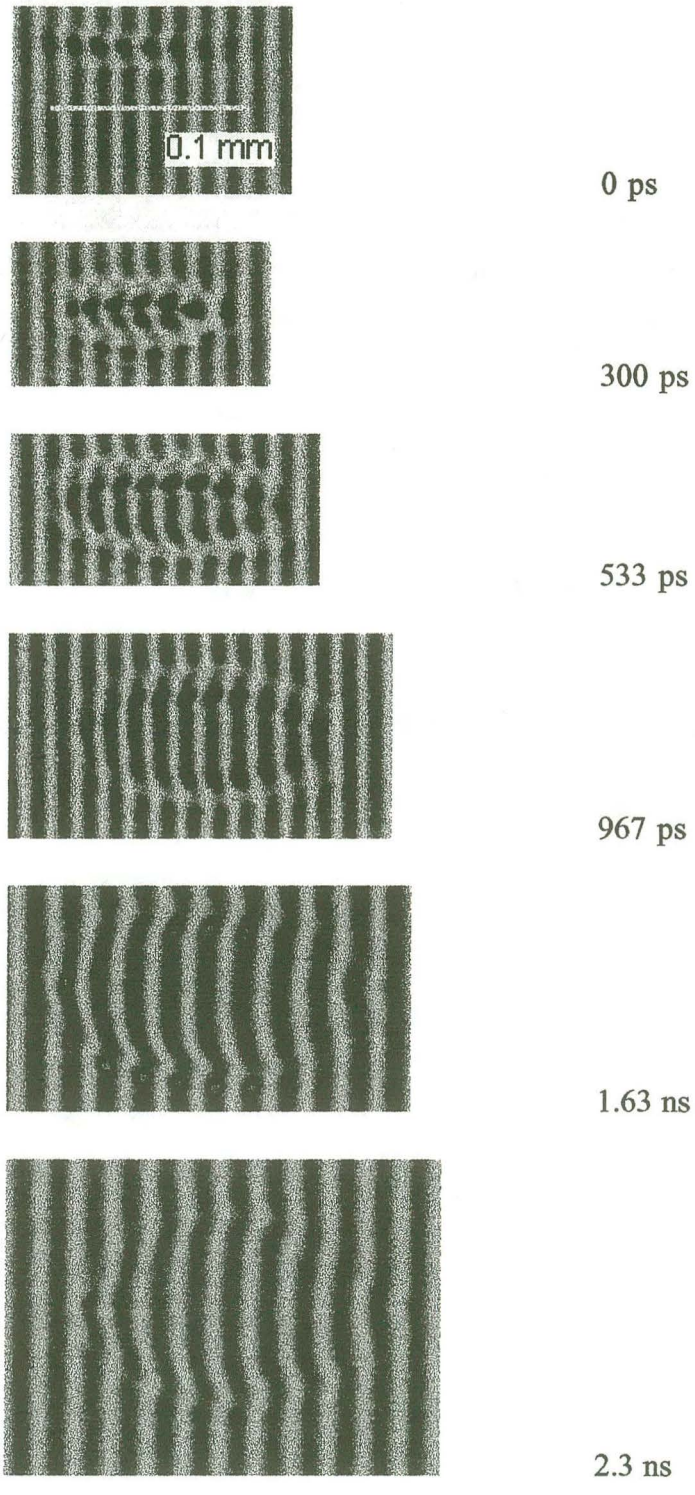

Figure 5-7

Channel formation measurement in hydrogen at different time delays of the interferometer pulse. Hydrogen backed Gas Jet at 1000 psi backing pressure, Ignitor pulse energy 20 mJ, Heater pulse energy 280 mJ.

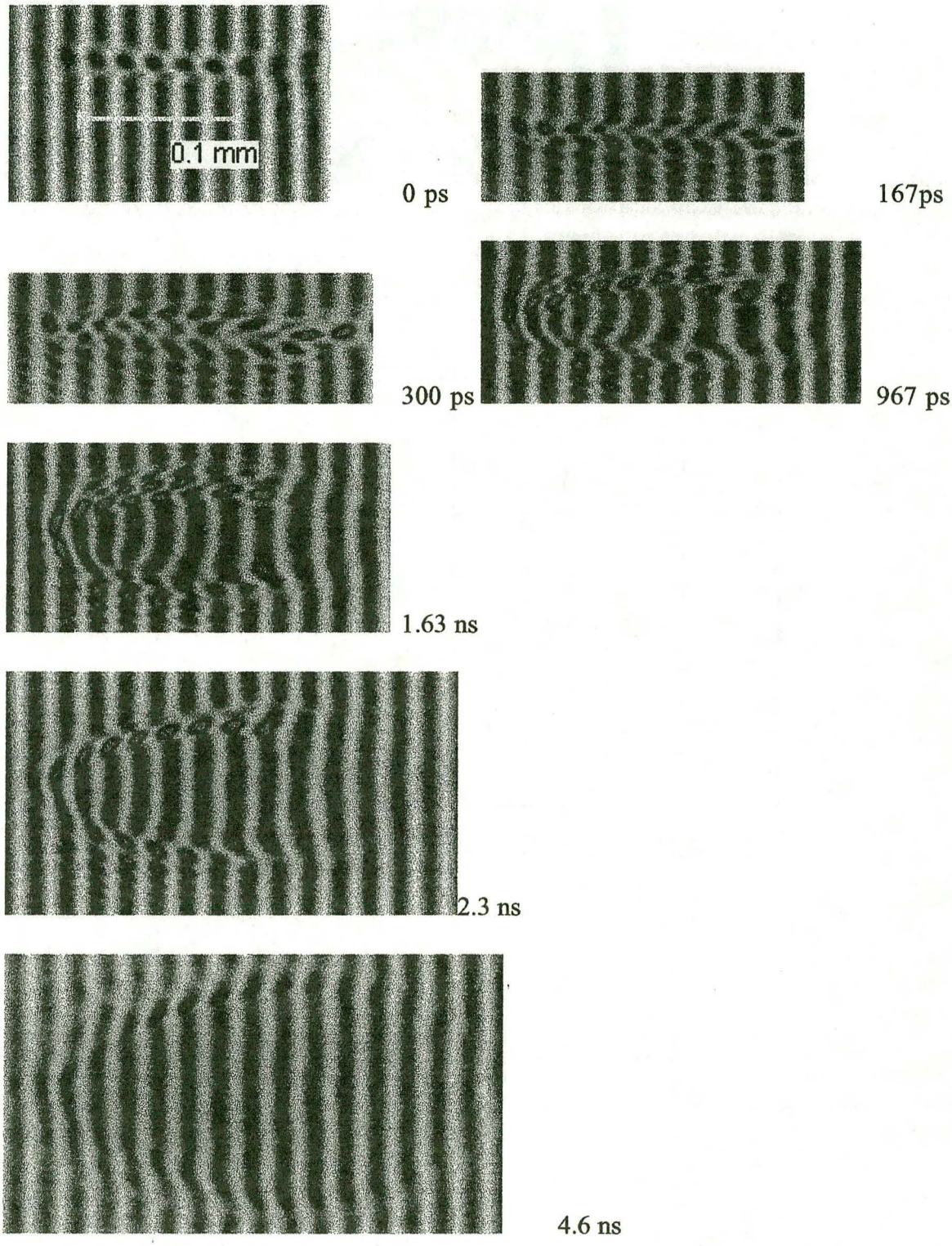

Figure 5-8

Channel formation measurement in nitrogen at different time delays of the interferometer pulse. Nitrogen backed Gas Jet at 1000 psi backing pressure, Ignitor pulse energy 20 mJ, Heater pulse energy 280 mJ.

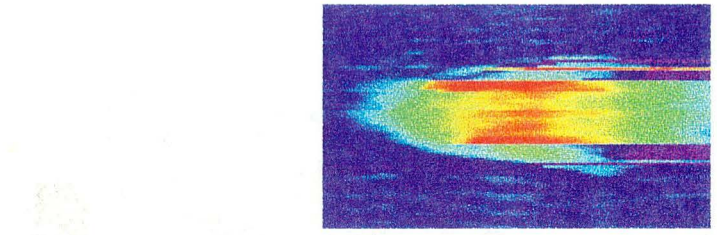

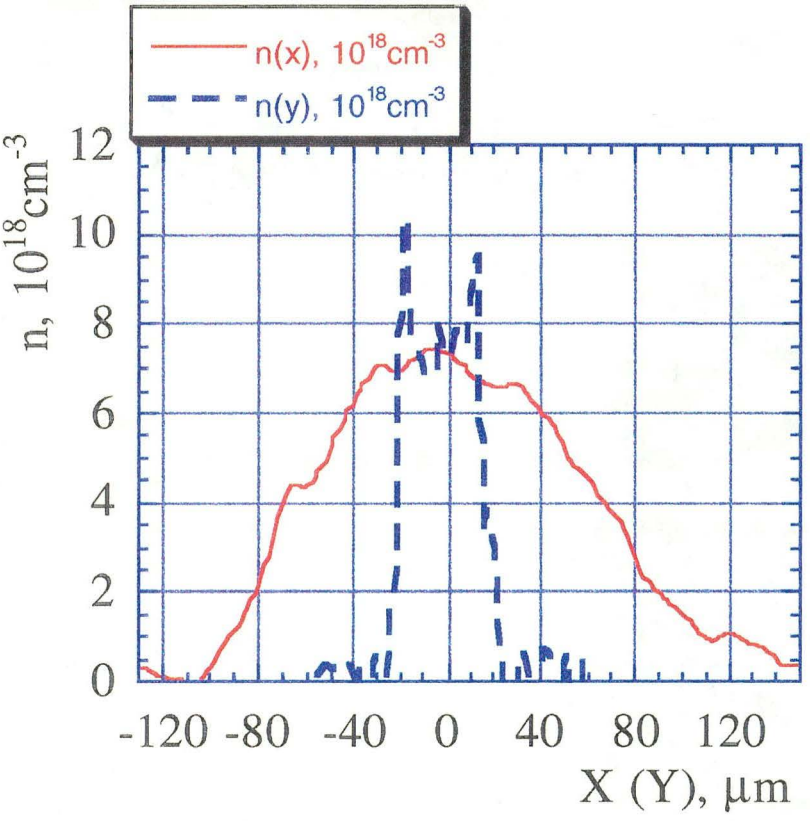

Figure 5-9

The inverted interferogram and its horizontal and vertical density profiles at 1 ns after heating predict guiding properties only in the Y- dimension.

An example of the 2-D plasma density, inferred from an interferogram of Figure 5-8, is given in Figure 5-9. From the density profiles in X and Y directions, also shown in

Figure 5-9, it is seen that a plasma channel is created only in the vertical direction. These channels are expected to guide in Y-direction only.

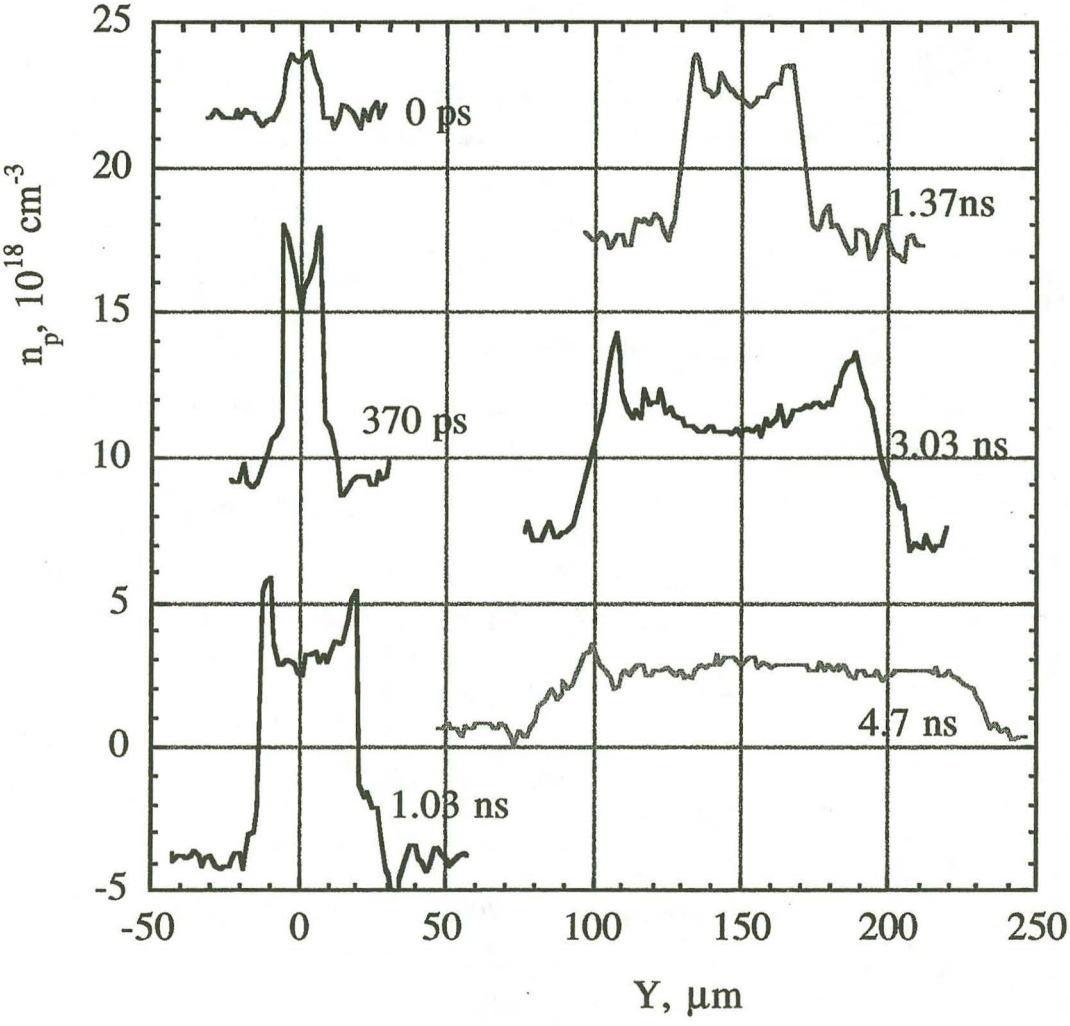

Figure 5-10

Channel density profile lineouts in Y-direction for different delay times. Calculated from the interferograms of Figure 5-8

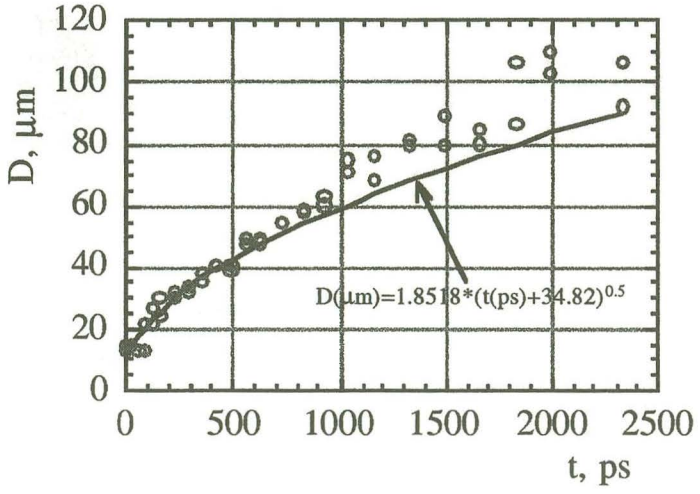

Figure 5-11

Shock front diameter vs. time delay of the interferometer probe pulse. Hydrogen backed Gas Jet at 1000 psi backing pressure, Ignitor pulse energy 40 mJ, Heater pulse energy 280 mJ.

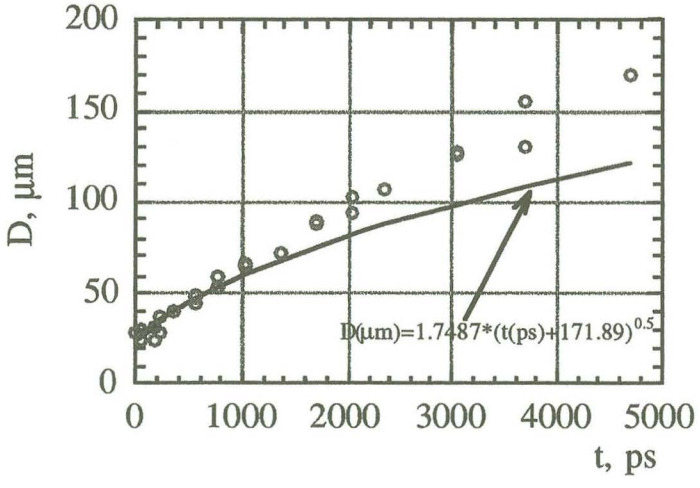

Figure 5-12

Shock front diameter vs. time delay of the interferometer probe pulse. Nitrogen backed Gas Jet at 1000 psi backing pressure, Ignitor pulse energy 40 mJ, Heater pulse energy 280 mJ.

From the interferograms of Figure 5-7 and Figure 5-8 the shock front diameter, D, is found by measuring the separation (in Y) between the points of commencement of the fringe shifts in the middle section of the channel. The results are plotted as a function of time delay in graphs of Figure 5-11 and Figure 5-12.

From the channel size and density dynamics, the initial temperature of the spark is inferred in two ways. By equating the shock speed to ion acoustic speed, the electron temperature can be found. From Sedov's solution of strong explosion in a homogeneous atmosphere [53], a theoretical calculation that relates the energy per unit length in the initial spark to the form of the expansion curve, the temperature can be calculated once again.

5.2.1 Ion Acoustic Shock Expansion

The shock expansion speed is the ion-acoustic speed [34]:

$$V_{ia} = \sqrt{\frac{\gamma \langle Z \rangle k_B T_e}{m_i}}, \tag{5.3}$$

where γ is the ratio of the specific heats, $\langle Z \rangle$ is the average ionization level, k_B is the Boltzman constant, and m_i is the gas atomic mass. From the least squares fits of data in Figure 5-11 and Figure 5-12 the shock speed can be calculated as a function of time. Then, using Eq. (5.3), electron temperature can be inferred, where $\gamma = 5/3$ is used for the electron gas. The calculated shock speeds and the inferred temperature evolutions are plotted in Figure 5-13 and Figure 5-14 for hydrogen and nitrogen correspondingly.

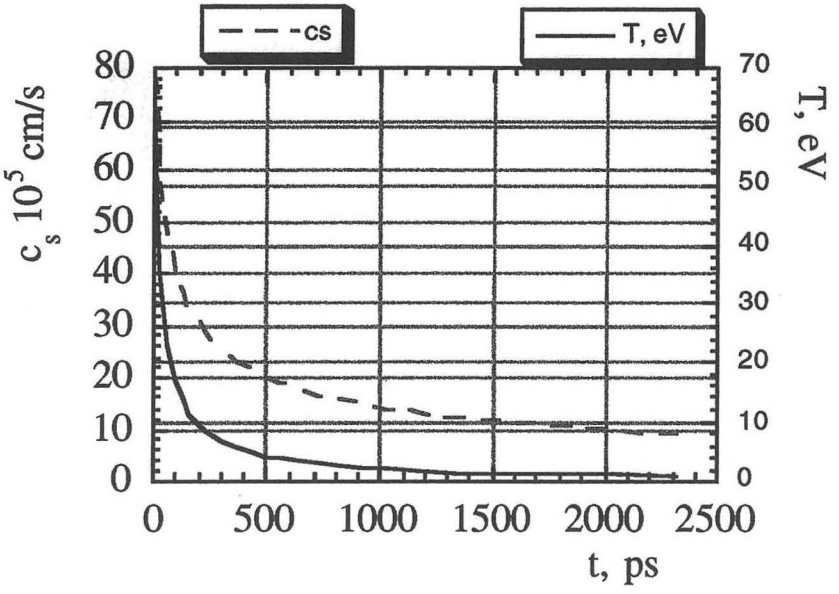

Figure 5-13

Shock front speed vs. time delay of the interferometer probe pulse, from the least squares fit to data in Figure 5-7, solid line, for a hydrogen backed Gas Jet at 1000 psi backing pressure, Ignitor pulse energy 40 mJ, Heater pulse energy 280 mJ. Temperature calculated from Eq. (5.3), dashed line.

The initial temperatures (right after the Heater pulse) are calculated to be ~20 eV and ~120 eV in hydrogen and nitrogen respectively. From the inverse Bremsstahlung theory of Chapter 3, in hydrogen, with $n_I=2\times10^{18}$ cm^{-3}, laser $I=7\times10^{12}$ W/cm^2, and laser pulse duration w=150 ps, the temperature was calculated to be T_e=19 eV. In nitrogen, with $n_I=1.6\times10^{18}$ cm^{-3}, $\langle Z\rangle$=3.5, and the same laser parameters, the temperature was calculated to be T_e=118 eV The energy per unit length can be estimated from the temperature, inferred from the shock propagation speed, and the shock diameter

$$E=\frac{3}{2}n_e k_B T_e \frac{\pi D^2}{4}, \tag{5.4}$$

where n_e is the electron density, calculated from the interferograms of Figure 5-7 and Figure 5-8 to be 3×10^{18} cm^{-3} for hydrogen and 9×10^{18} cm^{-3} for nitrogen at the initial stage of expansion. This calculation gives 0.0267 mJ/cm and 0.89 mJ/cm in hydrogen and nitrogen respectively.

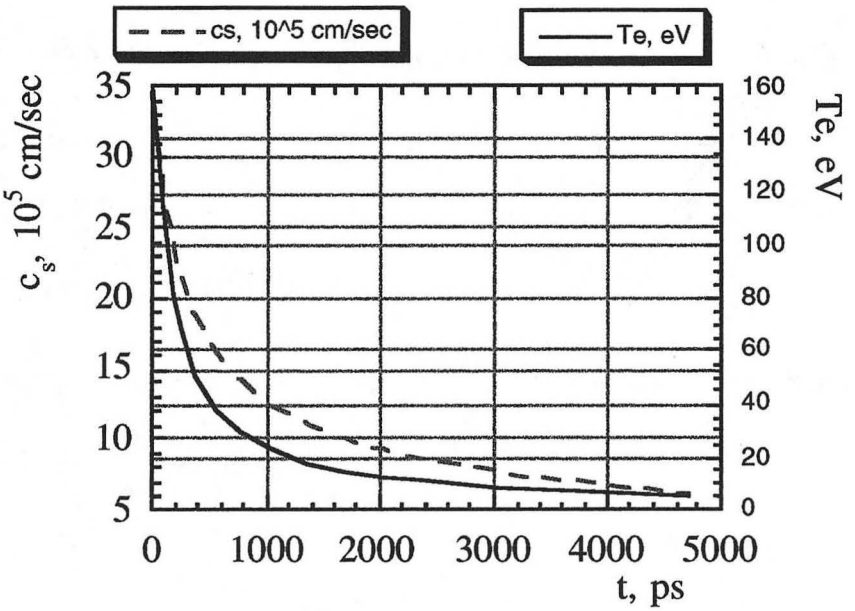

Figure 5-14

Shock front speed vs. time delay of the interferometer probe pulse, from the least squares fit to data in Figure 5-7, solid line. Temperature calculated from Eq. (5.3), dashed line. Nitrogen backed Gas Jet at 1000 psi backing pressure, Ignitor pulse energy 40 mJ, Heater pulse energy 280 mJ.

5.2.2 Strong explosion in a homogeneous atmosphere

The self similar problem of a strong explosion was formulated and solved by Sedov [53]. Sedov succeded in finding an exact analytic solution to the equations of self-similar motion. Next the problem is stated for the case of cylindrical geometry and a

solution is presented.

If a large amount of energy per unit length, E, is liberated in a cylindrical volume of small cross-section in a gas with constant specific heats and density ρ_0, a shock wave will propagate through the gas, starting from the point where the energy was released. The argument of self-similarity is valid in the region where the radius of the shock is large compared to the size of the initial explosion but not so large that the shock pressure is still much higher [54] than the pressure in the background gas. If these conditions are satisfied then the shock evolution depends only on the deposited energy per unit length, E, and the background gas density ρ_0. These two parameters cannot be combined to yield a quantity with dimensions of either length or time. Hence, the shock motion is self-similar, that is, it is a function of a particular combination of the coordinate r and the time t. The only dimensional combination of the two parameters which contains only length and time is the ratio of E to ρ_0 with dimensions $[E/\rho_0]=[cm^4s^{-2}]$. The dimensionless quantity

$$\xi = r\left(\frac{\rho_0}{Et^2}\right)^{1/4} \tag{5.5}$$

can serve as the similarity variable.

The shock front radius $R(t)$ evolution is given by a value of the independent dimensionless variable ξ_0

$$R(t) = \xi_0\sqrt{t}\left(\frac{E}{\rho_0}\right)^{1/4}. \tag{5.6}$$

The variable ξ_0 is typically on the order of 1 [61].

Least Squares Fits of the form of Eq. (5.6) to the data of Figure 5-11 and Figure 5-12 allow to calculate the energy per unit length deposited into the spark. For hydrogen it is 0.036 mJ/cm. In nitrogen, because of its higher degree of ionization, <Z>, the energy deposited per unit length with inverse Bremsstrahlung is expected to be higher than in hydrogen. Calculated from formula of Eq. (5.6), it is 1.21 mJ/cm.

The difference between the deposited energy calculated from the self-similar solution and the ion acoustic speed calculations (Section 5.2.1) is on the order of 25-30% for both hydrogen and nitrogen. It could be attributed to several factors, including the non-cylindrically symmetric shape of the shock and ξ_0 being different from 1.

5.3 Guiding Experiments

This Section describes the results of experiments on guiding high intensity laser pulses into the plasma channel. The laser pulse (injection pulse) was focused near the entrance of the channel using an off-axis parabola. The time delay between the Ignitor pulse and the injection pulse was fixed to 600 ps. (This constraint arose from physical limitations in the available vacuum chamber.) To diagnose the guiding, the laser beam was imaged onto a CCD camera with a MgF_2 lens of 1 inch diameter and focal length of fl=68.3 mm at 800 nm. The CCD camera was mounted on an optical rail so that it could be moved over about 50 cm range, thus changing the position of the imaging plane. The resolution and

magnification of the imaging system was calibrated for different CCD camera locations. To determine the exact position of the injected laser pulse focus in vacuum (without guiding), 90° scattered injection laser radiation from the pulse was used. By placing the channel so that its entrance approximately coincided with the injected laser focus position, and imaging the plane at the exit of the channel, a clear difference was observed between channel guided and vacuum diffracted laser spotsizes.

Section 5.3.1 gives a summary of the injection setup and imaging system calibration. The laser vacuum focus position measurement with respect to the gas jet is described in Section 5.3.2. Images of guided pulses are presented and analyzed in Section 5.3.3. An explanation of the transmission efficiency measurements is given in Section 5.3.4.

5.3.1 Injection Experiment Setup

An off-axis parabolic mirror, SORL, part no. 03-015-01Q, 25 mm clear aperture, apparent focal length fl=85 mm, deflection angle 41.8°, was used to bring the 20 mJ, 75 fs laser pulse to a focus for injection into plasma channels. The off-axis parabola was used to avoid nonlinear self-focusing and filamentation processes, ultrashort pulses are known to undergo in lenses, that affect the focusing of the laser pulse in a detrimental fashion. A schematic of the injection setup is shown in Figure 5-15. Due to the space limitations of the experimental chamber, the time delay between the Ignitor pulse and the injection pulse was fixed to 600 ps.

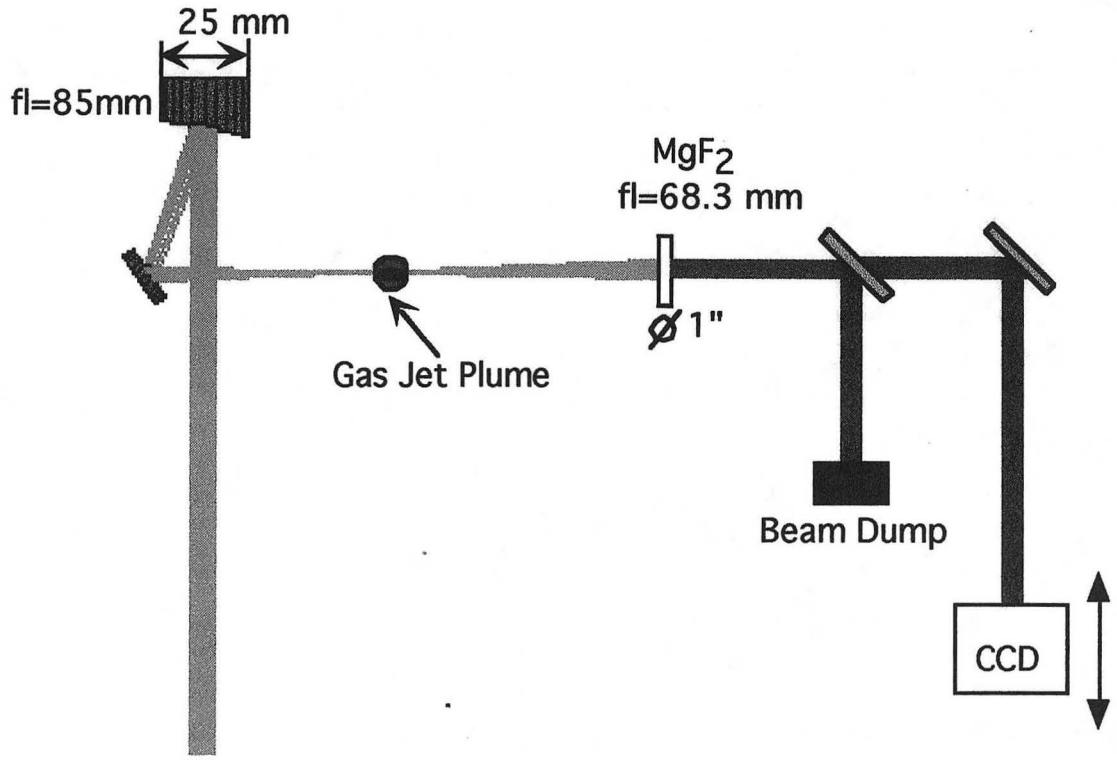

Figure 5-15

Injection setup and guided beam imaging schematic.

5.3.1.1 Laser Focus Position Measurement.

In order to optimize the laser pulse injection into the plasma channel, the position of the injection laser focus position was measured with respect to the gas jet using 90° Thomson side scatter measurement. A CCD camera with a fl=20 mm camera lens was used to image the spark at 90° to the direction of the injection laser pulse propagation. Two band pass filters centered around 850 nm, Corion P70-850-F and S40-850-F (resulting in a window of transparency of ~30 nm around 850 nm), were used to allow only the scattered laser radiation to be registered on the CCD camera.

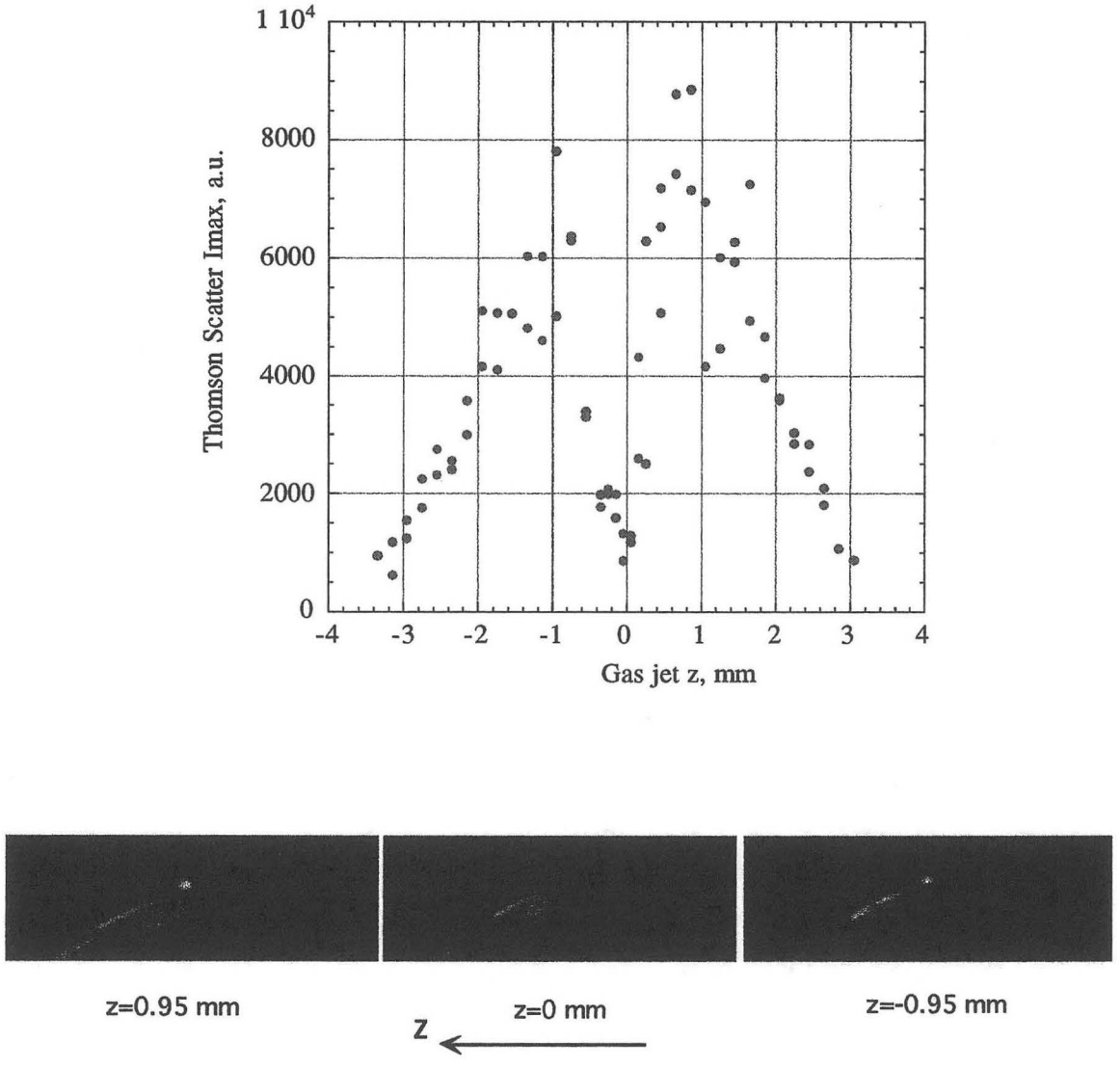

Figure 5-16

90° scattering peak amplitude at different gas jet positions. Laser Focus is at the center of the Gas Jet plume when z=0.0 mm. Positive z axis is in the direction of injection laser beam propagation.

At the edges of the gas jet plume, where the gas flow is turbulent, the Thomson scattering [55] amplitude is expected to be higher than when the laser is focused in the center of the

plume. The peak amplitude of the 90° scattering images at different Gas Jet positions is plotted in graph of Figure 5-16, together with three images of the scattered radiation. The sharp minimum of the scattering amplitude corresponds to the laser beam being focused at the center of the Gas Jet plume. The gas jet position with the injection laser focused at the very middle of the plume (the minimum amplitude of the scattering position) is referred in the remainder of this chapter as position z=0.0 mm.

5.3.1.2 Imaging System Calibration

To image an object plane in the vicinity of the gas jet plume, an F=3 MgF_2 lens (1 inch diameter, focal length of fl=68.3 mm at 800 nm) is combined with a CCD camera, (11 by 11 microns individual pixel dimensions, 640 by 480 pixels in a chip). The CCD camera was mounted on an optical rail so that it could be moved over about 50 cm range, thus changing the position of the object plane. To calibrate the imaging system, a 0.1 mm thick edge was attached to the center of the gas jet (directly below the orifice). The edge was imaged by optimizing the position of the CCD camera on the rail for different gas jet z-positions. The results of the measurement are plotted in the graph of Figure 5-17. This crosscalibrates the relative position of the object plane with respect to the Mg F_2 lens with the position of the CCD camera on the rail. Magnification can be calculated from knowing the focal length of the imaging lens and finding the image and object distances from the lens law Least Squares Fit to the data. Knowing magnification and the chip pixel size, the image scaling factor is calculated.

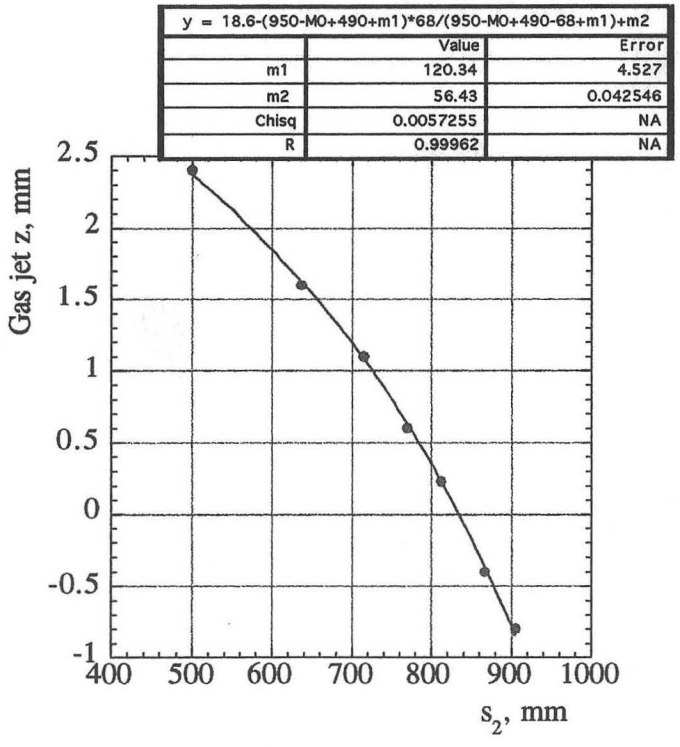

Figure 5-17

Imaging system calibration with a thin edge attached to the nozzle of the gas jet. Gas jet z-position vs. camera position on the rail, s_2, chosen for best imaging.

The evolution of the laser spotsize was measured as function of the CCD camera position on the rail (using the calibration of Figure 5-17 to relate it to the object distance). The graph in Figure 5-18 contains the results of the vacuum spotsize scan. There is slight astigmatism to the way the injection beam is going through focus: vertically, the smallest size is achieved at a slightly different position than horizontally. The position of the waist in the vertical scan is taken to be z=0 for the CCD imaging calibration.

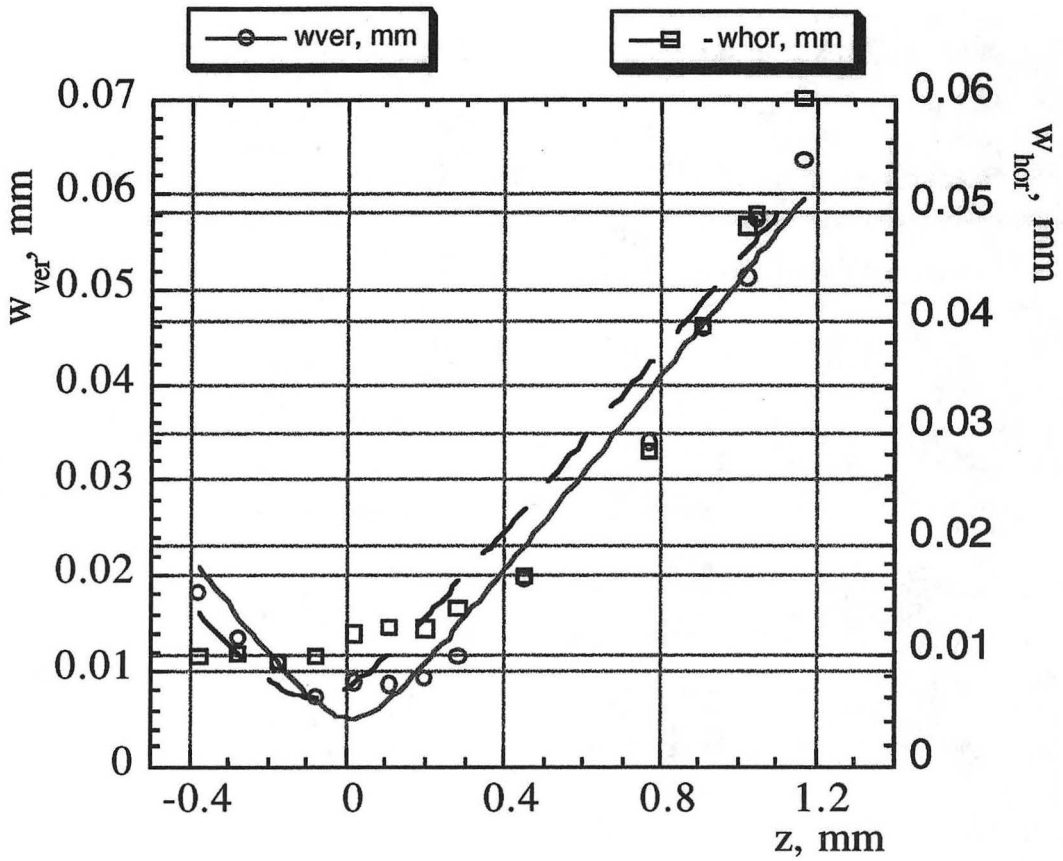

Figure 5-18

Vacuum spotsize scan. Vertical beam size, w_{ver}, - circles, and horizontal, w_{hor}, - squares, vs. the object plane z-position. Z=0.0 mm at the waist of the vertical spotsize.

5.3.2 Guiding.

5.3.2.1 Guided Beam Imaging

By comparing the laser beam images with and without the gas flowing out of the gas jet (valve pulsing or not), it was possible to clearly observe the effect of guiding on the laser beam.

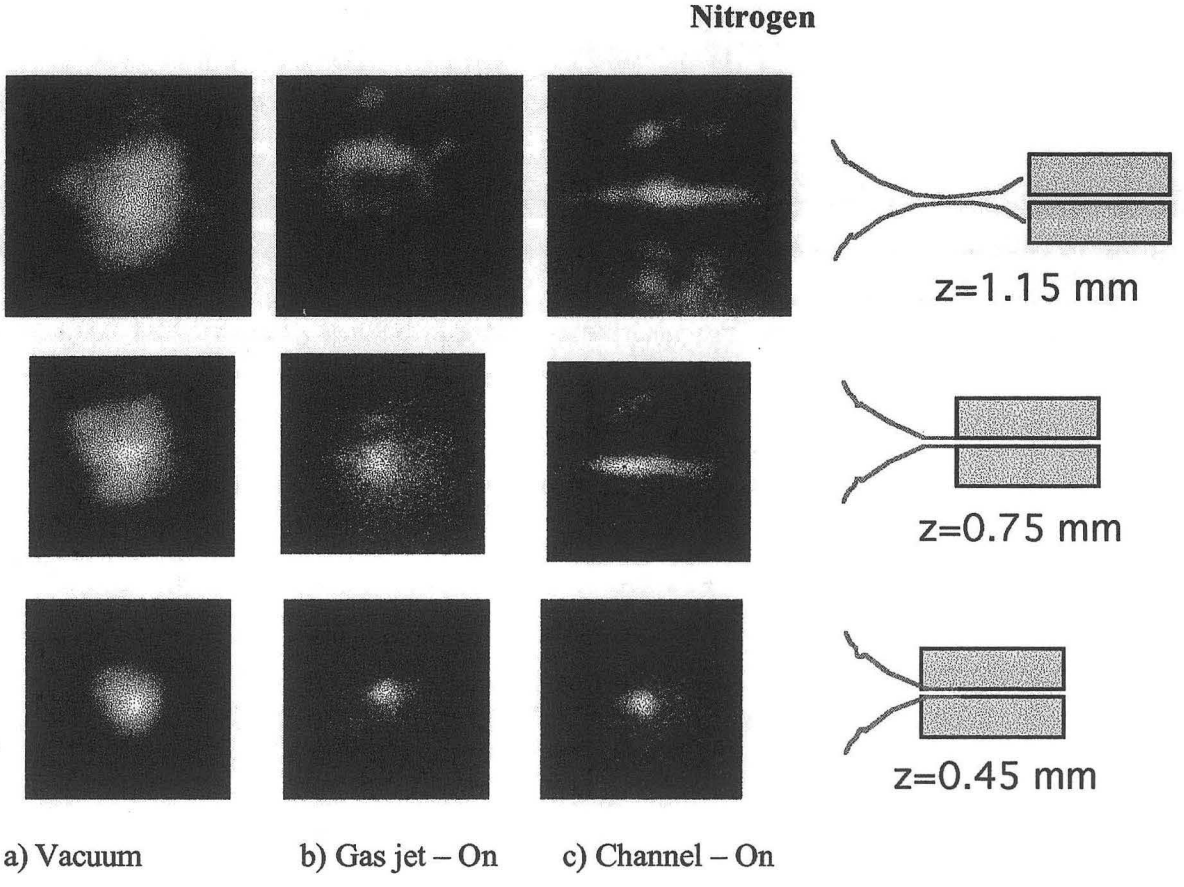

Figure 5-19

Injected laser beam images a) with the gas jet not pulsing, "vacuum", b) with the Gas Jet pulsing, but channel not being heated, "Gas jet - On", and c) with the gas jet pulsing and channel being created, "Channel - On" at different gas jet z-positions. The backing pressure of the gas jet was 1000 psi of nitrogen. Injection pulse energy ~20mJ, duration ~75 fs.

Figure 5-19 and Figure 5-21 show images of the injection laser pulse a) propagating through vacuum (gas jet turned off), b) after undergoing ionization induced refraction in the gas jet plume without the Heater pulse being present, hence no channel formed, and c) guided by the channel, for a gas jet backed with nitrogen and hydrogen at 1000 psi gas respectively.

Vertical lineouts of images of Figure 5-19, z=1.15 mm, clearly demonstrate the changes induced by the plasma channel on the guided laser pulse, Figure 5-20. The change

in size of ~8 times is consistent with a laser beam of Z_R~0.1 mm propagating a distance of 0.8 mm (the width of the jet).

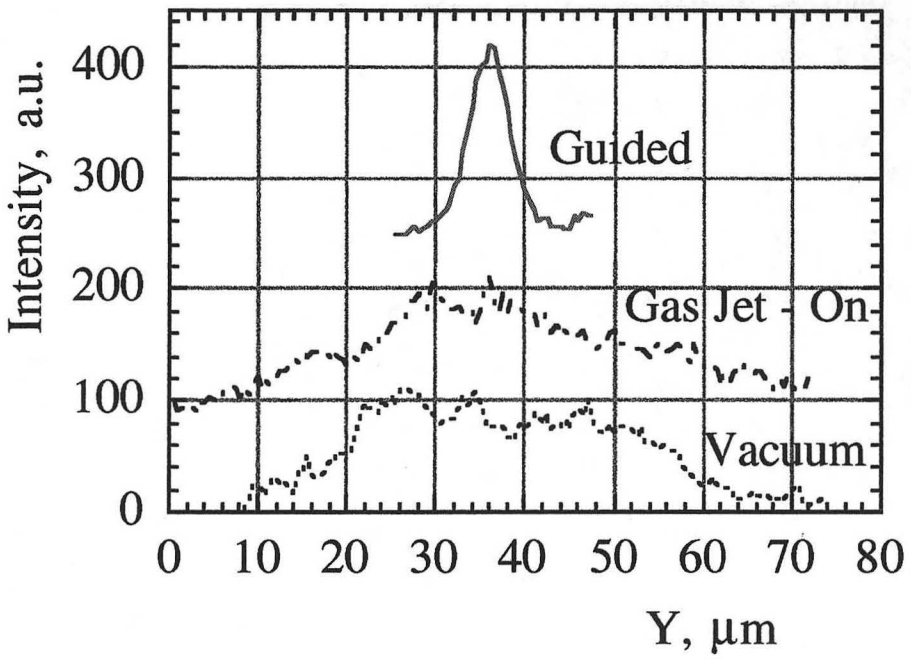

Figure 5-20

Vertical lineouts of images in Figure 5-19 demonstrate the change induced in the laser pulse by the plasma channel.

Figure 5-19 through Figure 5-21 demonstrate the clear change induced by the presence of a plasma channel on the laser spotsize. The plasma channel in hydrogen is not expected to have developed the depth and width sufficient for effective guiding at the fixed time delay of 600 ps after the Heater pulse of these experiments. Future experiments will test the guiding properties of hydrogen channels with larger time delays between injected pulse and the heater pulse. The remainder of this Chapter will be concerned with guiding

experiments in nitrogen.

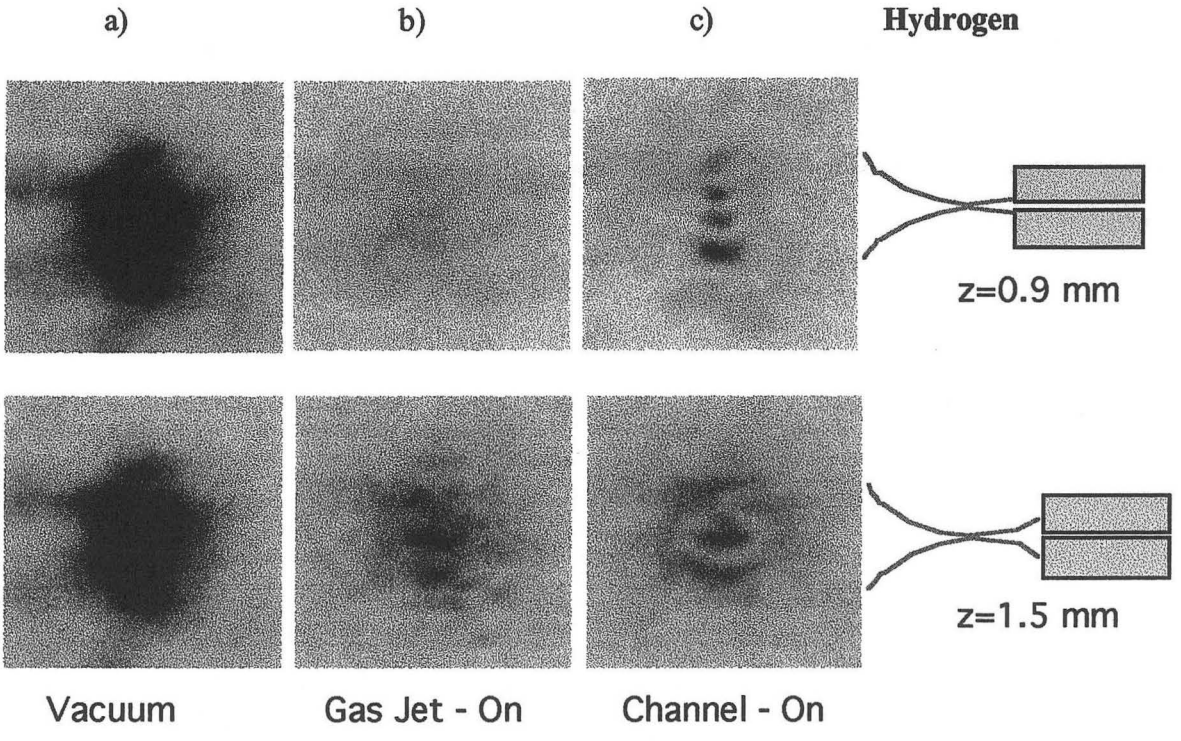

Figure 5-21

Injected laser beam images a) with the Gas Jet not pulsing, "vacuum", b) with the Gas Jet pulsing, but channel not being heated, "Gas jet - On", and c) with the gas jet pulsing and channel being created, "Channel - On" at different gas jet z-positions. The backing pressure of the gas jet was 1000 psi of hydrogen. Injection pulse energy ~20mJ, duration ~75 fs.

5.3.2.2 Guided Beam Size Evolution

In this section, a study of the guided beam image vs. the CCD camera position is used to find the guiding length and to prove that, as the gas jet is displaced, the guided beam waist is shifted accordingly.

The guided laser beam size was measured vs. z by moving the CCD camera,

similarly to the scan in Figure 5-18. Measurements were performed at two different gas jet z-positions, z=0.59 mm and z=1.02 mm, shown in Figure 5-22 and Figure 5-23 respectively. The positions of the vertical waist (smallest vertical spotsizes) in the two cases are ~0.9 mm and 1.25 mm respectively. The change in the waist position is in agreement with the measured gas jet size of FWHM~0.8 mm.

A set of data was taken for several different gas jet z-positions. The CCD camera was set at the point of smallest vertical spotsize for each gas jet z-position. The corresponding object plane locations were then plotted vs. the gas jet z-positions. The resultant graph is shown in Figure 5-24.

This clearly shows that moving the gas jet moves the beam waist.

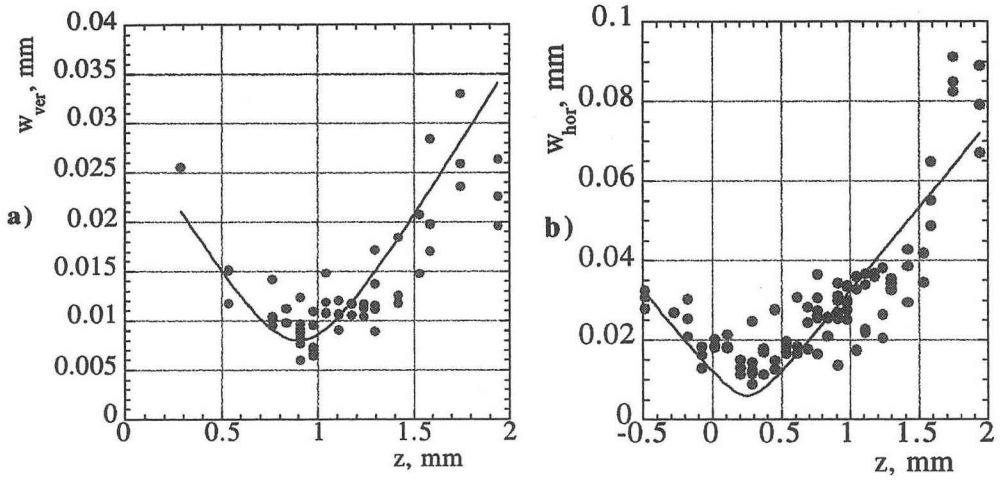

Figure 5-22

Guided beam size scan. 1000 psi of nitrogen, gas jet z=0.59 mm. Vertical guided lobe radius, a) and horizontal, b), vs. z.

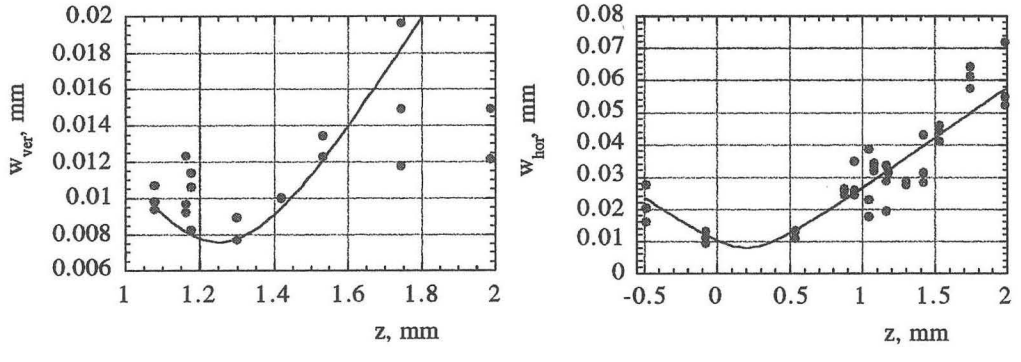

Figure 5-23

Guided beam size scan. 1000 psi of nitrogen, Gas Jet z=1.02 mm. Vertical guided lobe radius - filled circles, and horizontal - hollow squares, vs. object plane z.

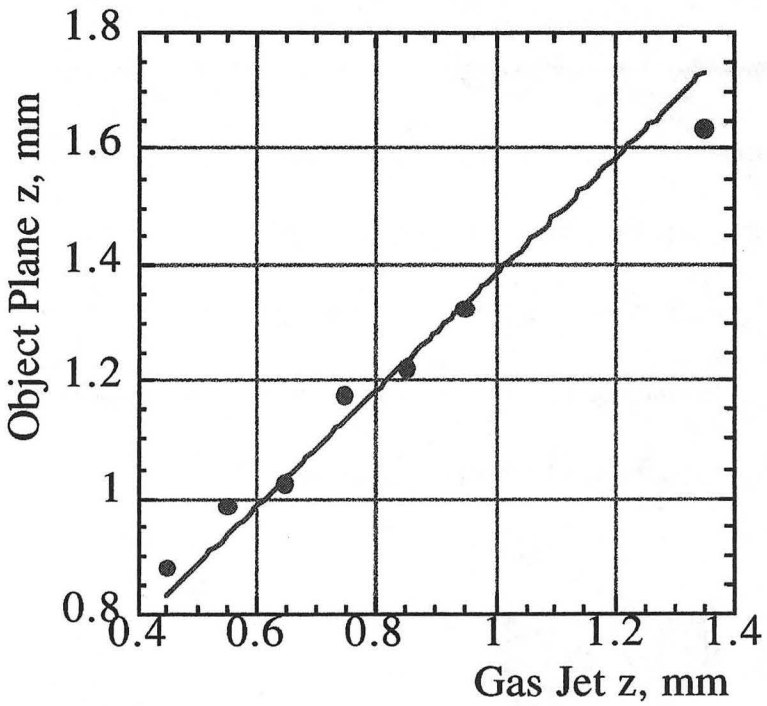

Figure 5-24

Changes in best camera position for imaging the guided lobe (vertical spotsize at minimum) vs. Gas Jet position. The line in the plot is drawn at 45° to the axes.

5.3.3 Controlling the Channel Shape.

As seen in Section 5.1.3, for the specific Ignitor and Heater pulse parameters, plasma channels were created in an elongated, elliptical shape. In turn, the guided beam

images (Figure 5-19) had a similar elongated shape. We next demonstrate that through control of the Ignitor pulse intensity, channels with circular cross-sections, possessing guiding properties in X as well as in Y direction, can be created. Since the initial volume of plasma is determined by the volume over which the intensity of the Ignitor pulse exceeds the ionization threshold intensity, the Ignitor pulse intensity can serve as means of control over the channel shape. By decreasing the Ignitor pulse intensity (via detuning the compressor, i.e. lengthening the pulse), plasmas were produced over smaller extent in x-direction, Figure 5-25, and hence, the energy deposition by the Heater pulse was localized to a much smaller area, leading to an aspect ratio of the resultant channel that was much closer to 1.

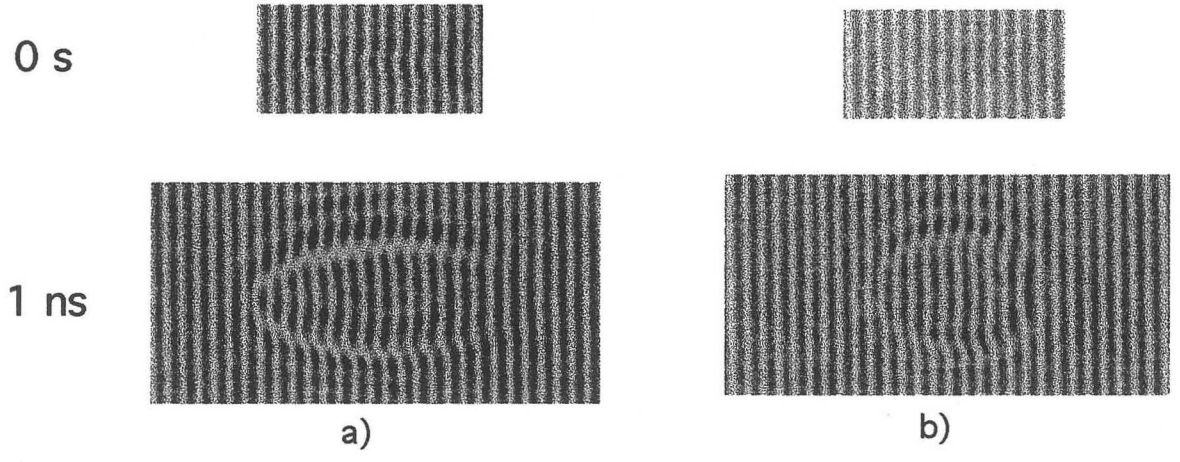

Figure 5-25

Change in channel crossection aspect ratio brought about by the reducing the Ignitor laser pulse intensity. a) best compression, b) detuned.

Laser pulses guided in such channels developed similar round shape. In Figure 5-26 the guided beam images are shown next to the corresponding channel shadowgrams. A shadowgram is an interferometer image taken with only the probe arm incident on the CCD camera chip. A shadowgram is an image of the refractive changes in the probe pulse

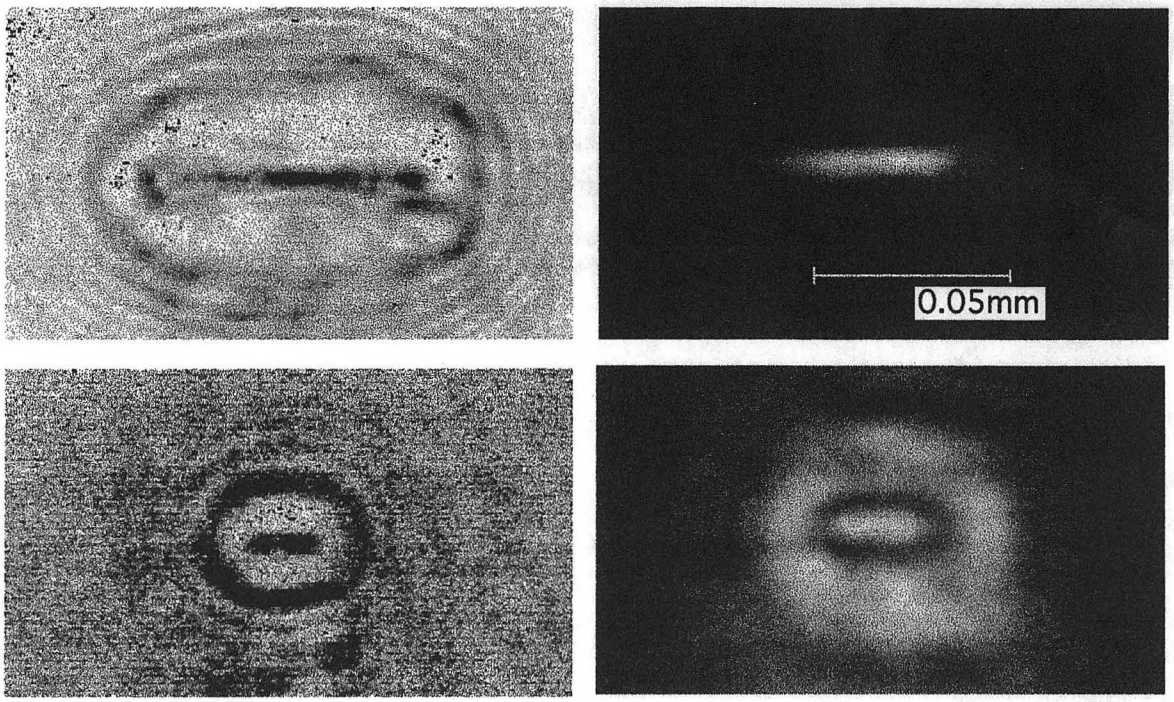

Figure 5-26

Guided beam images next to the corresponding channel shadowgrams. Aspect ratio of the guided beams is improved by a factor of 2.

as it traverses the plasma channel. The shock front is very distinctly shown in the shadowgrams because of the high gradients of the refractive coefficient at the shock. Shadowgrams were used in the experiments to visualize and optimize the channel production. The maximum of intensity on axis of a channel shadowgram is interpreted as an indication that the interferometric probe pulse is being partly guided by the channel. The difference in the guided pulse aspect ratio is clearly related to the shape of the channel. Thus, due to the ability to control the Heater and Ignitor laser pulses independently, it was possible to create a plasma channel with circular cross-section with

similar guiding properties in both X and Y directions. Horizontal intensity profiles of the images guided by differently shaped channels are plotted in the graph of Figure 5-27. There is a 2 times reduction in the horizontal guided beam size when the channel is created with a less intense Ignitor pulse, than when the fully compressed pulse is used for ignition. The side lobes in the case of a round channel indicate mode mismatch, which needs to be addressed in future investigations.

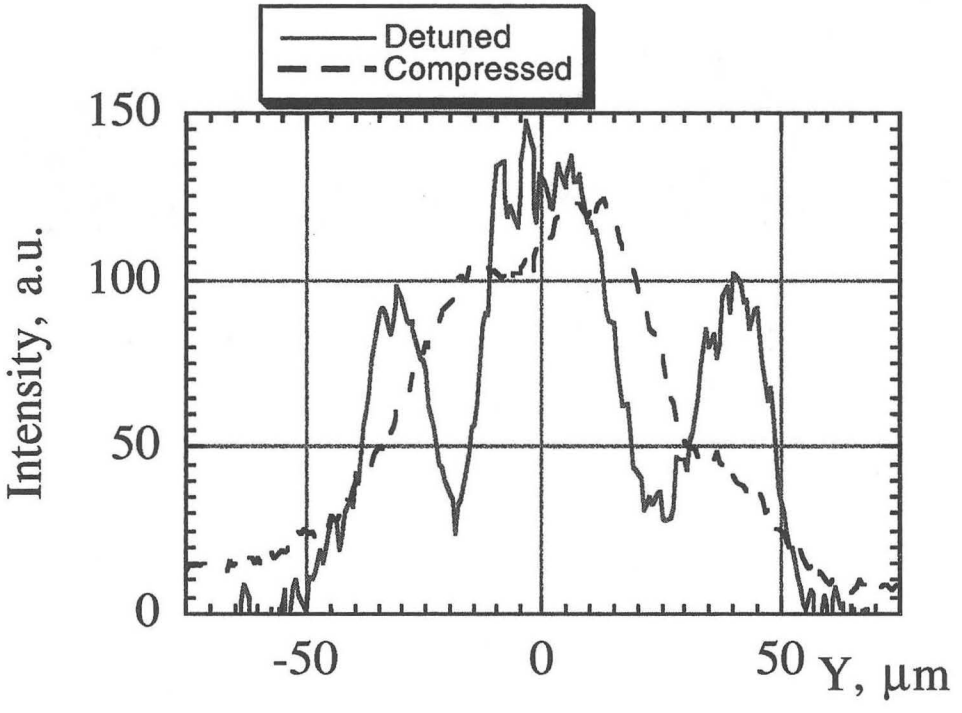

Figure 5-27

Horizontal intensity profiles of the images of laser pulses guided by a channel created with the Ignitor pulse at the optimal compression – solid, and detuned off the optimal – dashed

5.3.4 Mode Coupling and Propagation in Realistic Plasma Channels

In this section a rough estimate of the losses of the laser beam as it couples to and propagates through a realistic plasma channel is made. The results of this Section are compared to the experiments in the following Section.

As discussed in Section 2.2, a plasma channel with a parabolic density profile with infinite radial extent, $\Delta n_p = \Delta n r^2 / r_0^2$, supports a Gaussian guided mode $a^2 \propto \exp(-2r^2/r_0^2)$, provided that the channel depth satisfies $\Delta n = \Delta n_c$, where $\Delta n_c = (\pi r_e r_0^2)^{-1}$. If the injection is done with a perfectly Gaussian laser beam focused to a waist size of r_0 at the channels entrance then 100% of the injection laser energy will couple into the guided mode. If a perfectly Gaussian laser beam is not at its waist at the channel entrance, or if the waist size is different from the guided mode size for that particular channel, a corresponding fraction of the laser energy will couple to higher order modes in the channel. This loss mechanism we will refer to as the coupling loss.

Another loss mechanism in a realistic channel results from the laser tunneling through the channel walls. Experimentally created channels do not have infinitely high walls. Rather, as the profiles in Figure 5-10, the channel walls will reach a peak height and then fall off rapidly as shown in Figure 5-28. In our experiments, Section 5.2, the channel depth, width, and wall thickness at 600 ps after ignition were $\Delta n_{ch} \approx 1.5 \times 10^{18}\, cm^{-3}$,

$n_b \approx 7 \times 10^{18}\, cm^{-3}$, $x_{ch} \approx 8\,\mu m$, and $\Delta x \approx 3\,\mu m$ respectively. In such a channel there are no bound modes. The laser can leak out through the finite thickness walls, coupling to the continuum outside the channel. The degree of this leakiness depends on the channel depth, Δn_{ch}, width, $2x_{ch}$, and the wall thickness, Δx. The leakage loss is much larger for higher order modes, and any power not coupled into the fundamental mode of the channel is rapidly lost. Because of the finite transverse extent of the channel, peripheral parts of the laser pulse may miss the plasma all-together, spilling outside the channel, the spillage.

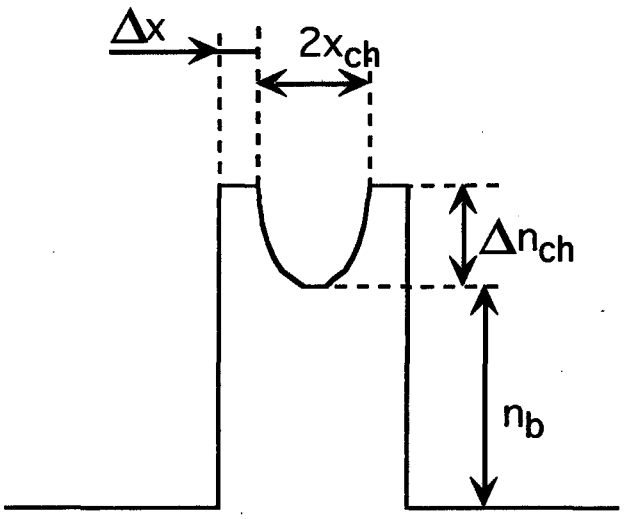

Figure 5-28

Schematic of a realistic plasma channel profile.

We have identified three different mechanisms of loss: coupling loss, leakage or tunneling loss, and spillage. This section presents calculations of all three types of loss and makes a comparison to the experimental data. Since in the experiments of this thesis the channels typically had guiding properties in one transverse direction only (Figure 5-9), a 1-D theory is used to describe the channel properties.

5.3.5 Loss from Leakage into Continuum.

To quantitatively estimate the contributions of these two loss mechanisms, the channel mode is assumed to be close to the fundamental mode of the infinite wall channel. Next, the equation describing the eigen modes in 1-D channel geometry is derived. The coupling efficiency and leakage rate are then estimated as functions of the input beam waist size and position, channel depth, width, and wall thickness.

Keeping the transverse derivative in the right hand side of Eq. (2.5) and (assuming that the laser pulse evolves slowly on the laser frequency time scale) using an eikonal approximation: $\frac{\partial^2}{\partial z^2} \approx -k_z^2 + 2ik_z \frac{\partial}{\partial z}$, where $a_0 = a(z,r)e^{i(k_z z - \omega t)}$, the paraxial wave equation is obtained:

$$\left(\frac{\omega^2}{c^2} - k_z^2 + \nabla_\perp^2 + 2ik_z \frac{\partial}{\partial z}\right) a = k_p^2 a \tag{5.7}$$

The lowest order mode (solution to Eq. (5.7) with the fourth term on the left hand side taken to be zero) in an infinite wall channel, $\Delta n = \Delta n_{ch} x^2 / x_{ch}^2$, is a gaussian $a^2 \propto e^{-2x^2/x_0^2}$ with

$$x_0 = \sqrt{\frac{2x_{ch}}{\Delta k_p}}, \tag{5.8}$$

where $\Delta k_p^2 = \frac{4\pi e^2 \Delta n_{ch}}{mc^2}$. The dispersion relation for this fundamental mode is found from Eq. (5.7) to be

$$\frac{\omega^2}{c^2} - k_z^2 = k_b^2 + \frac{\Delta k_p}{x_{ch}}, \tag{5.9}$$

where $k_b^2 = \frac{4\pi e^2 n_b}{mc^2}$. Hence, the k-number inside the channel wall is

$$k_w^2 = \frac{\omega^2}{c^2} - k_z^2 - k_b^2 - \Delta k_p^2 = \frac{\Delta k_p}{x_{ch}} - \Delta k_p^2. \tag{5.10}$$

For the channel depth, Δk_p, to be sufficient for guiding it is necessary that the laser pulse be evanescent in the channel walls (i.e. $k_w^2<0$). In two dimensions (from Section 2.2) this condition is $\Delta n > \Delta n_c = \left(\pi r r_0^2\right)^{-1}$ or, expressed differently,

$$\Delta k = \sqrt{\frac{4\pi e^2 \Delta n}{mc^2}} > \frac{2}{r_0} \tag{5.11}$$

changes in the 1-D case to

$$\Delta k_p > \frac{1}{x_{ch}}, \tag{5.12}$$

as derived from Eq. (5.10). Thus, for the same transverse channel dimension, the density depression required for 1-D guiding in a slab channel is four times smaller than that for 2-D guiding in a cylindrical channel.

The radiation that leaks through the wall continues to propagate as a plane wave at an angle, α, to the channel axis. This angle is determined from the boundary condition requirement, that z-components of the k-vectors inside and outside the channel be equal. The angle α can be alculated from the dispersion relation Eq. (5.9) and is given by

$$\sin\alpha = \frac{\sqrt{k_b^2 + \Delta k_p / x_{ch}}}{\omega / c}. \tag{5.13}$$

The rate of leakage can now be estimated with a Poynting vector argument:

$$\frac{1}{P}\frac{dP}{dt} \approx -\frac{cE_{out}^2 \sin\alpha}{\sqrt{\pi/2}\, x_0 E_0^2}, \tag{5.14}$$

Where P is the guided laser power, E_0 is the electric field amplitude on the channel axis, and E_{out} is the amplitude of the electric field tunneled through the channel wall

$$E_{out} \approx E_0 e^{-x_{ch}^2/x_0^2 - |k_w|\Delta x}. \tag{5.15}$$

In the experiments of Section 5.1.3, the channel depth, width, and wall thickness, at 600ps after ignition, were $\Delta n_{ch} \approx 1.5\times10^{18}\, cm^{-3}$, $n_b \approx 7\times10^{18}\, cm^{-3}$, $x_{ch} \approx 8\,\mu m$, and $\Delta x \approx 3\,\mu m$. These parameters give a guided mode radius of $x_0 \approx 8.33\,\mu m$, the k-number inside the channel's wall of $k_w = i1.56\times10^5\, m^{-1}$, the angle of leakage of $\sin\alpha = 0.0675$, and tunneled to on-axis field ratio of $\frac{E_{out}}{E_0} \approx 0.25$. By calculating the leakage exponent of Eq. (5.14) an estimate for the energy loss from the guided mode through tunneling is estimated to be ~ 35%.

5.3.6 Losses to Higher Order Modes and Refraction

A Gaussian laser beam, not properly mode matched at the entrance of a plasma channel, will not deliver all of its energy into the lowest order guided mode of the channel. Part of the energy will couple to higher order modes of the channel, while the rest will miss the plasma and propagate outside the spark. Next, a calculation of the coupling

efficiency to the fundamental Gaussian mode of the channel is presented.

In an infinite wall channel case a lowest order Gaussian beam $a \propto e^{-x^2\left(\frac{1}{w^2(z)}+\frac{i\omega/c}{2R(z)}\right)}$, where $w(z)=w_0\sqrt{1+\left(\frac{z}{z_R}\right)^2}$, $Z_R=\frac{\pi w_0^2}{\lambda}$, and $R(z)=z+\frac{z_R^2}{z}$, couples to the Gaussian guided mode with efficiency $C=\varepsilon^2$, where ε is given by

$$\varepsilon=\sqrt{\frac{2}{\pi w(z)x_0}}\int_{-\infty}^{+\infty}e^{-x^2\left(\frac{1}{w^2(z)}+\frac{i\omega/c}{2R(z)}\right)}e^{-x^2/x_0^2}dx= \frac{2}{\sqrt{x_0 w(z)}}\Bigg/\sqrt{\frac{1}{x_0^2}+\frac{1}{w^2(z)}+\sqrt{\left(\frac{1}{x_0^2}+\frac{1}{w^2(z)}\right)^2+\frac{\omega^2/c^2}{4R^2(z)}}} \tag{5.16}$$

When the laser waist is at the channel's entrance, Eq. (5.16) simplifies to

$$\varepsilon=\sqrt{2}\Bigg/\sqrt{\frac{x_0}{w_0}+\frac{w_0}{x_0}} \tag{5.17}$$

For the case of $x_0\approx 8.33\,\mu m$ and $w_0=2.4F\lambda\sim 5.76\,\mu m$, the efficiency is ~93%. In a finite radial extent plasma channel, a portion of the laser energy spills outside the channel. The steep plasma density gradient in the shock acts as a defocusing lens and the laser power incident on the shock is deflected and will not be collected by the MgF_2 lens. The portion of energy spilled, (the portion of the laser energy outside the spark), is given by

$$L_{spilled}=\sqrt{\frac{2}{\pi w^2(z)}}2\int_{x_{ch}+\Delta x}^{+\infty}e^{-2x^2\left(\frac{1}{w^2(z)}\right)}dx\ . \tag{5.18}$$

The portion of laser energy lost due to the refraction by the shock front is

$$L_{ref}=\sqrt{\frac{2}{\pi w^2(z)}}2\int_{x_{ch}}^{x_{ch}+\Delta x}e^{-2x^2\left(\frac{1}{w^2(z)}\right)}dx. \tag{5.19}$$

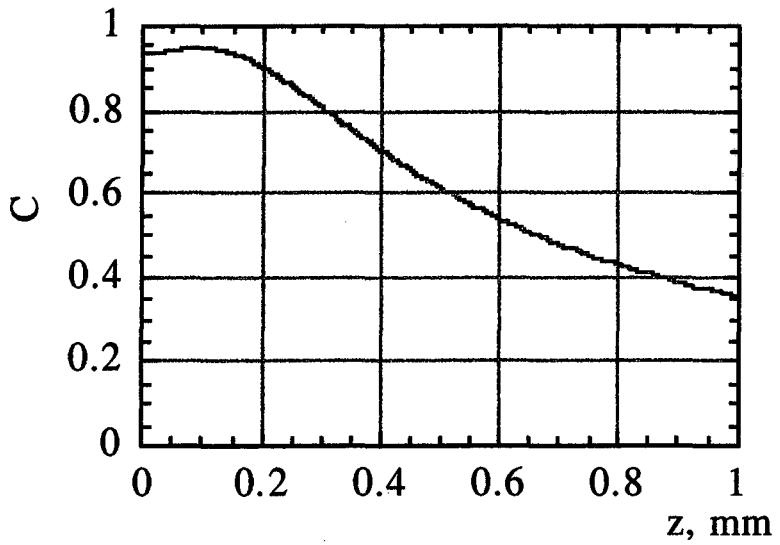

Figure 5-29

The coupling efficiency, C, calculated for the case of infinite wall channel, Eq. (5.16).

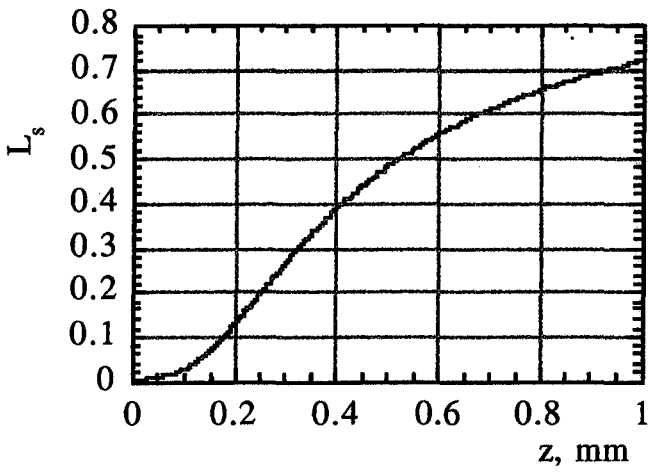

Figure 5-30

The combined fractional loss, Ls, due to the spillage outside the plasma, Eq. (5.18), and the shock refraction, Eq. (5.19), vs. the distance from the injection laser focus to the channel entrance.

For the case of $x_0 \approx 8.33\mu m$, $w_0 = 2.4F\lambda \sim 5.76\mu m$, and z=0, the combined fractional loss of Eq.(5.18) and Eq. (5.19) is $L_s = L_{spilled} + L_{ref} \sim 0.0055$.

These simple estimates are consistent with the experiment, as seen below.

5.3.7 Coupling and Transmission Efficiency Measurements

Presented in this section is a preliminary study of the energy losses in laser guiding. The discussion of this section will be used to direct future investigations.

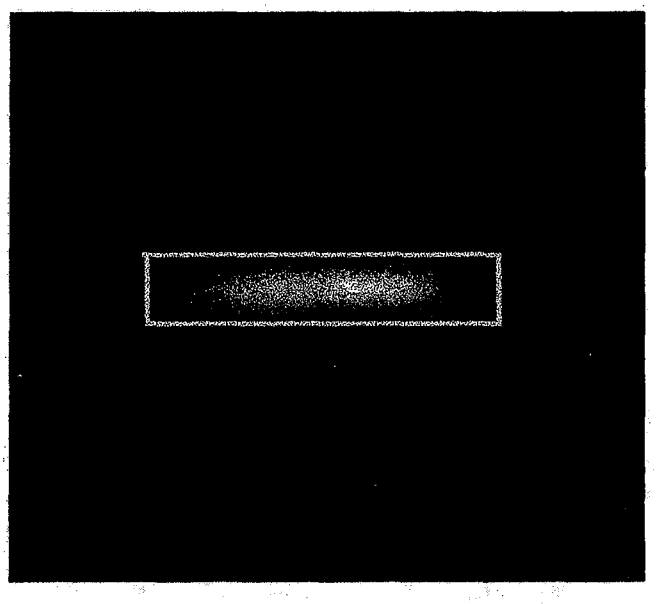

Figure 5-31

The energy is measured by integrating the pixel values over a selected image area. The area shown corresponds to the measurement of the guided energy.

The images in Figure 5-19 demonstrate that, as the gas jet is moved further away from the laser focus, the mode coupling into the channel worsens, i.e. larger portions of the injected laser energy are not coupled into the channel, but rather spilled outside the

channel. Quantitatively, the image intensity integral is a measure of the laser energy. By taking intensity integrals of the CCD images, we will compare the amount of the laser energy guided by the channel to the total intensity integral of the CCD image (full beam energy, E_{full}) and the image intensity integral of the vacuum propagated beam (E_{vacuum}). The intensity integral of the isolated central lobe of the images is taken to be the guided energy. An example of the image area chosen for the measurement of the guided energy is shown in Figure 5-31.

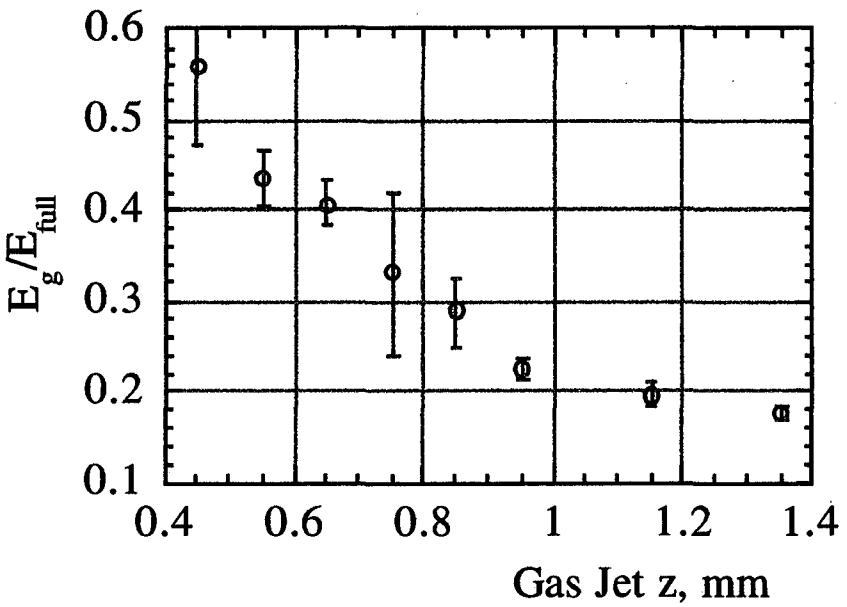

Figure 5-32

Ratio of energy in the central lobe or guided, E_g, to that of the full beam, E_{full}, plotted vs. the gas jet position.

The ratio of the guided energy, E_g, to the total image intensity integral, E_{full} is shown in

Figure 5-32. As expected, the fraction of the laser beam that is coupled into the channel is larger as the injection pulse focus is moved closer to the jet's edge than when the gas jet is moved further away from the laser focus position in vacuum. It should be noted that the F-numbers of the off-axis parabola and the imaging MgF_2 lens are rather close and the collection angle is limited. Nevertheless, the leakage of the fundamental mode of the plasma channel is fully collected.

As the laser waist is moved closer to the channel entrance, the laser spotsize becomes comparable with the channel size and most of the power is coupled to the modes of the channel. The ratio of E_g to the E_{full} approaches ~60 %. This number is in good agreement with the results of Section 5.3.5, where the leakage fraction was calculated to be ~35% (i.e. E_g/E_{full}~ 65%).

The fraction of the laser energy spilled outside the channel (E_{full}/E_{vacuum}) is plotted in the graph of Figure 5-33. Also shown is the theoretical prediction of Eq.(5.18). Agreement is fair.

The guided laser energy was measured to be at most ~0.2 of the injected beam energy (calculated from images of laser beams propagating in vacuum, i.e. with the gas jet off). This number is about a factor of 3 lower than the predictions of Section 5.3.6. There are several factors that could explain this discrepancy.

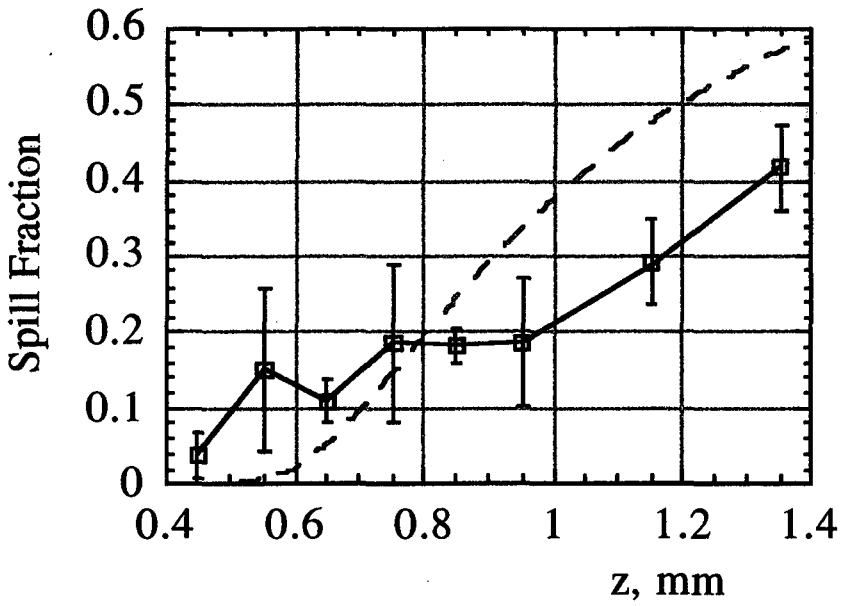

Figure 5-33

Energy fraction outside the guided lobe, or spillage, $(E_{full}-E_g)/E_{vacuum}$. Measured - squares, calculated – dashed line.

The injection laser beam is not a pure zero order Gaussian mode. The plasma channel, similarly to a spatial filter, selects only the lowest Gaussian mode. The injection laser beam is believed to be 70% Gaussian at best.

The plasma density of the gas jet is naturally smaller near the edges than in the center. The inverse Bremsstrahlung is less efficient in heating lower density plasma (Section 3.1.3). Therefore, the channel near the gas jet edge is not as deep, or wide as in the center of the jet. This "closed" end of the channel will act as a defocusing lens, which is likely to dramatically reduce the injection laser coupling efficiency. To experimentally verify whether this effect is indeed present, a transverse diagnostic, such as 90° Thomson scattering or transverse interferometry is needed.

From the temperature measurement of Section 5.2, T_e~120eV, the degree of ionization of nitrogen in these experiments is believed to be 5. The intensity needed to ionize the fifth electron (97.89 eV ionization potential) is ~$1.5 10^{16}$W/cm^2. To ionize the sixth electron (552 eV), the intensity of ~10^{19}W/cm^2 is required. Although it is possible that a fraction of nitrogen atoms were additionally ionized by the injection laser pulse and ionization refraction has reduced, somewhat, the amount of the laser power coupled into the channel, this is not believed to be a major factor, because the density depression in the channel, 1.5×10^{18} cm^{-3}, is on the order of the neutral gas density in the jet.

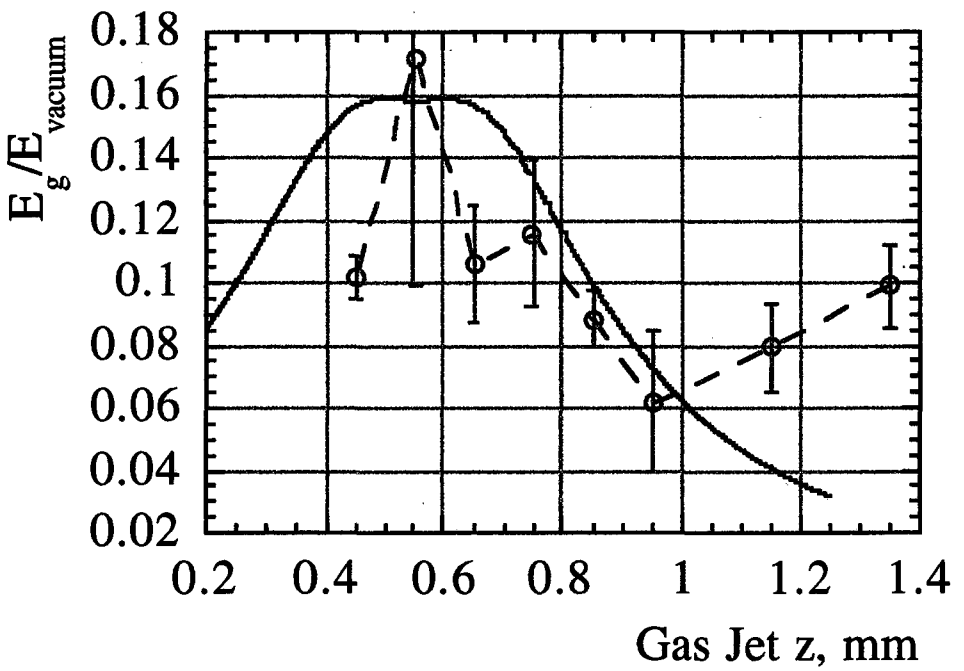

Figure 5-34

Ratio the guided laser beam energy, E_g, to the energy of the vacuum propagated beam (Gas Jet turned off), E_{vacuum}, vs. the gas jet position.

With that in mind, we compare the energy transmission efficiency predicted in

Section 5 with that measured by introducing an arbitrary scaling factor to match the peak transmission efficiency, Figure 5-34. The qualitative behavior of the experimental data matches the calculated for z<1mm. The transmission efficiency increases for z>1mm. This can be attributed to the fact that, at those gas jet positions, the spillage fraction is large (Figure 5-33), resulting in a substantial intensity propagating alongside the plasma channel. The tunneling through the channel walls from the outside of the channel into the guided mode would increase the measured guided energy.

5.4 Summary

Experiments, presented in this chapter have demonstrated the viability of the Ignitor-Heater plasma channel creation technique for high intensity laser guiding.

Plasma channels were formed, for the first time, in multiply ionized nitrogen and hydrogen without the need for high Z gas additives. A gas jet was used to avoid ionization induced refraction. Gas jet density profile was characterized as a function of the distance to the orifice and the transverse coordinate, using 2-D interferometry of the plasma created with the Ignitor pulse only. The plasma temperature was calculated from ion acoustic speed (shock front expansion speed) measurements, performed with femtosecond 2-D interferometry. These calculations were found to agree well with predictions from the inverse Bremsstrahlung theory (Chapter 3). The results of the temperature measurements were cross-checked by calculating the energy deposition from the Sedov's theory. The ionization degree of nitrogen was calculated from the inferred plasma temperature to be ~5. The laser intensity necessary for ionization of the 6 electron of nitrogen is ~10^{19} W/cm^2.

The vertical plasma density profiles of the channels had a density minimum on axis, while the horizontal profiles did not.

The guiding properties of plasma channels were tested by injecting an intense (5×10^{17} W/cm^2) short (75 fs) laser pulse at a fixed delay time of ~600 ps after the heating. By measuring the position of the laser beam waist in vacuum and with a plasma channel in nitrogen, it was proven that the laser was guided in the vertical direction over the full length of the jet, ~10 Z_R

Consistent with the plasma channel density profile measurements, the laser pulses were guided in the vertical direction only. The plasma channel shape was modified to have an aspect ratio closer to 1 by decreasing the Ignitor pulse intensity and thus reducing the horizontal extent of the initial spark. The laser pulses were shown to be guided in both transverse directions by such channels. Future experiments will concentrate on improving the 2-D guiding properties of the plasma channels.

Insertion loss in nitrogen plasma channels was studied both experimentally and theoretically. Guiding losses in realistic plasma channels can be caused by leakage, spillage, and coupling loss. Leakage or tunneling loss occurs because of the finite radial extent of the channel plasma. The guided mode can couple to the continuum outside the channel walls and, in that way, the laser energy can leak out of the channel. Spillage is also due to the finite radial extent of the plasma, it is the loss of the laser energy that falls outside the plasma walls at the entrance of the channel. The coupling loss occurs if the laser mode at the entrance of the channel does not exactly match the lowest order Gaussian mode of the channel. This causes a portion of the laser energy to couple to the higher order modes of the channel for which the leakage rate is much higher.

Insertion losses due to these mechanisms were measured as functions of the gas jet position with respect to the vacuum focus position of the injection laser pulse. Spillage and

leakage mechanisms were found to agree well with the theoretical predictions. The coupling loss was measured to be much higher than the calculated value. This difference is attributed to the fact that the injected laser beam has a large higher order mode content. Future experiments will concentrate on injecting a purer TEM_{00} laser mode.

Plasma channels produced in hydrogen were shown to affect the laser beam profile in a manner similar to the nitrogen channels. However, channels with plasma density variation sufficient for guiding were not expected to be formed in hydrogen at the time delay of 600 ps. Future experiments with larger time delays of the injected laser beam are expected to demonstrate improved guiding in hydrogen channels.

The next Chapter addresses the other two limitations on the acceleration length, i.e. laser pulse depletion and dephasing.

6 Driving Laser Pulse Evolution

In this Chapter we present an analytic and numerical study of the coupling between a high intensity laser pulse and the plasma wake in the context of LWFA in a homogeneous plasma and in a hollow channel. The presentation closely follows P. Volfbeyn et al., Phys. Plas. Vol.4, 3403 (1997).

As discussed in Chapter 2, the excitation of a large amplitude plasma wave (10 GV/m for a plasma wave with $\delta n / n_0 = 0.1$ at $n_0 = 10^{18} cm^{-3}$) requires laser intensities on the order of 10^{18} W/cm^2 (for a laser wavelength ~1 micron). At such high intensities the index of refraction of the plasma is modified by its interaction with the laser pulse. This modification occurs through relativistic effects as well as through laser ponderomotive force driven plasma density modulation arising from the excited plasma wave. The interaction with the plasma affects both the longitudinal and transverse properties of the laser pulse. These, in turn, lead to changes in the coupling of the laser pulse to the plasma and, thus, in properties of the accelerating plasma wave. Understanding these issues is important for evaluation and optimization of the efficiency of LWFA designs and in understanding experimental results. In this Chapter a one dimensional (1-D), nonrelativistic analytic model of the driving pulse evolution and supporting simulation results will be presented, with emphasis on the effects of energy depletion, longitudinal laser pulse shape distortion, and changes in the group velocity and center wavelength of the pulse.

In this Chapter a new diagnostic method that measures the laser energy coupling to the plasma wave based on the measurement of the changes of the driving laser pulse [9] is discussed. This diagnostic derives information about the excited plasma wave from the

phase (or frequency) evolution of the driving laser pulse. It is passive, in that it does not require additional laser pulses or an externally injected electron beam. The temporal resolution of the laser pulse phase is shown to provide information about the temporal profile of the plasma wave.

In Section 6.1 a one dimensional (1-D), nonrelativistic analytic model of the driving pulse evolution and supporting simulation results is presented, with emphasis on the effects of energy depletion, longitudinal laser pulse shape distortion, and changes in the group velocity and center wavelength of the pulse. Section 6.1.1 presents approximate scaling laws that describe the evolution of the driving laser pulse and discusses their consequences for acceleration. In Section 6.1.2, 1-D equations to model the evolution of a laser pulse in a plasma are derived and numerical solutions of these equations are presented.

In Section 6.2 the one dimensional nonrelativistic analytic model of the driving pulse evolution described in Section 6.1 is extended to study the hollow channel geometry. The use of energy conservation in this theoretical approach greatly simplifies the analysis.

6.1.1 Approximate Scaling Laws

With $\delta n / n_0$ in Eq. (2.15), Eq. (2.6) could now be analyzed. However, before doing so, it is instructive to obtain a qualitative picture of the evolution of the driving laser pulse as it excites a plasma wake. We first consider the simplified 1-D case of a laser pulse with a flat -top temporal profile propagating in a plasma with a density profile co-

moving with the laser pulse that changes linearly in ξ, i.e. $\omega_p^2 = \omega_{p0}^2 + \kappa\xi$. Here $\xi = z - ct$, and κ is the constant plasma density gradient. The term $\kappa\xi$ phenomenologically represents the plasma density change due to plasma waves excited by the laser pulse. A more sophisticated qualitative analysis of driving laser pulse evolution was presented by Bulanov *et al.* [56].

For $a_0 << 1$, the plasma modifies the phase and group velocities of the laser as

$$V_\phi = \frac{\omega}{k} = c \Big/ \sqrt{1 - \omega_p^2/\omega^2},\ V_g = \frac{\partial\omega}{\partial k} = c\sqrt{1 - \omega_p^2/\omega^2}, \tag{6.1}$$

where $k = \omega/c$ is the wavenumber of the laser.

When the plasma density varies with ξ and not z, different portions of the pulse continuously experience different plasma densities. As a result, the phase and group velocities are different for different portions of the laser pulse. This, in turn, leads to changes in frequency and duration of the laser pulse and, in self-consistent description, allows for energy balance. The leading edge of the laser pulse moves slower than the trailing edge by a factor

$$\Delta V = c\Delta\sqrt{1 - \omega_p^2/\omega^2} = c\frac{\kappa\tau}{2\omega^2}, \tag{6.2}$$

where τ is the laser pulse length. Thus

$$\frac{1}{c}\frac{d\tau}{dt} = -\frac{\Delta V}{c} = -\frac{\kappa\tau}{2\omega^2}. \tag{6.3}$$

Similarly, the change in distance between adjacent crests of the laser wave can be found from

$$\frac{d\lambda}{dz} = \frac{\lambda}{c}\frac{d}{d\xi}\left(c \Big/ \sqrt{1-\omega_p^2/\omega^2} \right) = \frac{\kappa\lambda}{2\omega^2}, \tag{6.4}$$

Note that, to the third order in (ω_p/ω) the product $\tau\lambda$ remains constant:

$$\frac{d(\tau\lambda)}{dz} = \tau\frac{\kappa\lambda}{2\omega^2} - \lambda\frac{\kappa\tau}{2\omega^2} = 0, \tag{6.5}$$

Equivalently, τ/ω=const. As it will be seen later in this Section, the laser created wave has a density gradient that decreases towards the end of the laser pulse. Hence, in the case of $\kappa > 0$, the linear plasma profile effects the laser pulse in a manner similar to that of a self-consistent wake.

Theoretically, the interaction between the driving laser and plasma can be viewed as a decay of electromagnetic laser wave into a plasma wave and a frequency shifted electromagnetic wave. Since the laser pulse duration τ is of the order of one half the plasma period, the spectral bandwidth of the laser pulse is larger than the plasma frequency. An electromagnetic wave shifted by ω_p will remain a part of the laser pulse, resulting only in a change in the frequency of the laser pulse. Because the scattered electromagnetic wave remains a part of the laser pulse, the number of photons in the laser pulse is conserved, the energy is lost by reduction in frequency and not by loss (conversion) of photons [57]. This action invariance in laser wakefield generation is a realization of the Manley-Rowe relationship. Since the number of photons is proportional to the energy of the laser pulse divided by the frequency: $N_{ph} \propto E^2\tau/\omega = const.$; combining this with the previous result, $\tau/\omega = const.$, we obtain $E = const.$.

To summarize, the laser pulse shortens and reddens as it propagates in a plasma with a density profile linearly decreasing towards the back of the laser pulse. Thus the laser pulse also loses energy, i.e. it depletes [58]. The reddening and shortening combined with an increase in a_0 conserve the number of photons in the laser pulse which, in the linear density profile case, is equivalent to electric field amplitude in the laser pulser, E, being constant.

Combining the Eqs. (6.3) and (6.5) we obtain

$$\frac{d\tau}{dz} = -\frac{\kappa\tau}{2\omega^2} = -\frac{\kappa}{2}\frac{\tau_i^2}{\omega_i^2}\frac{1}{\tau}, \tag{6.6}$$

where $\omega_i = \omega(z=0)$, and subscript i signifies the initial unperturbed quantity from now on. By solving Eq. (6.6) we find the z-dependence of the laser pulse duration τ,

$$\tau/\tau_i = \sqrt{1-\kappa z/\omega_i^2}\,; \tag{6.7}$$

or, equivalently,

$$\omega/\omega_i = \sqrt{1-\kappa z/\omega_i^2}\,. \tag{6.8}$$

To determine the effect of these changes in the drive pulse back on the wakefield, we combine the above results with the expression for the electric field amplitude of the wake in a hollow channel, obtained by substituting a flat-top laser profile into Eq. (2.15)

$$E_z = 2k_{pi}\frac{mc^2}{4e}|a_0|^2 \sin(\frac{k_{pi}\tau}{2})\cos[k_{pi}(\xi+\frac{\tau}{2})], \tag{6.9}$$

where $k_{pi} = \omega_{pi}/c$, with E=$a_0\omega$=const., and $a_0/a_{0i}=\omega_i/\omega=1/\sqrt{1-\kappa z/\omega_i^2}$. From Eq. (6.9) it is seen that, for fixed a_0 and k_p, there exists an optimal value the pulse length $\tau = \pi/k_{pi}$. A

reduction in coupling due to the pulse length decrease can be more than offset by the increase in a_0 as the pulse propagates through plasma (see Eq. (6.9)).

As the spectrum of the laser pulse reddens its group velocity decreases. An important parameter for a LWFA accelerating section is the dephasing length. A highly relativistic electron will move faster than the phase velocity of the plasma wake. Such electron may not be accelerated infinitely in a single LWFA stage because it will eventually traverse the accelerating region of the plasma wake and "slip" into the decelerating region. The distance over which an electron moving with a speed close to the speed of light slips over π radians of the wakefield phase is called the dephasing length. Using Eq. (6.1) for the laser pulse group velocity, and Eq. (6.8) for the frequency evolution, the dephasing length for the linear density variation, flat-top laser pulse case is

$$l_{deph} = l_{dpl}(1 - e^{-L_{deph}/l_{dpl}}), \tag{6.10}$$

where $l_{dpl} = \omega_i^2 / \kappa$ is the distance after which all of the laser energy is lost to the wake, the full depletion length, and $L_{deph} = \dfrac{2\pi\ \omega_i^2}{k_{ch}\ \omega_p^2}$.

As pointed out in the discussion following Eq. (6.9), a high accelerating gradient is maintained even after a substantial fraction of the laser energy is depleted. By increasing the laser amplitude while keeping the plasma density constant, so that the ratio of the dephasing length to the depletion length is increased, the portion of the laser energy deposited into the plasma wave can be increased.

In a realistic scenario, the plasma wake profile excited by the laser pulse is far

from linear, causing the character and speed of the dephasing process to change, and deviate from that described in Eq. (6.1), as will be shown in Section 6.1.2.

6.1.2 SELF-CONSISTENT EVOLUTION OF THE LASER PULSE

In this Section an eikonal theory of laser evolution based on the fluid model is presented. We define $a_0 = be^{-i\Phi}$, where b is real and a slow function of z and ξ, and Φ is also real and a slow function of z, and Φ has fast variations in ξ. The real part of Eq. (2.6) becomes

$$\frac{\partial^2 b}{\partial(kz)^2} - b\left(\frac{\partial \Phi}{\partial(kz)}\right)^2 + 2\frac{\partial^2 b}{\partial(kz)\partial(k\xi)} - 2b\frac{\partial \Phi}{\partial(kz)}\frac{\partial \Phi}{\partial(k\xi)} = \chi b, \tag{6.11}$$

and the imaginary part is

$$2\frac{\partial b}{\partial(kz)}\frac{\partial \Phi}{\partial(kz)} + b\frac{\partial^2 \Phi}{\partial(kz)^2} + 2\frac{\partial b}{\partial(kz)}\frac{\partial \Phi}{\partial(k\xi)} + 2\frac{\partial \Phi}{\partial(kz)}\frac{\partial b}{\partial(k\xi)} + 2b\frac{\partial^2 \Phi}{\partial(kz)\partial(k\xi)} = 0. \tag{6.12}$$

The equations were made dimensionless by dividing both parts of Eqs. (6.11) and (6.12) by the wave number of the laser, k^2. Also, the quantity $\chi = k_p^2 / k^2$ was introduced.

Since ω_p / ω <<1, as a small quantity, it is useful to rewrite Eqs. (6.11) and (6.12) to contain only the lowest order (in ω_p / ω) terms. In Eq. (6.11) the fourth term on the left hand side, and the right hand side are lowest order in ω_p / ω , as will be proven a posteriori. In Eq. (6.12) the third, fourth, and the fifth terms dominate.

Rewriting Eqs. (6.11) and (6.12) to the lowest order in $\frac{\omega_p}{\omega}$ we obtain

$$-\frac{\partial \Phi}{\partial(kz)}\frac{\partial \Phi}{\partial(k\xi)}=\frac{\chi}{2} \tag{6.13}$$

and

$$\frac{\partial}{\partial(kz)}\left(b\frac{\partial \Phi}{\partial(k\xi)}\right)=-\frac{\partial \Phi}{\partial(kz)}\frac{\partial b}{\partial(k\xi)}. \tag{6.14}$$

From Eqs. (6.13) and (6.14) and the definition of Φ and b,

$$\frac{\partial \Phi}{\partial(k\xi)}\propto 1, \tag{6.15a}$$

$$\frac{\partial \Phi}{\partial(kz)}\propto\frac{\omega_p^2}{\omega^2}, \tag{6.15b}$$

and

$$\frac{\partial b}{\partial(kz)}\propto\frac{\omega_p^3}{\omega^3}. \tag{6.15c}$$

It is readily seen that any ξ derivative except $\frac{\partial\Phi}{\partial\xi}$ adds at least one order in $\frac{\omega_p}{\omega}$: performing a ξ derivative is similar to dividing by the number of laser periods contained in the laser pulse. Indeed, the length of the laser pulse is of the order of $\frac{1}{k_p}$ for best coupling to the plasma wake, and the laser period is order $\frac{1}{k}$. Therefore,

$$\frac{\partial^2\Phi}{\partial(kz)\partial(k\xi)}\propto\frac{\omega_p^3}{\omega^3}, \tag{6.15d}$$

$$\frac{\partial^2 b}{\partial(kz)^2}\propto\frac{\omega_p^5}{\omega^5}, \tag{6.15e}$$

$$\frac{\partial^2 b}{\partial(kz)\partial(k\xi)} \propto \frac{\omega_p^4}{\omega^4}, \tag{6.15f}$$

$$\frac{\partial^2 \Phi}{\partial(kz)^2} \propto \frac{\omega_p^5}{\omega^5}. \tag{6.15g}$$

The results obtained in Section 6.1.1 for a flat-top pulse are recovered by taking the ξ derivative of both sides in Eq. (6.13), namely

$$\frac{\partial\,\omega}{\partial z} = -\frac{1}{2\omega}\frac{\partial\,k_p^2}{\partial \xi} \tag{6.16}$$

and

$$\frac{\partial}{\partial z}(b\omega) = 0, \tag{6.17}$$

where $\frac{\partial^2 \Phi}{\partial \xi^2}$ has been neglected in the first equation and $\frac{\partial\, b}{\partial \xi}$ in the second.

To simulate the effects of the laser pump depletion self-consistently we start with an expression for the plasma density modulation, Eq. (2.15), obtained under assumption that the perturbation is small compared to the unperturbed density, $\delta n / n_i << 1$, and taking the laser pulse to be a plane wave,

$$\frac{\delta n}{n_i}(\xi) = \frac{b^2(\xi)}{4} + k_{pi}\int_{\xi}^{\infty} \sin(k_{pi}(\xi - \xi'))\frac{b^2(\xi')}{4} d\xi', \tag{6.18}$$

where the third term on the right hand side of Eq. (2.15) is zero under the plane wave assumption. The right hand side of Eq. (6.13) can be rewritten as

$$\frac{\chi}{2} = \frac{4\pi n e^2}{2m\gamma\omega^2} = \frac{\omega_{pi}^2}{2\omega^2}\left(1 + \frac{\delta n}{n_i}\right)\left(1 - \frac{b^2}{4}\right) = \frac{\omega_{pi}^2}{2\omega^2}\left(1 + k_{pi}\int_{\xi}^{\infty} \sin(k_{pi}(\xi - \xi'))\frac{b^2(\xi')}{4} d\xi'\right) \tag{6.19}$$

to the lowest order in b^2, where the term $1/\gamma \approx 1-b^2/4$ comes from the relativistic correction to the plasma frequency.

Eq. (6.14) conserves the action (the number of photons) of the laser pulse. To prove this statement the action is rewritten in terms of b and Φ:

$$\int_{-\infty}^{+\infty} \frac{E^2}{\omega} d\xi \propto \int_{-\infty}^{+\infty} b^2 \frac{\partial \Phi}{\partial \xi} d\xi \quad . \tag{6.20}$$

Using Eq. (6.14) we obtain:

$$\frac{d}{dz}\int_{-\infty}^{+\infty} b^2 \frac{\partial \Phi}{\partial \xi} d\xi = \int_{-\infty}^{+\infty} d\xi \left[-2b \frac{\partial \Phi}{\partial z}\frac{\partial b}{\partial \xi} - b^2 \frac{\partial^2 \Phi}{\partial \xi \partial z} \right]. \tag{6.21}$$

After integrating Eq. (6.21) by parts, we obtain

$$\frac{d}{dz}\int_{-\infty}^{+\infty} b^2 \frac{\partial \Phi}{\partial \xi} d\xi = \int_{-\infty}^{+\infty} d\xi \left(-b^2 \frac{\partial^2 \Phi}{\partial \xi \partial z} \right) - b^2 \frac{\partial \Phi}{\partial z}\Bigg|_{-\infty}^{+\infty} + \int_{-\infty}^{+\infty} d\xi b^2 \frac{\partial^2 \Phi}{\partial \xi \partial z} = 0, \tag{6.22}$$

because the laser amplitude is zero at infinity.

Energy conservation in the system, described by Eqs. (6.13) and (6.14), is verified by considering first the amount of energy per unit area in the laser pulse:

$$\varepsilon_l = \frac{1}{8\pi}\int_{-\infty}^{+\infty} \frac{1}{2}\left(|E|^2 + |B|^2 \right) d\xi = \frac{1}{8\pi}\frac{m^2 c^4}{e^2}\int_{-\infty}^{+\infty} b^2 \left(\frac{\partial \Phi}{\partial \xi} \right)^2 d\xi. \tag{6.23}$$

The energy loss by the laser per unit propagation distance is given by

$$\frac{\partial \varepsilon_l}{\partial z} = \frac{m^2 c^4}{8\pi e^2}\int_{-\infty}^{+\infty} 2b \frac{\partial \Phi}{\partial \xi}\left[-b \frac{\partial^2 \Phi}{\partial \xi \partial z} - \frac{\partial b}{\partial \xi}\frac{\partial \Phi}{\partial z} + b \frac{\partial^2 \Phi}{\partial \xi \partial z} \right] d\xi = \frac{-m^2 c^4}{16\pi e^2}\int_{-\infty}^{+\infty} d\xi b^2 k^2 \frac{\partial \chi}{\partial \xi}, \tag{6.24}$$

where both Eqs. (6.13) and (6.14) have been employed. Substituting for χ from Eq. (6.19) the Eq. (6.24) becomes

$$\frac{\partial \varepsilon_l}{\partial z} = \frac{-m^2c^4k_{pi}^4}{128\pi e^2} \int_{-\infty}^{+\infty}\int_{-\infty}^{+\infty} d\xi' d\xi b(\xi)^2 b^2(\xi')\cos(k_{pi}(\xi-\xi')). \tag{6.25}$$

The amount of energy in the wake per unit length is calculated by adding the electric field energy and the kinetic energy of the electron fluid:

$$\frac{\partial \varepsilon_w}{\partial \xi} = \frac{k_{pi}}{2\pi}\int_{-\pi/k_p}^{+\pi/k_p} d\xi\left(\frac{1}{8\pi}E_w^2 + \frac{mn_iV^2}{2}\right) = \frac{k_{pi}}{8\pi^2}\int_{-\pi/k_{pi}}^{+\pi/k_{pi}} d\xi\left[k_{pi}^2\frac{mc^2}{e}\int_{-\infty}^{\infty}\cos(k_{pi}(\xi-\xi'))\frac{b^2(\xi')}{4}d\xi'\right]^2$$

$$= \frac{m^2c^4k_{pi}^4}{128\pi e^2}\int_{-\infty}^{+\infty}\int_{-\infty}^{+\infty} d\xi' d\xi'' b^2(\xi')b^2(\xi'')\cos(k_{pi}(\xi''-\xi')). \tag{6.26}$$

As can be seen from Eqs. (6.25) and (6.26) all the energy lost by the laser pulse is stored in the wake.

The evolution of the amplitude b and frequency $\frac{\partial \Phi}{\partial \xi}$ of a laser pulse as it propagates in a plasma has been obtained by integrating Eqs. (6.13) and (6.14) numerically. Figure 6-1 shows the longitudinal profile of the driving laser pulse vector potential and the relative change in the refractive index of the plasma, corresponding to the plasma wake. Similarly to the simple model of Sec. 6.1.1, it is because different parts of the laser pulse experience different values of the index of refraction, the laser pulse develops a temporal phase chirp. In Figure 6-2, b and Φ are shown as functions of ξ after the laser pulse propagated a distance $z=L_{deph}$.

The frequency spectrum of the laser pulse is redshifted and widened (Figure 6-3a) resulting in a change in the laser pulse-shape (Figure 6-3b). Such large frequency shifts should be easily observed experimentally.

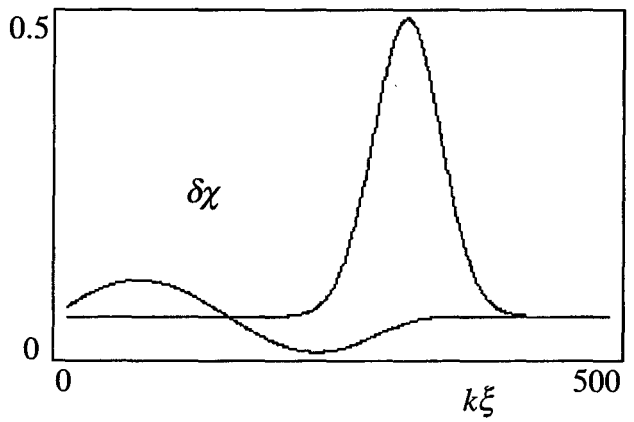

Figure 6-1

The amplitude of the laser pulse vector potential, b, gaussian pulse shape with the pulselength calculated to maximize the coupling to the plasma wake, and the plasma oscillation, $\delta\chi = \chi - 1$, from Eq.(6.19). Plotted as function of distance from the head of the laser pulse, $k\xi$.

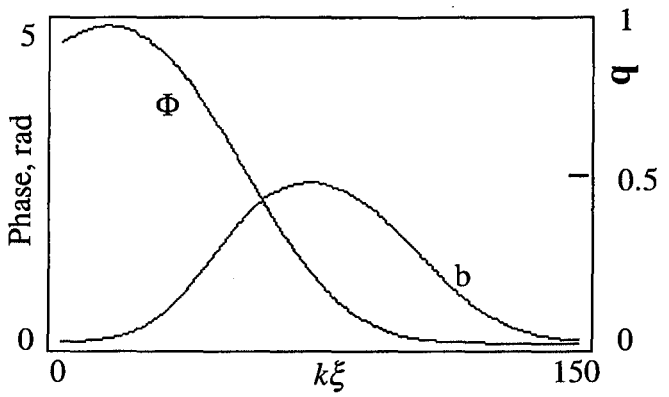

Figure 6-2

The amplitude of the laser pulse vector potential, b, and the phase, Φ, as a function of $k\xi$ after propagating for one dephasing length. Calculated by integrating Eqs. (6.13) and (6.14) numerically with χ calculated from Eq. (6.19), with $\omega_p / \omega_0 = 1/50$, a laser pulse with a gaussian pulse shape with the pulselength calculated to maximize the coupling to the plasma wake, and amplitude $a_0 = 0.5$.

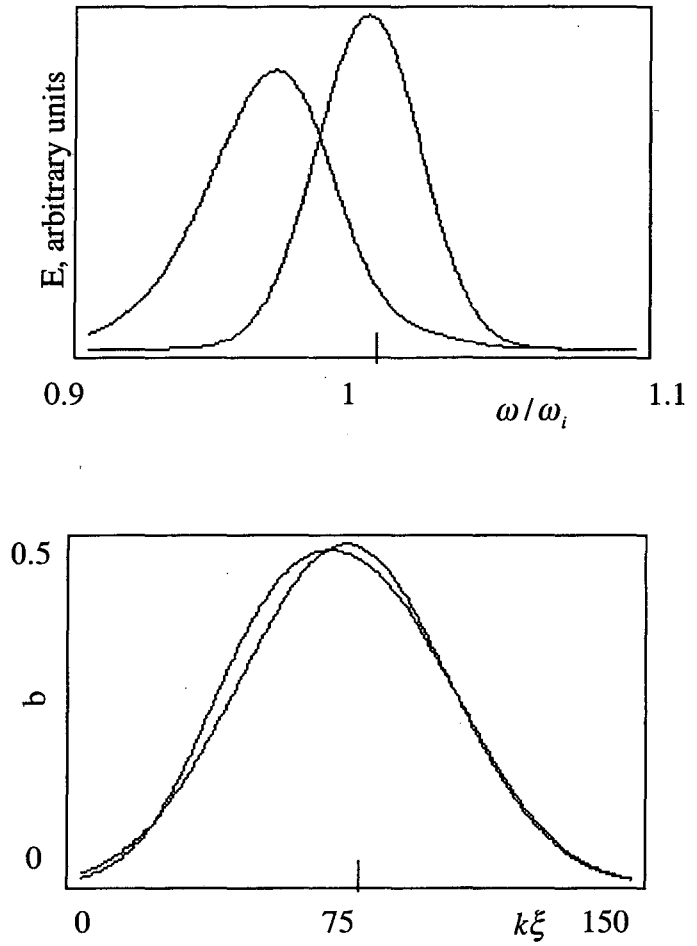

Figure 6-3

a). Spectrum of the laser pulse (unnormalized, arbitrary units) before and after propagating for one dephasing length. b). The amplitude of the laser pulse vector potential, b, before and after propagating for one dephasing length. Calculated by integrating Eqs. (6.13) and (6.14) numerically with χ calculated from Eq. (6.19), with $\omega_p/\omega_0 = 1/50$, a laser pulse with a gaussian pulse shape with the pulselength calculated to maximize the coupling to the plasma wake, and amplitude $a_0 = 0.5$.

The amplitude of the plasma wake remained nearly constant during the interaction, Figure 6-4, which is consistent with the predictions of Sec. 6.1.1.

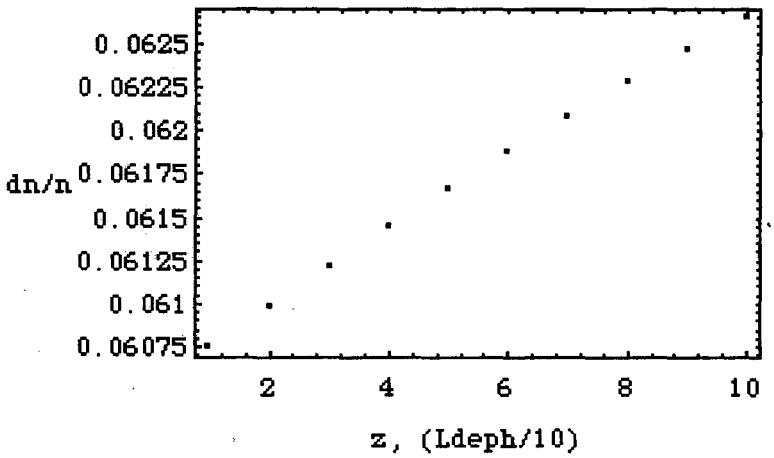

Figure 6-4

The plasma wave amplitude vs. propagation distance. The amplitude is not reduced by the laser pulse depletion.

In conclusion, the plasma wake leaves an imprint on the pulse that excites it. Through time resolved measurement of the amplitude and phase of the laser pulse, information about the wake may therefore be obtained. The observed increase in the coupling strength supports the idea of trying to increase efficiency of a single stage accelerator by depleting the laser pulse energy, before dephasing terminates the acceleration.

6.2 Driving Laser Pulse Evolution in a Hollow Channel

In a hollow channel, in addition to the electromagnetic mode, an electrostatic mode is excited in the bulk of the plasma. The amplitude of the electric field of this electrostatic mode is zero at the channel boundary, peaks at a distance of order $1/k_p$ into the plasma, and decays away at large distances. In this section the feedback of both the

electromagnetic surface wake and the electrostatic bulk wake on the laser pulse is considered.

The coupling of the bulk mode to the laser pulse is of the same nature as that of the wake in a homogeneous plasma (see Sec. 6.1.2). The laser propagation is modified by the changes in plasma density caused by the excitation of the bulk mode.

The plasma electron fluid in the electromagnetic wake mode behaves as if it is incompressible. The propagation of the laser pulse is affected by the ripple of the channel boundary due to the electromagnetic wake. The transverse displacement of the electron fluid effectively causes different longitudinal slices of the drive laser pulse to propagate in channels of different size, with varying phase and group velocity.

A set of equations governing the driving laser pulse evolution in a hollow channel in a slab geometry, with the laser pulse infinite in the x-direction guided by a hollow channel of size $2d$ in y-direction, is derived next. The wave equation (6.20), can be reduced to an equation similar to Eq. (6.24). By keeping the transverse derivative in y, and assuming that the vector potential is of the form $a_x = a_0(\xi,z)R(y,d(\xi))$, Eq. (6.23) can be rewritten as

$$0 = \frac{\partial^2 a_0}{\partial z^2} + 2\frac{\partial^2 a_0}{\partial z \partial \xi} + \frac{a_0}{R}\frac{\partial^2 R}{\partial y^2} + \frac{2}{R}\frac{\partial R}{\partial \xi}\frac{\partial a_0}{\partial z} \approx \frac{\partial^2 a_0}{\partial z^2} + 2\frac{\partial^2 a_0}{\partial z \partial \xi} - \chi k^2 a_0, \tag{6.27}$$

where the cross term $\frac{2}{R}\frac{\partial R}{\partial k\xi}\frac{\partial a_0}{\partial kz}$ has been neglected as well as the z derivatives of the transverse function R because they are of the order $(\omega_p/\omega)^4$.

Eq. (6.27) is identical to Eq. (6.14) except for the plasma coupling term $\chi(\xi)$,

which we next evaluate using energy conservation. The energy stored per unit length of the electromagnetic plasma wake is given by:

$$\frac{\partial \varepsilon_w}{\partial \xi} = \int_{-\infty}^{+\infty} dy \frac{k_{pi}}{2\pi} \int_{-\pi/k_p}^{+\pi/k_p} d\xi \left(\frac{1}{8\pi}(E_w^2 + B_w^2) + \frac{m n_i(y) V^2}{2}\right), \tag{6.28}$$

By introducing a geometric factor with dimension of unit length, c_w, which relates the wake energy per unit length to the wake's energy density on the channel's axis, we can rewrite Eq. (6.28) in a fashion similar to Eq. (6.26):

$$\frac{\partial \varepsilon_w}{\partial \xi} = c_w \frac{m^2 c^4 k_{ch}^4}{128\pi e^2} \int_{-\infty}^{+\infty} \int_{-\infty}^{+\infty} d\xi d\xi' \, b(\xi', d)^2 b^2(\xi', d) \cos(k_{ch}(\xi' - \xi)), \tag{6.29}$$

where

$$\begin{aligned} c_w &= 2d + 2\int_{-d}^{d} dy k_{ch}^2 y^2 + 2\int_{d}^{\infty} dy \left(1 + \frac{k_p^2}{k_{ch}^2}\right) e^{-2k_p(y-d)} + 2\int_{d}^{\infty} dy \left(2 + \frac{k_p^2}{k_{ch}^2}\right) \frac{k_{ch}^2}{k_p^2} e^{-2k_p(y-d)} \\ &= \left(5 + 6k_p d + 3(k_p d)^2 + \frac{4}{3}(k_p d)^3\right) \Big/ k_p (1 + k_p d). \end{aligned} \tag{6.30}$$

Similarly, the energy stored per unit length of the electrostatic bulk wake becomes

$$\frac{\partial \varepsilon_b}{\partial \xi} = c_b \frac{m^2 c^4 k_p^4}{128\pi e^2} \int_{-\infty}^{+\infty} \int_{-\infty}^{+\infty} d\xi d\xi' \, b^2(\xi', d) b^2(\xi', d) \cos(k_p(\xi' - \xi)), \tag{6.31}$$

where

$$\begin{aligned} c_b &= 2\int_{d}^{+\infty} (1 + k_p^2/k_p^2) \left[(b(y)^2 - b(d)^2 e^{-k_p(y-d)})^2 + (-2(p/k_p) b(y)^2 + b(d)^2 e^{-k_p(y-d)})^2\right] / b(d)^4 dy = \\ &= (k_p^3 - 2k_p^2 p - 4k_p p^2 + 8p^3) / \left[k_p^2 p(k_p + 2p)\right]. \end{aligned} \tag{2.61}$$

Equivalently to Eq. (6.24), the energy change in the laser pulse per unit propagation distance is given by:

$$\frac{\partial \varepsilon_l}{\partial z} = -c_l \frac{m^2 c^4}{16\pi e^2} \int_{-\infty}^{+\infty} d\xi b^2 k^2 \frac{\partial \chi}{\partial \xi}, \tag{2.33}$$

where c_l is a geometric factor for the laser mode, similar to c_w:

$$c_l = \int_{-d}^{d} dy \cos^2(k_y y) + 2\int_{d}^{\infty} dy \cos^2(k_y d) e^{-2p(y-d)} = d + 1/p. \tag{6.34}$$

For energy to be conserved, it is therefore required that χ be of the form:

$$\chi = \frac{c_b k_p^3}{4c_l k^2} \int_{\xi}^{+\infty} d\xi' \, b(\xi', d)^2 \sin(k_p(\xi - \xi')) + \frac{c_w k_{ch}^3}{4c_l k^2} \int_{\xi}^{+\infty} d\xi' \, b(\xi', d)^2 \sin(k_{ch}(\xi - \xi')) + \frac{k_y^2}{k^2}. \tag{6.35}$$

Laser evolution in a hollow channel can now be treated similarly to the 1-D case of Sec. 2.52 with exception of the coupling term, $\chi(\xi)$, which is calculated using energy conservation and contains contributions from two wake modes with different frequencies. In addition the treatment can be extended to an arbitrary transverse profile plasma channel, provided the wake is known.

The evolution of the amplitude b and frequency $\frac{\partial \Phi}{\partial \xi}$ of a laser pulse as it propagates in a hollow channel plasma has been obtained by integrating Eqs. (6.13) and (6.14) numerically with $\chi(\xi)$ calculated from Eq. (6.19). In Figure 6-4, b and Φ are shown as functions of ξ after the laser pulse propagated a distance $z=L_{deph}$ in a hollow channel of width $k_p d = 1$. The geometric energy density coefficients for this case are calculated to be: $k_p c_l = 2.48$, $k_p c_w = 7.67$, and $k_p c_b = 0.179$. Since the geometric factor for the bulk mode is much smaller that that for the surface mode, the periodicity of the phase change in Figure 6-5 is $1/k_{ch}$ and otherwise the results are similar to those for the case of homogeneous plasma and plane wave laser pulse (Figure 6-2 and Figure 6-3): the

frequency spectrum of the laser pulse is redshifted and widened (Figure 6-6a) resulting in a change in the laser pulse-shape (Figure 6-6b) and the amplitude of the plasma wake remained nearly constant during the interaction, which is consistent with the predictions of Sec. 6.1.1.

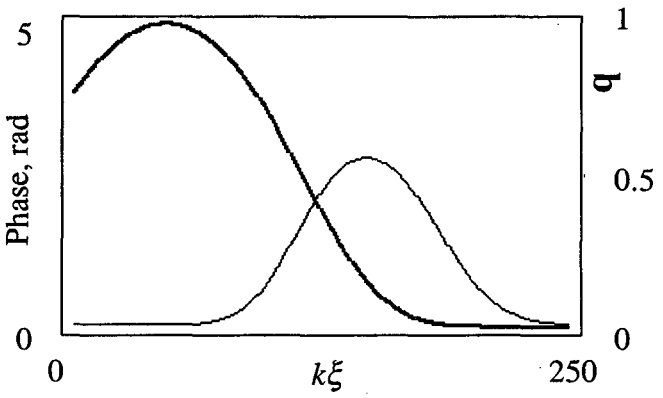

Figure 6-5

The amplitude of the laser pulse vector potential, b, and the phase, Φ, as a function of $k\xi$ after propagating for one dephasing length in a hollow channel, $k_p d = 1$. Calculated by integrating Eqs. (6.13) and (6.14) numerically with χ calculated from Eq. (6.19), with $\omega_p / \omega_0 = 1/50$, a laser pulse with a Gaussian pulse shape, and amplitude $a_0 = 0.5$.

This method could be extended to treating arbitrary channel shapes, provided the wakefield modes of those channels were known. Fluid simulations developed by B. A. Shadwick and J. S. Wurtele [16] allow characterization of the mode structure of channels with arbitrary plasma density profiles. Coupled with those, this theory will be able to provide a full selfconsistent picture of laser evolution as it excites the plasma wake, and the effect the depletion will have on the excited wake.

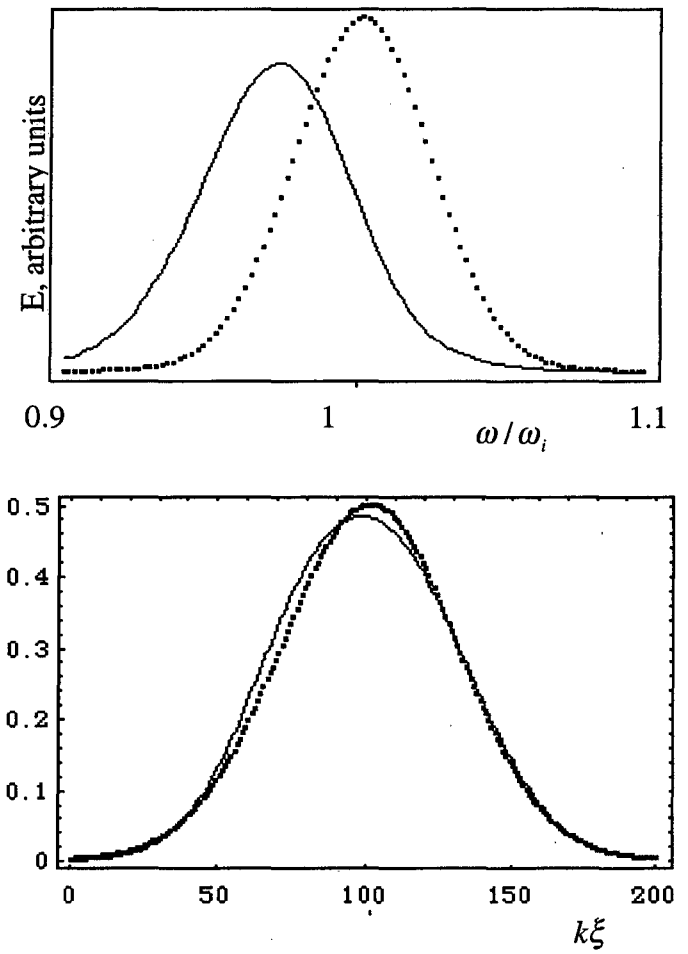

Figure 6-6

a). Spectrum of the laser pulse (unnormalized, arbitrary units) before and after propagating for one dephasing length in a hollow channel, $k_p d = 1$. b). The amplitude of the laser pulse vector potential, b, before and after propagating for one dephasing length in a hollow channel, $k_p d = 1$. Calculated by integrating Eqs. (6.13) and (6.14) numerically with χ calculated from Eq. (6.19), with $\omega_p / \omega_0 = 1/50$, a laser pulse with a Gaussian pulse shape , and amplitude $a_0 = 0.5$.

7 Conclusions

This thesis addressed the limitations on the length of a Laser Wakefield accelerating stage. To overcome the laser diffraction length limit, a novel method of plasma channel production for laser guiding, the Ignitor - Heater technique, was proposed and tested experimentally. Laser pulse depletion and dephasing were studied theoretically by solving the problem of intense laser pulse evolution in plasmas. A laser wake diagnostic, based on the results of this theory, was proposed.

The Ignitor - Heater plasma channel formation method makes use of two laser pulses. A femtosecond Ignitor pulse, brought to a line focus with a cylindrical optic, is used to initially ionize the gas. A longer, ~160 ps, heater pulse is then introduced to heat and further ionize the plasma through collisions. The heated cylinder of gas expands, creating radial plasma density distribution with a minimum on axis. Such a plasma channel is an optical waveguide.

This scheme made it possible, for the first time, to create preformed guiding plasma channels in hydrogen and deeply ionized nitrogen without high atomic number additives, thereby allowing high intensity laser pulse guiding. To avoid the ionization induced refraction of the guided laser pulse, the plasma channels were formed in a plume of a pulsed gas jet. It should be also noted that the Ignitor – Heater scheme employs cylindrical optics that could be kept out of the path of the accelerator beam and,

potentially, allow the recycling of the laser beams. The channel formation process was fully characterized with time resolved 2-D longitudinal interferometry diagnostic using a femtosecond probe pulse. From the measured dynamics of the radial shock expansion, the temperature and energy of the heated plasma were calculated. The ability to independently control the intensity of the Ignitor pulse allowed us to control the transverse extent of the initial ionization spark. The length of the initial spark effected the shape of the plasma channel. In this fashion channel transverse aspect ratio was controlled from ~ 1 to ~10.

Laser pulses at record high intensity ($\sim 5\times10^{17}$ W/cm^2) were guided in these channels over ~ 10 Rayleigh lengths. Control over the channel shape allowed us to observe guiding in one transverse dimension, for channels with high aspect ratio, or guiding in both X and Y, if a round channel was formed. Experimental and theoretical investigations were conducted to obtain further insight into the coupling of a laser pulse to the plasma channel guided mode and the tunneling of the trapped laser through the channel wall.

The self-consistent theoretical treatment of laser pulse propagation in underdense plasma was presented in Chapter 5. The laser pulse was shown to lose its energy to the plasma wave by reduction in the frequency, not loss or conversion of photons. A prediction of an approximate linear theory, that the excited wave amplitude is not strongly affected by the driving laser pulse depletion, was verified by numerically integrating the self-consistent equations. This is an important result for LWFA design,

suggesting that a large portion of the driving laser pulse can be depleted in a dephasing length without reduction in accelerating gradient.

The 1-D theory was extended to treat the case of a laser exciting a wake in a hollow plasma channel, by making use of an energy conservation argument. This method is applicable to a plasma channel of arbitrary radial plasma density profile, provided that the wakefield modes are known for such a channel.

Because the laser pulse evolution is governed by the plasma wave that is created within the laser pulse duration, the excited wave time resolved amplitude can be inferred from the time dependence of the laser phase. Thus, the theory of this thesis, combined with a temporally resolved measurement of the laser phase, can serve as a diagnostic of the excited plasma wave profile (within the laser pulse). The formalism of Chapter 5 can be applied to calculating the evolution of any laser pulse, propagating with the wake. The theory of this thesis can be used to add value to already existing Longitudinal Interferometry diagnostic [11] by calculating the evolution of the interferometric probe pulse with taking into account the effects of group and phase velocities slippage.

Beyond its impact on the development of laser-plasma accelerators, this thesis lays the groundwork for many new physics experiments. The 2-D interferometer diagnostic with femtosecond temporal resolution demonstrated measurement of the plasma density and temperature. The gas jet characterization technique, developed as a part of this thesis, will be of immediate interest for plasma lens experiments planned at the Stanford Linear Collider. The temperature measurement allows calculation of the inverse Brehmsstrahlung crossection, relevant for understanding the absorption of high

8 Bibliography

[1] J.L. Feng, M.E. Peskin, H. Murayama, X. Tata, "Testing supersymmetry at the Next Linear Collider." Physical Review D (Particles and Fields), vol.52, (no.3), 1 ,Aug. 1995. p.1418-32.

[2] T. Tajima and J.M. Dawson, Phys. Rev. Lett. **43**, pp. 267-270 (1979).

[3] L. M. Gorbunov and V.I. Kirsanov, Sov. Phys. JETP, vol. 66, p. 290, 1987; P. Sprangle, E. Esarey, A. Ting and G. Joyce, "Laser wakefield acceleration and relativistic optical guiding", Appl. Phys. Lett., vol. 53, pp. 2146-2148, 1988; E. Esarey, A. Ting, P. Sprangle, and G. Joyce, "The laser wakefield accelerator", Comments Plasma Phys. Controlled Fusion, vol. 12, pp. 191-204, 1989.

[4] C. E. Clayton, K. A. Marsh, A. Dyson, M. Everett, A. Lal, W. P. Leemans, R. Williams, and C. Joshi, " Ultrahigh-Gradient Acceleration of Injected Electrons by Laser-Excited Relativistic Electron Plasma Waves", Phys. Rev. Lett., vol. 70, pp. 37 - 40, 1993; F. Amiranoff et al.,"Electron acceleration in Nd-laser plasma beat-wave experiments", Phys. Rev. Lett., vol. 74, pp. 5220-5223, 1995.

[5] C. E. Clayton, K. A. Marsh, A. Dyson, M. Everett, A. Lal, W. P. Leemans, R. Williams, and C. Joshi, " Ultrahigh-Gradient Acceleration of Injected Electrons by Laser-Excited Relativistic Electron Plasma Waves", Phys. Rev. Lett., vol. 70, pp. 37 - 40, 1993; F. Amiranoff et al.,"Electron acceleration in Nd-laser plasma beat-wave experiments", Phys. Rev. Lett., vol. 74, pp. 5220-5223, 1995.

[6] D. Strickland and G. Mourou, "Compression of amplified chirped optical pulses," Opt. Commun., vol.56, pp. 219-221, 1985.

[7] T. Tajima, "High energy laser plasma accelerators", Laser Part. Beams, vol. 3, pp. 351-413, 1985

[8] C.G. Durfee III and H. M. Milchberg, "Light pipe for high intensity laser pulses", Phys. Rev. Lett., vol. 71, pp. 2409, 1993; C.G. Durfee III, J. Lynch, and H.M. Milchberg, "Development of a plasma wave guide for high intensity laser pulses", Phys. Rev. E, vol. 51, pp. 2368, (1995).

[9]P. Volfbeyn, P.B. Lee, J. S. Wurtele, W. P. Leemans, G.Shvets, "Driving laser pulse evolution in a hollow channel laser wakefield accelerator", Phys. Plasmas **4**, pp. 3403-3410 (1997).

[10] C.E. Clayton, C. Darrow, C. Joshi, "Novel small-angle collective Thomson scattering

system." Applied Optics, vol.24, (no.17), p.2823-6, (1985);

[11] C. W. Siders, S. P. Le Blanc; D . Fisher; T.Tajima, M.C. Downer, A. Babine, A. Stepanov, A. Sergeev, "Laser Wakefield Excitation and Measurement by Femtosecong Longitudinal Interferometry", Phys. Rev. Lett. v. 76, no. 19, pp. 3570-3573 (1996); J. R. Marques, J. P. Geindre, F. Amiranoff, P. Audebert, J. C. Gauthier, A. Antonetti, G. "Temporal and spatial measurements of the electron density perturbation produced in the wake of an ultrashort laser pulse", Phys. Rev. Lett. may 6,,V76(N19):3566-3569 (1996)

[12] E. Esarey et al., IEEE Trans. Plasma Sci., vol. PS-24, pp. 252-288 (1996); E. Esarey et al., IEEE J. Quant. Electron. 33, pp. 1879-1914 (1997).

[13] G. Shvets, "Interaction of intense lasers with plasmas", Ph.D. dissertation, MIT, 1995.

[14] G. Shvets and J. S. Wurtele, "Instabilities of short pulse laser propagation through plasmas", Phys. Rev. Lett., vol. 73, p. 3540, 1994

[15]T.C. Chiou, T. Katsouleas, C. Decker, W. B. Mori, G. Shvets, J. S. Wurtele, "Laser wakefield acceleration and optical guiding in a hollow plasma channel", Phys. Plasmas, vol. 2, pp. 310-318, 1995.

[16] B. A. Shadwick, G. Shvets, J. S. Wurtele, Bull. Am. Phys. Soc., v. 41, p.1601, B. A. Shadwick and J. S. Wurtele, to be published.

[17]E. Esarey et al., IEEE Trans. Plasma Sci., vol. PS-24, pp. 252-288 (1996); E. Esarey et al., IEEE J. Quant. Electron. 33, pp. 1879-1914 (1997).

[18]C. Max, J. Arons and A.B. Langdon, "Self-modulation and self-focusing of electromagnetic waves in plasmas," Phys. Rev. Lett., vol. 33, pp. 209-212, 1974.

[19] P. Sprangle, C.M. Tang, and E. Esarey, ``Relativistic self-focusing of short-pulse radiation beams in plasmas," IEEE Trans. Plasma Sci., vol. PS-15, pp. 145-153, 1987.

[20] G.Z. Sun, E. Ott, Y.C. Lee, and P. Guzdar, ``Self-focusing of short intense pulses in plasmas," Phys. Fluids, vol. 30, pp. 526-532, 1987.

[21] W.B. Mori, C. Joshi, J.M. Dawson, D.W. Forslund, and J.M. Kindel, ``Evolution of self-focusing of intense electromagnetic waves in plasma," Phys. Rev. Lett., vol. 60, pp. 1298-1301, 1988.

[22] E. Esarey, A. Ting, and P. Sprangle, ``Optical guiding and beat wave phase velocity control in the plasma beat wave accelerator", in Advanced Accelerator Concepts, edited by C. Joshi, AIP Conf. Proc. vol. 193 , pp. 71-86, 1989.

[23] P. Sprangle, E. Esarey, and A. Ting, ``Nonlinear theory of intense laser-plasma interactions," Phys. Rev. Lett., vol. 64, pp. 2011-2014, 1990; ``Nonlinear interaction of intense laser pulses in plasmas," Phys. Rev. A, vol. 41, pp. 4463-4469, 1990.

[24]R.Wagner, S.-Y. Chen, A.Maksimchuk, D. Umstadter, "Electron acceleration by a laser wakefield in a relativistically self-guided channel." Physical Review Letters, vol.78, (no.16), APS, 21 April 1997. p.3125-8.

[25] T.C. Chiou, T. Katsouleas, C. Decker, W. B. Mori, G. Shvets, J. S. Wurtele, "Laser wakefield acceleration and optical guiding in a hollow plasma channel", Phys. Plasmas, vol. 2, pp. 310-318, 1995.

[26] P. Sprangle, E. Esarey, J. Krall, and G. Joyce, "Propagation and guiding of intense laser pulses in plasmas", Phys. Rev. Lett., vol. 69, pp. 2200,1992; E. Esarey, P. Sprangle, J. Krall, A. Ting and G. Joyce, "Optically guided laser wakefield acceleration", Phys. Fluids B, vol. 5, pp. 2690-2697, 1993.

[27] Donald L. Lee, *Electromagnetic Principles of Integrated Optics* (Wiley, New York, 1986), Chapter 4.

[28] Amnon Yariv, *Optical Electronics*, 3rd edition (Holt, Rinehart, and Winston, New York, 1985), Chapter 3.

[29] T. M Antonsen,, Jr.; P. Mora, "Leaky channel stabilization of intense laser pulses in tenuous plasmas." Physical Review Letters, vol.74, (no.22), 29 May 1995. p.4440-3.

[30] C. B. Schroeder, J. S. Wurtele, D. H. Whittum, "Multimode analysis of the plasma channel accelerator", submitted to Phys. Rev. Lett.

[31] W.P. Leemans et al., "Experiments and simulations of tunnel-ionized plasmas", Phys. Rev. A, 46, 1091 (1992)

[32] S. Augst et al., PRL, vol. 63, no. 20, 2212 (1989)

[33] W. P. Leemans, et al."Plasma physics aspects of tunnel ionized gases," Phys. Rev. Lett. vol. 68, pp. 321-324, 1992

[34] Francis F. Chen, "Introduction to plasma physics and controlled fusion", v. 1: Plasma Physics, p. 181, Plenum Press, New York, 1984.

[35]C. D. Decker et al., Phys. Plasmas 1 (12), 4043 (1994)

[36] G. Shvets and N. J. Fisch, Phys. Plasmas, Vol. 4, No. 2, 428 (1997)

[37]J. M. Dawson and C. Oberman, Phys. Phluids 5, 517 (1962)

[38] V. P. Silin, Sov. Phys. JETP 20, 1510 (1965)

[39] W. P. Leemans et al., IEEE Trans. Plasma Sci **24**, pp. 331-342, 1996

[40] E. Esarey, J. Krall, and P. Sprangle, ``Envelope analysis of intense laser pulse self-modulation in plasmas", Phys. Rev. Lett., vol. 72, pp. 2887-2890, 1994.

[41] Kapteyn-Murnane Laboratories L.L.C., MI, USA

[42] T. Brabec, et. al., "Kerr lens modelocking", Opt. Lett., 17, 1292 (1992)

[43] H. A. Haus, J. P. Fujimoto, and E. P. Ippen, "Analytic Theory of additive pulse and Kerr lens mode locking, IEEE J. Quant. Elec. 28, 2086 (1992)

[44] R. L. Fork et al., "Negative dispersion using pairs of prisms", Opt. Lett., 9, 150 (1984)

[45] Positive Light Inc., Los Gatos, CA, USA

[46] Soliton Ltd., Moscow, Russia

[47] D. J. Kane and R. Trebino, IEEE J. of Quant. Electron. Vol. 29, p.571 (1993)

[48] W. P. Leemans et al. "Experimenta and simulations of tunnel ionized plasmas," Phys. Rev. A, 46,1091, 1992

[49] G. P. Agrawal, *Nonlinear Fiber Optics*. Academic Press Inc., Boston, San Diego, 1989

[50] General Valve, Inc.

[51] M. Takeda et al., J. Opt. Soc. Am. B, vol. 72, 156 (1981)

[52] H. Griem, *Plasma Spectroscopy,* p. 176, New York, McGraw-Hill (1964)

[53] L. I. Sedov "Propagation of strong blast waves", Prikl. Mat. I Mekh. v. 10, 241-250 (1946).

[54] Ya. B. Zel'dovich and Yu. P. Raizer, *Elements of Gasdynamics and the Classical Theory of Shock Waves,* pp. 93-99,Academic Press, New York, (1968)

[55] J. Sheffield, *Plasma scattering of electromagnetic radiation*, Academic Press, New York, 1975

[56] S. V. Bulanov, I. N. Inovenkov, V. I. Kirsanov, N. M. Naumova, and A. S. Sakharov, "Nonlinear depletion of ultrashort and relativistically strong laser pulses in an underdense plasma", Phys. Fluids B 4 (7), July 1992

[57] J. M. Rax and N. J. Fisch, "Nonlinear relativistic interaction of an ultrashort pulse with a cold plasma", Phys. Fluids B, vol. 4, pp. 1323-1331, 1992.

[58] W. Horton and T. Tajima, "Pump depletion in the plasma-beat-wave accelerator", Phys. Rev. A, vol.34, (no.5):4110-19, Nov. 1986.

Ernest Orlando Lawrence Berkeley National Laboratory
One Cyclotron Road | Berkeley, California 94720

Prepared for the U.S. Department of Energy under Contract No. DE-AC03-76SF00098